

VILNIUS UNIVERSITY
CENTER FOR PHYSICAL SCIENCES AND TECHNOLOGY

Vitalij Fiodorov

Laser-Assisted Selective Fabrication of Metal Traces on Polymers by Electroplating

DOCTORAL DISSERTATION

Technological Sciences,
Material Engineering (T 008)

VILNIUS 2025

The dissertation was written in 2019 – 2025 in the Department of Laser Technologies of the Center for Physical Sciences and Technology.

Academic supervisor:

Dr Gediminas Račiukaitis (Center for Physical Sciences and Technology, Technological Sciences, Material Engineering – T 008).

This doctoral dissertation will be defended in a public meeting of the Dissertation Defense Panel:

Chairman – Prof. Dr. Domas Paipulas (Vilnius University, Technological Sciences, Material Engineering, T 008).

Members:

Dr. Mindaugas Gedvilas (Center for Physical Sciences and Technology, Technological Sciences, Material Engineering, T 008).

Dr. Ieva Matulaitienė (Center for Physical Sciences and Technology, Natural Sciences, Chemistry, N 003).

Prof. Dr. Tomas Tamulevičius (Kaunas University of Technology, Technological Sciences, Material Engineering, T 008).

Dr. Bogdan Voisiat (Technical University of Dresden, Germany, Technological Sciences, Material Engineering, T 008).

The dissertation shall be defended at a public meeting of the dissertation defense panel at 10 AM on 16th of April 2025 in the Institute of Physics meeting room. Address: Savanorių av. 231, Vilnius, Lithuania.

Tel. +37062862878; e-mail: vitalijfiodorov@yahoo.com.

The text of this dissertation can be accessed at the library of Vilnius University, as well as on the website of Vilnius University:

www.vu.lt/lt/naujienos/ivykiu-kalendorius

VILNIAUS UNIVERSITETAS
FIZINIŲ IR TECHNOLOGIJOS MOKSLŲ CENTRAS

Vitalij Fiodorov

Lazeriu asistuotas selektyvus polimerų dengimas metalu galvaniniu būdu

DAKTARO DISERTACIJA

Technologijos mokslai,
Medžiagų inžinerija (T 008)

VILNIUS 2025

Disertacija rengta 2019– 2025 metais Fizinių ir technologijos mokslų centre.
Mokslinius tyrimus rėmė Lietuvos mokslo taryba.

Mokslinis vadovas:

dr. Gediminas Račiukaitis (Fizinių ir technologijos mokslų centras,
technologijos mokslai, medžiagų inžinerija, T 008).

Gynimo taryba:

Pirmininkas – prof. dr. Domas Paipulas (Vilniaus universitetas, technologijos
mokslai, medžiagų inžinerija, T 008).

Nariai:

dr. Mindaugas Gedvilas (Fizinių ir technologijos mokslų centras,
technologijos mokslai, medžiagų inžinerija, T 008).

dr. Ieva Matulaitienė (Fizinių ir technologijos mokslų centras, gamtos
mokslai, chemija, N 003)

prof. dr. Tomas Tamulevičius (Kauno technologijos universitetas,
technologijos mokslai, medžiagų inžinerija, T 008)

dr. Bogdan Voisiat (Dresdено technikos universitetas, Vokietija, technologijos
mokslai, medžiagų inžinerija, T 008).

Disertacija ginama viešame gynimo tarybos posėdyje 2025 m. 04 mėn. 16 d.
10 val. Fizikos instituto posėdžių saleje. Adresas: Savanorių pr. 231, Vilnius,
Lietuva. Tel. +37062862878; el. paštas vitalijfiodorov@yahoo.com.

Disertaciją galima peržiūrėti Vilniaus universiteto bibliotekoje ir VU interneto
svetainėje adresu: <https://www.vu.lt/naujienos/ivykiu-kalendorius>

CONTENTS

LIST OF ABBREVIATIONS	8
INTRODUCTION	10
THE AIM OF THE THESIS	12
SCIENTIFIC NOVELTY	12
STATEMENTS TO BE DEFENDED	12
APPROBATION.....	13
AUTHOR CONTRIBUTION	14
CO-AUTHOR CONTRIBUTION	14
1. LITERATURE OVERVIEW	15
1.1. Polymers	15
1.2. Conductive polymers.....	17
1.3. Polymers with conductive impurities	18
1.4. High-performance polymers	19
1.5. Polyimides	20
1.6. Biodegradable polymers	22
1.7. Carbon and its forms.....	23
1.7.1. Carbon allotropes.....	23
1.7.2. History of graphene, its structure, and properties	24
1.7.3. Graphene applications.....	26
1.7.4. Graphene characterization methods	27
1.8. Graphene formation methods	29
1.8.1. Mechanical methods	29
1.8.2. Graphene formation by chemical vapor deposition	29
1.8.3. Epitaxial growth.....	29
1.8.4. Chemical reduction of graphene oxide	30
1.8.5. Laser-induced graphene	30
1.9. Interaction of laser radiation with polymers	31
1.9.1. Polymer absorption of laser radiation	31
1.9.2. Nonlinear absorption.....	32
1.9.3. Tunnelling process	33
1.10. Laser-assisted electric circuit formation methods.....	34
1.10.1. Laser direct structuring	34
1.10.2. Selective surface activation induced by laser.....	35
1.10.3. Microscopic integrated processing technology	36

1.10.4.	Laser-induced forward transfer	36
1.10.5.	Laser-induced surface activation	37
1.10.6.	Laser-assisted metal deposition from the liquid phase.....	38
1.11.	Other electric circuit formation methods	39
1.11.1.	Photolithography.....	39
1.11.2.	Aerosol jet printing	40
1.11.3.	Inkjet printing	41
1.11.4.	Pressing.....	42
1.11.5.	Brushing a metal paint	42
1.11.6.	Physical vapor deposition on polymers	43
1.11.7.	Chemical vapor deposition on polymers.....	43
1.12.	Comparison between electroless plating and electroplating	43
1.12.1.	Electroless plating.....	43
1.12.2.	Electroplating.....	45
1.13.	Electroplating on polymers.....	47
1.13.1.	Electroplating on conductive polymers.....	47
1.13.2.	Electroplating process on ABS plastic.....	48
1.13.3.	Selective electroplating of 3D printed parts.....	49
2.	EXPERIMENTAL SETUP AND METHODS	50
2.1.	Materials	50
2.2.	Laser treatment	51
2.3.	Electroplating	53
2.4.	Sheet resistance measurement	54
2.5.	Adhesion measurements	55
2.6.	Surface morphology analysis.....	55
2.7.	Raman spectroscopy	56
3.	RESULTS AND DISCUSSION.....	57
3.1.	Laser treatment of samples	57
3.1.1.	Polyimide treatment with picosecond and nanosecond lasers at the focal plane	57
3.1.2.	Irradiation at the non-focal plane with 1064 nm.....	59
3.1.3.	Fabricating with 355 nm and 532 nm out of the focal plane.....	65
3.1.4.	LIG formation in a nitrogen atmosphere.....	67
3.1.5.	PI treatment with 10.6 μ m wavelength.....	68
3.1.6.	Biopolymer processing with 1064 nm	70

3.1.7.	Modelling of the heat conduction after laser pulses exposition to a substrate	71
3.1.8.	Summary.....	77
3.2.	Raman spectra analysis of treated surfaces.....	78
3.2.1.	Raman spectra investigation of samples treated with 1064 nm laser wavelength	78
3.2.2.	Raman spectra of samples treated with 355 nm and 532 nm laser wavelengths.....	82
3.2.3.	Raman spectra of samples treated with 1064 nm laser wavelength in a nitrogen atmosphere	82
3.2.4.	Raman spectra of samples treated with 10.6 μm laser wavelength.	83
3.2.5.	Summary.....	86
3.3.	Electroplating of LIG surfaces.....	86
3.3.1.	Copper plating on LIG formed with 1064 nm wavelength	86
3.3.2.	Copper plating on LIG formed with 532 nm wavelength	89
3.3.3.	LIG deposition with other metals	90
3.3.4.	Summary.....	91
LIST OF CONCLUSIONS		92
SANTRAUKA		94
BIBLIOGRAPHY		101
Curriculum Vitae		114
PADÈKA		115

LIST OF ABBREVIATIONS

List of acronyms

ABS	Acrylonitrile butadiene styrene
CB	Carbon black
CCD	Charged-coupled device
CNT	Carbon nanotube
CVD	Chemical Vapor Deposition
EDTA	Ethylenediamine tetra acetic acid
FWHM	Full width at the half maximum
GO	Graphene oxide
HDPE	High-density polyethylene
ICP	Intrinsically conducting polymers
IR	Infrared
LCP	Liquid crystal polymers
LDPE	Low-density polyethylene
LDS	Laser direct structuring
LIFT	Laser-induced forward transfer
LIG	Laser-induced graphene
LISA	Laser-induced selective activation
MID	Molded interconnect device
MIPTEC	Microscopic integrated processing technology
NA	Numerical aperture
PA	Polyacetylene
PBAT	Polybutylene adipate terephthalate
PCB	Printed circuit board
PCL	Polycaprolactone
PE	Polyethylene
PEEK	Polyether ether ketone
PEI	Polyetherimide
PEO	Polyethylene oxide

PET	Polyethylene terephthalate
PHA	Polyhydroxyalkanoates
PI	Polyimide
PLA	Polylactic acid
PMMA	Polymethyl methacrylate
PP	Polypropylene
Ppy	Polypyrrole
PPS	Polyphenylene sulfide
PS	Polystyrene
PSU	Polysulphone
PT	Polythiophene
PTFE	Polytetrafluoroethylene
PVC	Polyvinyl chloride
PVD	Physical vapor deposition
Red	Reducing agent
rGO	Reduced graphene oxide
SACADA	Samara Carbon Allotrope Database
SEM	Scanning electron microscope
SSAIL	Selective surface activation induced by laser
TEM	Transmission electron microscope
TPE	Thermoplastic elastomer
UV	Ultraviolet
VIS	Visible
XRD	X-ray diffraction

INTRODUCTION

Recent developments in semiconductor technologies have led to the miniaturization of various electronic devices. Alongside this growing trend, the vast rise of flexible electronics takes place. New methods for fabricating conductive tracks on flexible materials are constantly being developed to implement flexible and 3D electronics.

The technologies of selective fabrication of copper tracks on dielectrics show massive potential for current and future electronics applications. There are several laser-assisted techniques for producing copper tracks on dielectric materials. One of the most common processes is laser direct structuring (LDS). LDS is a two-step method where an electric pattern is initially written by a laser on the surface of dielectric material. Further, the material is immersed in the electroless copper bath, where copper is deposited on the laser-activated treated areas [1]. Another method is laser-induced forward transfer (LIFT). The principle of this technique is that thin donor material is placed above the specimen, and the laser exposition transfers the material from the thin donor to the sample [2]. A novel three-step method is selective surface activation induced by laser (SSAIL) [3]. Initially, a pattern is written by a focused laser beam on the specimen surface. A further step is the chemical activation of laser-modified areas. Finally, metal is deposited on the laser-treated area by electroless plating.

Most laser-assisted copper track production methods use electroless plating for metal deposition. Electroless plating has its own disadvantages, as it is a slow process. Also, the instability of the plating bath strongly affects deposition quality. Moreover, those laser-assisted techniques for copper track fabrication are suitable for 2D surfaces, however, not all of them are appropriate for 3D surfaces. Currently, only the LDS method has gained success in manufacturing electronic devices.

This research presents an alternative laser-assisted copper tracks formation method, including laser-induced graphene (LIG) formation on the commercial polymer. Our laser-assisted technology consists of two main steps: firstly, the electric circuit is laser-written on a dielectric surface by forming a conductive graphene layer. Then, the sample is immersed in the electrolytic solution, where laser-treated areas are copper-deposited by electroplating. The method is novel; we could not find any publications about electroplating on the graphene surface.

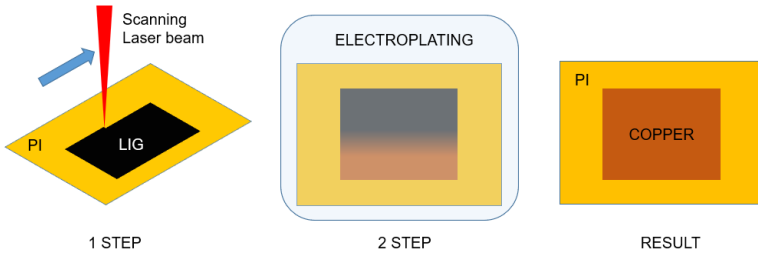


Figure 1. Schematic of two-step copper deposition process on polyimide (PI) [4].

The electroplating process is possible only on electro-conductive surfaces [5]. However, using electro-conductive polymers and conductive composites prevents spatial selectivity of the plating. Electroplating polymers is feasible in some cases by adding an initial electroless plating layer of nickel or copper to provide a conductive surface on the plastic part [6]. Another alternative is that the conductivity of some polymers could be increased after laser irradiation due to graphene formation on laser-irradiated areas. The conductivity of formed laser-induced graphene (LIG) is too low to be used directly in most electronics applications. However, it is high enough for the electroplating process. Graphene has gathered extensive attention from research communities and the electronics industry over the past decade. That is because this 2D material possesses a set of peculiar physical properties [7], making it a strong candidate for broad applications in electronics [8-11]. Moreover, from the various graphene production methods being developed, laser-based ones can offer production flexibility and scaling options. Laser-induced graphene has already been proven as an adequate material for sensors and energy storage [12-17]. It is known that LIG can be formed in various organic materials [18-20] and polymers. For example, various groups reported the successful formation of LIG in polyimide using far-infrared CO_2 [13, 16, 21-25] and ultrashort pulsed lasers working from IR to UV wavelengths [26-28].

In our research, surface conductivity measurements and Raman spectroscopy were applied to characterize the laser-modified polymer surface. Then, electroplating parameters were varied to get a uniform copper layer on laser-treated areas. The main advantage of the method is that direct electroplating on polymers allows the deposition of metal much faster than using electroless plating, like in LDS or SSAIL technologies. Also, the method offers selectiveness, low cost, and the ability to produce copper tracks on 3D complex-shaped materials, whereas conventional methods, such as photolithography, are unsuitable.

THE AIM OF THE THESIS

The main task of the research was to investigate a new laser-assisted method for producing copper tracks on polymers. Three tasks were set to achieve the main goal:

- Investigation of laser treatment processes for high conductivity graphene layer formation on polymer surface.
- Analysis of the quality of graphene formed after laser treatments with various wavelengths.
- Investigation of the electroplating process for metal deposition on the laser-formed conductive graphene layer.

SCIENTIFIC NOVELTY

This thesis explores a novel laser-assisted method for selective fabrication of copper tracks, based on the formation of graphene on polymer substrates. The method could be used to produce copper tracks on 3D materials or flexible electronic devices, where most conventional methods are not suitable. The quality of laser-induced graphene on a polyimide surface using a wide range of laser parameters, different laser sources, and wavelengths was compared and analyzed. It was demonstrated that graphene properties could be controlled by modifying the laser fabrication parameters. Two novel laser treatment techniques for graphene formation were developed.

Copper deposition by electroplating was performed on a laser-formed conductive graphene layer, and a thin and uniform layer of copper was deposited. Nickel, silver, zinc, and tin metals, widely used in the electronic industry, were also electroplated on laser-induced graphene. Electroplating of these metals on laser-induced graphene has never been published before.

STATEMENTS TO BE DEFENDED

1. The formation of a high-conductivity laser-induced graphene layer on a polyimide film requires irradiating its surface temperature above 1000 K for a particular time of 1.4 milliseconds, which could be achieved by selecting a proper irradiation dose.
2. The sheet resistance of the laser-induced graphene could be used as a mark of LIG formation, as it correlates with the intensity ratios of Raman spectra peaks $I(2D)/I(G)$ and $I(D)/I(G)$, when a lower sheet resistance corresponds to higher $I(2D)/I(G)$ and lower $I(D)/I(G)$

ratios, indicating a reduced number of graphene layers and fewer defects in graphene sheet.

3. The sheet resistance of laser-induced graphene as low as $100 \Omega/\text{sq}$ is required to be deposited directly/uniformly by a metal via electroplating.

APPROBATION

The research results presented in this thesis were published in two scientific papers [A1-A2], presented at five international conferences [C1-C5] and two national conferences [P1-P2].

Scientific papers that were published:

A1. Fiodorov, V., Ratautas, K., Mockus, Z., Trusovas, R., Mikoliūnaitė, L., Račiukaitis, G. (2022). *Laser-assisted selective fabrication of copper traces on polymers by electroplating*. Polymers, 14(4), 781.

A2. Fiodorov, V., Trusovas, R., Mockus, Z., Ratautas, K., Račiukaitis, G. (2023). *Laser-induced graphene formation on Polyimide using UV to mid-infrared laser radiation*, Polymers, 15(21), 4229.

International conferences where the results of this thesis were presented:

C1. Fiodorov, V., Ratautas, K., Mockus, Z., Trusovas, R., Račiukaitis, G. *Laser-assisted selective fabrication of copper traces on polymers by electroplating*. Open Readings 2021, Vilnius, Lithuania (2021). Poster.

C2. Fiodorov, V., Ratautas, K., Mockus, Z., Trusovas, R., Račiukaitis, G. *Laser-assisted selective fabrication of copper traces on polymers by electroplating*. High Power Laser Ablation (HPLA), Santa Fe, USA (2021). Poster.

C3. Fiodorov, V., Ratautas, K., Mockus, Z., Trusovas, R., Račiukaitis, G. *Laser-assisted selective fabrication of copper traces on polymers by electroplating*. Laser Precision Microfabrication (LPM), Hirosaki, Japan (2021). Oral.

C4. Fiodorov, V., Ratautas, K., Mockus, Z., Trusovas, R., Račiukaitis, G. *Laser-assisted selective fabrication of copper traces on polymers by electroplating*. Laser in Manufacturing (LIM), Munich, Germany (2021). Oral.

C5. Fiodorov, V., Ratautas, K., Mockus, Z., Trusovas, R., Mikoliūnaitė, L., Račiukaitis, G. *Laser-assisted selective fabrication of copper traces on polymers by electroplating*. 5th International Conference on Material Science and Nanotechnology, London, United Kingdom (2022). Oral.

National conferences where the results of this thesis were presented:

P1. Fiodorov, V., Ratautas, K., Mockus, Z., Trusovas, R., Račiukaitis, G. *Laser-assisted selective fabrication of copper traces on polymers by electroplating*. FizTech 2021, Vilnius, Lithuania (2021). Oral.

P2. Fiodorov, V., Ratautas, K., Mockus, Z., Trusovas, R., Mikoliūnaitė, L., Račiukaitis, G. *Laser-assisted selective fabrication of copper traces on polymers by electroplating*. Fiztech 2022, Vilnius, Lithuania (2021). Oral.

AUTHOR CONTRIBUTION

The author of the thesis made the main experimental and theoretical work of this study:

- Design of the experiment;
- Sample preparation and laser fabrication of materials;
- Initial electroplating experiments;
- Sheet resistance measurements;
- Microscopic analysis of laser-treated samples;
- Writing papers for publication;
- Preparation of presentations at conferences.

CO-AUTHOR CONTRIBUTION

- Dr. Gediminas Račiukaitis gave ideas on how to proceed with the experiments and revised scientific papers.
- Dr. Zenius Mockus assisted with metal electroplating on laser-formed graphene layers.
- Dr. Romualdas Trusovas assisted in Raman spectra measurements on laser-formed graphene layers and helped in the preparation of scientific papers.
- Dr. Karolis Ratautas advised in theoretical modelling of heat conduction on the sample surface after laser irradiation.
- Dr. Lina Mikoliūnaitė assisted in the analysis of Raman spectra of samples.

1. LITERATURE OVERVIEW

1.1. Polymers

Polymers play a crucial role in our daily lives and have a significant impact on various industries, including household textiles, medicine, and electronics. These versatile materials possess unique properties that make them valuable for specific applications. They can be flexible or rigid, transparent, or opaque, and exhibit electrical conductivity or insulating properties. Scientists and engineers can adapt the properties of polymers during synthesis to suit various needs.

Polymers are large molecules composed of repeating monomer units covalently bonded together to form long chains, resulting in their characteristic high molecular weight. They can consist of hundreds or even thousands of monomers. Polymers can be found in a wide range of materials and substances, both naturally occurring and synthetic [29].

Natural polymers occur naturally in living organisms and can be derived from natural sources. Examples of natural polymers include proteins found in hair, skin, and muscles, as well as cellulose, the main component of plant cell walls, and wood. On the other hand, synthetic polymers are human-made and include well-known examples such as polyethylene (PE), polypropylene (PP), polyvinyl chloride (PVC), polystyrene (PS), and polyethylene terephthalate (PET). These synthetic polymers are commonly used in packaging, flooring materials, pipes, plastic bags, bottles, and various other products.

Polymers can also be classified based on their main chain structure (see **Figure 2**):

- Linear polymers. The monomer units are connected in a long, continuous chain without any branching or cross-linking in linear polymers. This simple, straight-line arrangement is seen in polymers like high-density polyethylene (HDPE) and polyvinyl chloride (PVC).
- Branched polymers. Branched polymers have some monomer units forming the main chain, but there are also smaller side chains or branches attached to them, resulting in a more complex structure. Low-density polyethylene (LDPE) and certain forms of polypropylene (PP) are examples of branched polymers.
- Cross-linked polymers. Cross-linked polymers form a three-dimensional network with covalent bonds between different polymer chains. This cross-linking enhances their strength and rigidity. Cross-linked polymers, such as epoxy resins and phenolic resins, cannot be

re-melted or re-shaped after curing, making them thermosetting plastics.

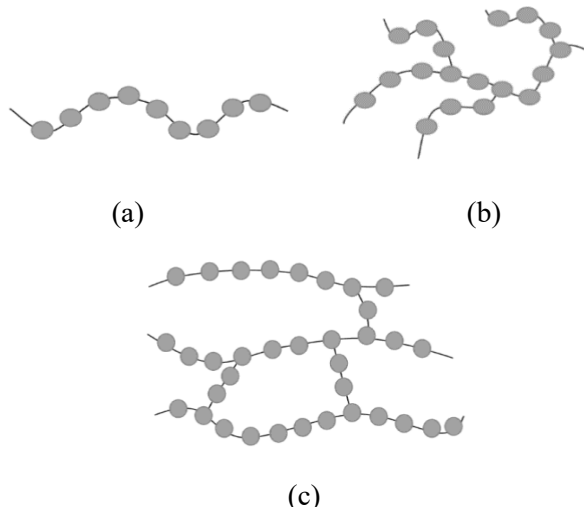


Figure 2. Polymer type by their structure: (a) linear; (b) branched; (c) cross-linked [30].

Polymers can also be categorized based on their mechanical properties, which are affected by the arrangement and structure of their polymer chains. These mechanical properties are crucial in determining the suitability of polymers for various applications. Below are some common classifications based on their mechanical behavior:

- **Elastomers.** Elastomers are polymers known for their exceptional elasticity, capable of undergoing significant deformation under stress and returning to their original shape when the stress is released. This "rubbery" behavior is due to their long, coiled polymer chains, which could be stretched and recoiled back to their original configuration. Examples of elastomers include natural rubber, neoprene, and silicone rubber.
- **Thermoplastics.** Thermoplastics are polymers that become pliable when heated and solidify when cooled. They can be molded and reshaped multiple times without undergoing chemical degradation. The linear or slightly branched polymer chains in thermoplastics can slide past each other, allowing for their plasticity and reusability. Examples of thermoplastics include polyethylene, polypropylene, polyvinyl chloride, and polystyrene.

- Thermosetting plastics. Thermosetting plastics, or thermosets, are polymers that undergo a chemical reaction during curing, forming a three-dimensional cross-linked network. Once fully cured, thermosets cannot be remelted or reshaped, making them rigid and strong. Their strong cross-linked structure prevents significant deformation under heat or stress. Examples of thermosetting plastics include epoxy resins, phenolic resins, and melamine formaldehyde.
- Fiber-forming polymers. These polymers possess high tensile strength and can be drawn into long, thin fibers. They are commonly used in textiles, ropes, and structural composites. Examples of fiber-forming polymers include nylon (PA), polyester (PET), and polyaramids (e.g., Kevlar).
- High-performance polymers. High-performance polymers exhibit exceptional mechanical properties, such as high strength, stiffness, and temperature resistance. They are often utilized in demanding applications, including aerospace, automotive, and engineering. Examples of high-performance polymers include polyether ether ketone (PEEK), polyimide (PI), and polytetrafluoroethylene (PTFE or Teflon).
- Plasticizers and reinforcements. Some polymers can be modified by adding plasticizers to increase flexibility, making them more suitable for specific applications. Additionally, incorporating reinforcements, such as fiberglass or carbon fibers, significantly improves the strength, stiffness, and other mechanical characteristics of the polymer.

By understanding the mechanical properties of different polymers, engineers, and designers can select the appropriate materials for specific purposes, optimizing performance and functionality in various industries [30-32].

1.2. Conductive polymers

Conductive polymers, also referred to as intrinsically conducting polymers (ICPs), form a distinct category among polymers as they possess the ability to conduct electricity. This characteristic sets them apart from most conventional polymers, which act as insulators and endow them with exceptional value in various electronic and electrical applications.

The electrical conductivity in conductive polymers stems from electron delocalization along the polymer chain, leading to a partial overlap of electron orbitals. This effect is achieved by introducing conjugated double bonds or

heteroatoms into the polymer's structure. These conjugated systems facilitate the movement of charge carriers (electrons or holes) within the polymer, giving rise to its electrical conductivity.

One of the most well-known conductive polymers is polyaniline; other common conductive polymers include polythiophene (PTs), polypyrrole (PPy), and polyacetylene (PA) [32-33].

1.3. Polymers with conductive impurities

Polymers with electrically conductive impurities are a type of composite material where polymers are combined with electrically conductive particles or fillers. Due to these conductive additives, the plastic matrix gains electrical conductivity, creating a material suitable for applications that demand both the mechanical characteristics of plastics and electrical conduction capabilities. Various types of electrically conductive fillers can be used in plastics, including:

- Carbon-based fillers. Carbon black, carbon nanotubes (CNTs), and graphene are popular choices for conductive polymers.
- Metal fillers. Incorporating metal particles like silver, copper, aluminum, or nickel into plastics produces electrical conductivity.
- Conductive polymers. In some instances, conductive polymers can act as both the matrix material and the electrically conductive filler.

The electrical conductivity of polymers generally increases as the concentration of conductive impurities rises. This is because carbon materials, such as carbon black, carbon fibers, carbon nanotubes, graphene, or metals (like metal powders, flakes, or nanoparticles) possess high electrical conductivity. When these conductive additives disperse within the polymer matrix, they create a network of conductive pathways, enabling electrons to flow. At lower concentrations of additives, the conductive pathways may not be well connected, resulting in relatively low electrical conductivity of the composite material. However, the probability of forming a continuous percolating network increases as more impurities are added. This percolating network provides an efficient pathway for electron transport throughout the composite. Consequently, a critical concentration of impurities, known as the percolation threshold, beyond which the electrical conductivity of the polymer composite increases significantly. Below this threshold, the composite behaves as an insulator, while it acts as a conductor above it. The specific percolation threshold can vary depending on the type of additives, their shape, and the properties of the polymer matrix (see **Figure 3**).

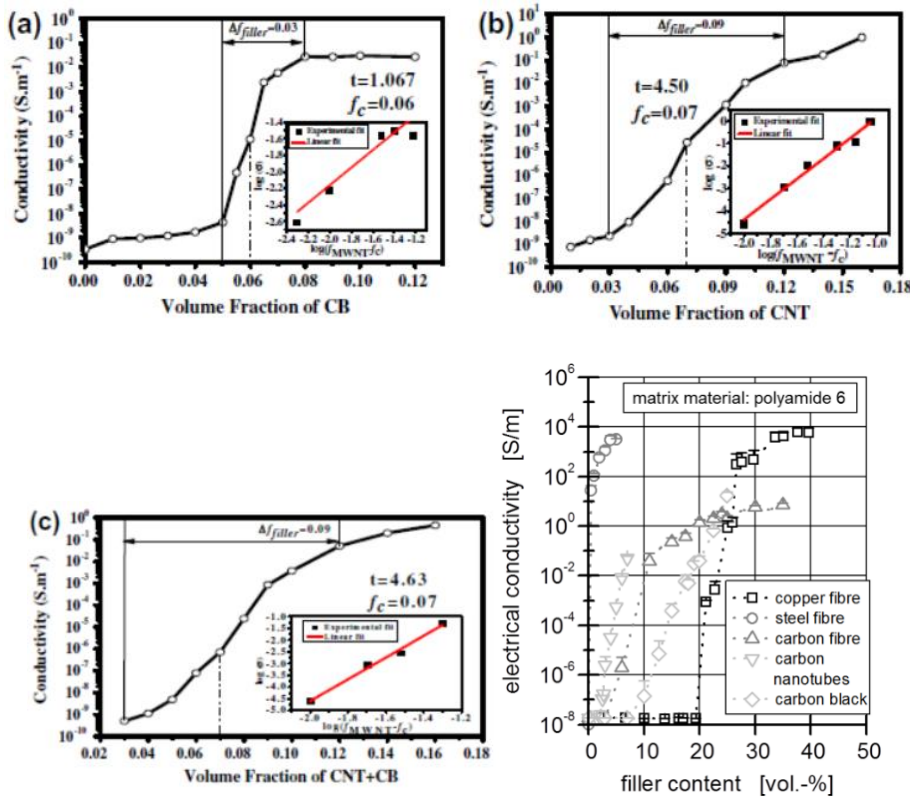


Figure 3. The electrical conductivity of TPE composite dependence for three types of fillers: (a) carbon black (CB); (b) carbon nanotubes (CNT); (c) hybrid fillers combining carbon nanotubes and carbon black (CNT-CB); (d) electrical conductivity of the polyamide-6 polymer doped with different types of fillers [34].

Doping polymers with conductive impurities requires careful consideration to strike a balance. While increasing the concentration of conductive impurities enhances electrical conductivity, excessively high concentrations can lead to issues like reduced mechanical properties and increased brittleness of the composite material. Therefore, precise control over the amount of impurities is essential to achieve the desired level of electrical conductivity without compromising other important properties of the polymer [34-36].

1.4. High-performance polymers

High-performance polymers, also known as advanced engineering plastics, belong to a class of polymers characterized by their exceptional mechanical,

thermal, chemical, and electrical properties. These specialized plastics are engineered to surpass the capabilities of conventional materials and standard plastics, making them highly needed for demanding and specialized applications. Their unique combination of properties makes them invaluable in industries that confront extreme conditions, high stress, and harsh environments. The critical features of high-performance plastics encompass superior mechanical strength, thermal stability, chemical resistance, low friction or outstanding wear resistance, flame retardancy, and more. These remarkable attributes make high-performance polymers pivotal in driving innovation and technological advancements across various industries, offering versatile solutions in numerous challenging scenarios.

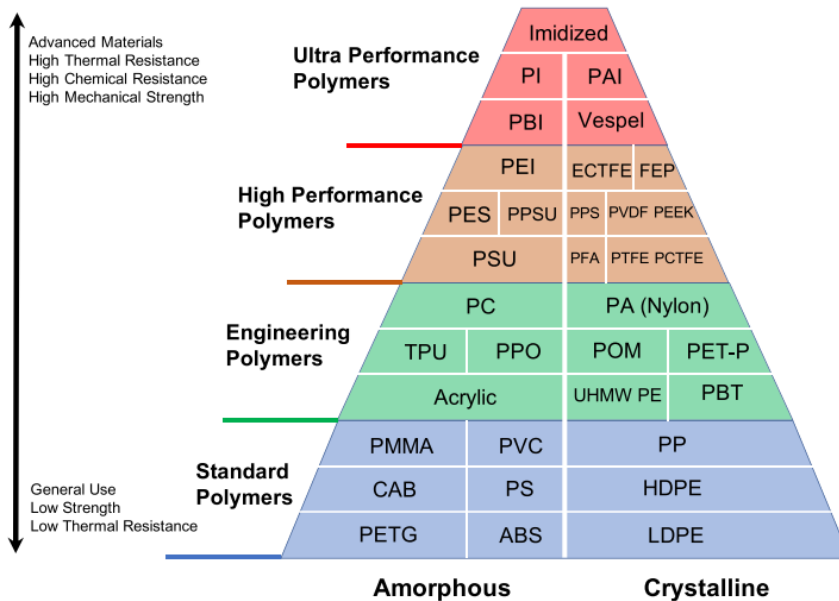


Figure 4. Hierarchy of polymer materials according to their thermal, chemical, and mechanical stability [37].

The most used high-performance polymers are polyether ether ketone (PEEK), polyimides (PI), polyphenylene sulfide (PPS), liquid crystal polymers (LCP), polysulphones (PSU), and polyetherimide (PEI) [38-39].

1.5. Polyimides

Polyimide (PI), one of the most recent advanced materials, attracts particular attention. Constructing spacecraft and satellites, for instance, necessitates materials that can withstand high surface temperatures, possess lightweight

characteristics, and exhibit high dimensional stability. For example, polyimide materials can withstand temperatures up to 670 K without degradation. Standard polymers, like polypropylene (PP), polymethyl methacrylate (PMMA), or acrylonitrile butadiene styrene (ABS), cannot withstand even 373 K temperature. The tensile strength of PI is up to 230 MPa, whereas standard polymers have only around 50 MPa. Modern military and civil aircraft extensively use such polymers, like polyimide, gradually replacing conventional materials like metals, glass, and ceramics. Additionally, these polymers find applications in the microelectronics and optoelectronics industries [40, 41].

Polyimide (PI) represents a novel class of polymers characterized by their inherently rigid chains, making them of significant commercial importance [42]. These applications span a wide range, including microelectronics, high-temperature matrices, and adhesives for gas separation membranes. The synthesis of PI involves the incorporation of highly stable and rigid heterocyclic ring systems into the polymer chain. PI is available in various forms, such as plastics, films, laminating resins, insulating coatings, and high-temperature structural adhesives. The thermal stability of polyimides arises from the presence of an inert imide ring and strong interchain interactions, which result in high cohesion among the polymer chains. **Figure 5** illustrates a representative structure of a polyimide.

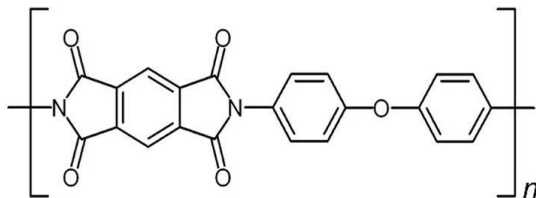


Figure 5. The structural element of polyimide molecule [43].

Polyimides can be broadly categorized into three groups based on the monomers from which they are derived: fully aromatic polyimides, semi-aromatic polyimides, and fully aliphatic polyimides (see **Figure 6**) [44]. Aromatic polyimides are synthesized from aromatic dianhydride and a diamine. Semi-aromatic polyimides incorporate one aromatic monomer (either dianhydride or diamine), while the other monomer is aliphatic. The third category comprises polymers formed by combining aliphatic dianhydrides and diamines.

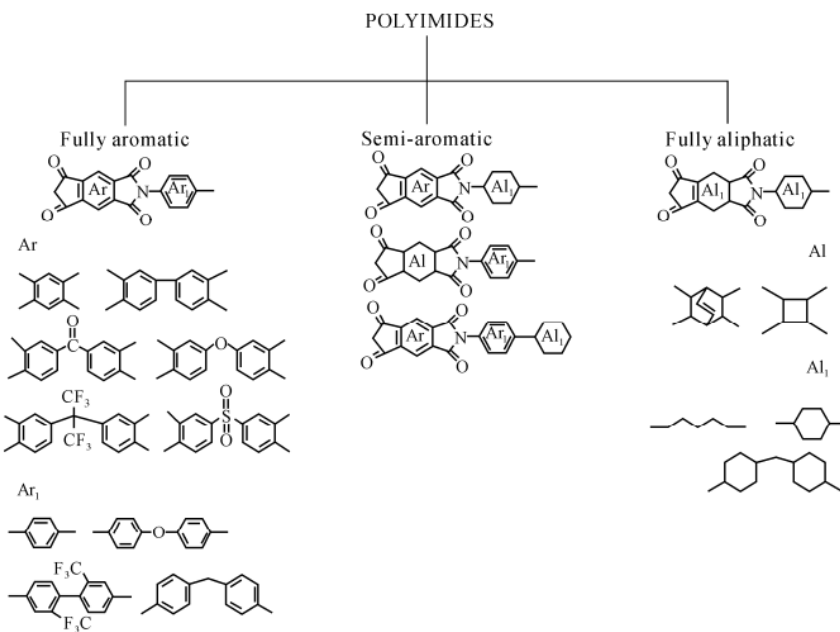


Figure 6. Categories of Polyimides: fully aromatic (left), semi-aromatic (center) or fully aliphatic (right) [45].

Aromatic polyimides (PIs) are commonly found in various commercial polyimide products, including G.E.'s Ultem® and DuPont's Kapton®.

1.6. Biodegradable polymers

Biodegradable polymers, often referred to as biodegradable plastics, are a class of polymer materials capable of undergoing natural biological processes that break them down into simpler components like water, carbon dioxide, and biomass. This stands in strong contrast to conventional plastics that can persist in the environment for centuries. The primary purpose of biodegradable polymers is to reduce the environmental consequences of plastic waste.

There are two primary categories of biodegradable polymers (see **Figure 7**):

- Natural polymers. These polymers originate from renewable sources, such as plants (e.g., corn, potatoes, sugarcane) or microorganisms (e.g., bacteria, algae). Notable examples of bio-based biodegradable polymers include polylactic acid (PLA), polyhydroxyalkanoates (PHA), and starch-based plastics. These polymers can be broken down by microorganisms in composting conditions.
- Synthetic biodegradable polymers. These polymers are manufactured through chemical processes and engineered to break down more

quickly in the environment than traditional plastics. Polyethylene oxide (PEO), polycaprolactone (PCL), and polybutylene adipate terephthalate (PBAT) are among the synthetic biodegradable polymers.

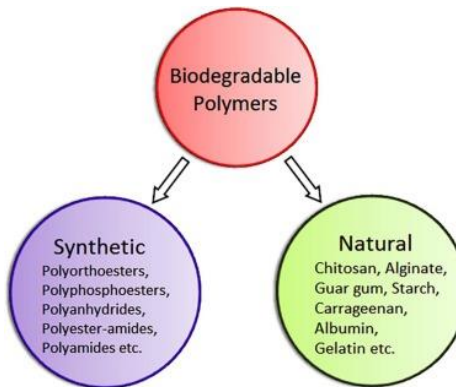


Figure 7. Biodegradable polymers could be grouped into synthetic and natural polymers [46].

It is essential to recognize that while biodegradable polymers offer advantages in restraining plastic waste and reducing environmental harm, their ability to biodegrade often depends on specific circumstances. For instance, certain biodegradable plastics require controlled conditions found in industrial composting facilities, including regulated temperature, moisture, and microbial activity, for efficient breakdown. The process could be significantly slower in natural settings like oceans or landfills, where conditions might not be optimal for biodegradation.

Biodegradable polymers have gathered attention as part of efforts to reduce plastic pollution and soften the ecological impact of plastic waste. Nonetheless, achieving a comprehensive resolution to plastic pollution also includes reducing plastic consumption, enhancing recycling systems, and choosing sustainable packaging alternatives [46-47].

1.7. Carbon and its forms

1.7.1. Carbon allotropes

Carbon's versatile valency enables the creation of numerous allotropes, signifying distinct structural manifestations of the same elemental composition. Among the earliest known carbon variants are diamond and graphite. Recent decades have witnessed the revelation and exploration of

additional allotropes, encompassing configurations like spherical Buckminster, fullerene, carbon nanotubes, nanorods, and planar graphene. Different carbon allotropes have different properties, i.e., diamond is colorless, transparent, and extremely hard, whereas graphite is black and opaque and has a high electrical conductivity. Other less common forms of carbon allotropes could exist at extremely high temperatures and pressures. Currently, around 500 hypothetical allotropes of carbon are known, according to the Samara Carbon Allotrope Database (SACADA). The most noteworthy recent breakthrough in carbon allotrope exploration has been the discovery of graphene [48, 49].

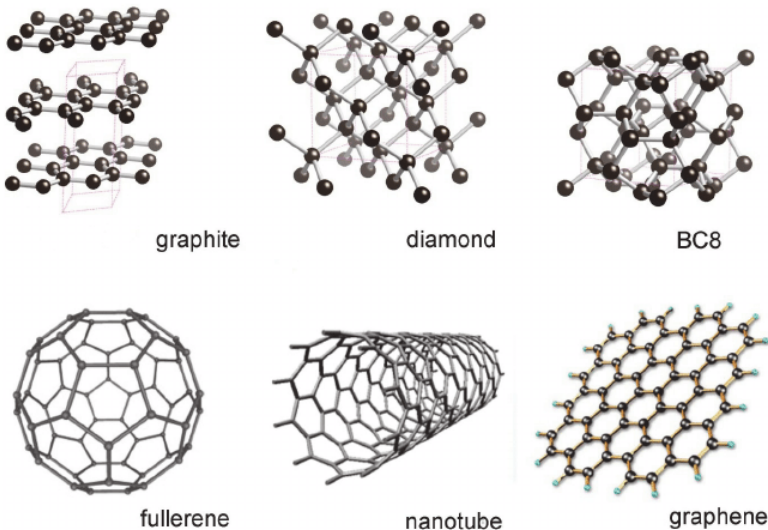


Figure 8. Six of the most common carbon allotropes are shown [48].

1.7.2. History of graphene, its structure, and properties

In 1947, Canadian physicist P. R. Wallace put forth the theoretical concept of graphene - a single layer of carbon atoms arranged in a two-dimensional honeycomb lattice. In 1960, A. R. Ubbelohde and F. A. Lewis accomplished the isolation of a monolayer of graphite atoms and highlighted graphite's composition of layered structures, forming networks of hexagonal carbon atom rings. Consequently, the compact arrangement of a single atomic carbon layer in graphite could form a two-dimensional honeycomb lattice, which is now recognized as graphene. The term "graphene" was formally introduced by R. Boehm et al. in 1994. In 2004, K. Novoselov and A. Geim achieved a significant breakthrough. They successfully isolated and investigated a single-atom-thick crystallite, known as graphene, from bulk graphite. Using the now-

famous Scotch tape technique, they transferred these graphene layers onto a thin silicon dioxide substrate situated on a silicon wafer. This marked the point at which the properties of graphene material were fully realized. It's worth noting that the initial extraction of graphene from graphite was accomplished through a process called micromechanical cleavage. In recognition of their pioneering experiments on the two-dimensional material graphene, they were jointly awarded the Nobel Prize in Physics in 2010 [8, 50-51].

Graphene, a carbon nanomaterial, comprises two-dimensional layers consisting of a single-atom-thick planar sheet of sp^2 -bonded carbon atoms densely arranged in a honeycomb lattice crystalline structure. The arrangement of graphene's structure has similarities to numerous interconnected benzene rings, where carbon atoms take the place of hydrogen atoms (see **Figure 9**). Notably, the absence of oxygen groups renders graphene hydrophobic. Additionally, it is classified as a carbon allotrope, characterized by a planar array of sp^2 -bonded atoms with a molecular bond length measuring 0.142 nm. When stacked, these graphene layers give rise to graphite, exhibiting an inter-planar spacing of 0.335 nm.

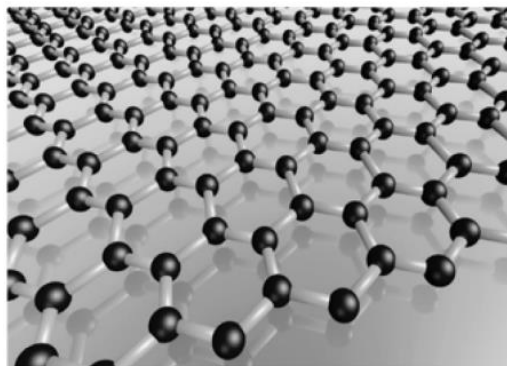


Figure 9. Graphene is a hexagonal lattice on the atomic scale constructed from carbon atoms [50].

In contrast, graphite forms a three-dimensional structure due to its stacking arrangement, whereas graphene remains a two-dimensional material, only one atom thick. Graphene's bonding is a result of sp^2 hybridization. It features a solitary π orbital and three σ bonds that run perpendicular to the plane. The robust σ bonds within the plane establish the rigid hexagonal backbone structure, while the π bonds extending out of the plane determine interactions between distinct graphene layers. Nevertheless, deviations in graphene's structure primarily arise from the deficiency of one or more sp^2 carbon atoms or the inclusion of one or more disparate atoms with sp^3

hybridization. By establishing covalent bonds within the plane, carbon atoms create σ -bonds with three adjacent carbon atoms alongside an out-of-plane π bond. This complicated arrangement of sp^2 carbon atoms is responsible for providing graphene with its distinct and exceptional properties:

Tensile strength. The tensile strength of graphene is approximately 125 GPa, while its elastic modulus stands at 1.1 TPa. This translates to graphene's strength being 100 times greater than that of steel.

Thermal conductivity. Graphene showcases extraordinary thermal conductivity, which empowers it to transmit heat proficiently. This characteristic proves invaluable for tasks related to heat management and dissipation.

Electrical conductivity. Graphene is an outstanding electricity conductor thanks to its distinct electronic structure. The carbon-carbon bonds stimulate delocalized π electrons within its hexagonal lattice, enabling their free movement across the structure and facilitating efficient electrical conduction.

Optical properties. Graphene is nearly transparent, and this characteristic, when coupled with its electrical conductivity, makes it a fitting choice for creating transparent conductive films essential in applications like displays and solar cells [51-54].

1.7.3. Graphene applications

Graphene finds application in energy storage devices like batteries and supercapacitors due to its substantial surface area. Within Li-ion batteries, graphene is commonly used as an anode and has a capacity of approximately 1000 mAh/g, a value three times greater than that of a graphite electrode. Additionally, graphene contributes to prolonged battery lifespans and accelerated recharge times, often in seconds. Finally, its flexibility further allows graphene to serve as a solid-state supercapacitor integrated into textiles, facilitating advancements in wearable electronics [55].

Graphene nanoporous membranes have the potential to excel in applications like water desalination and filtration, achieving efficiencies spanning from 33 % to 100 %, depending on pore size and applied pressure. D. C. Tanugi and J. C. Grossman conducted classical molecular dynamics studies, revealing that water could pass through graphene membranes at rates reaching up to 100 l/cm² per day — significantly surpassing the diffusion rates of reverse osmosis (RO) membranes (see **Figure 10**).

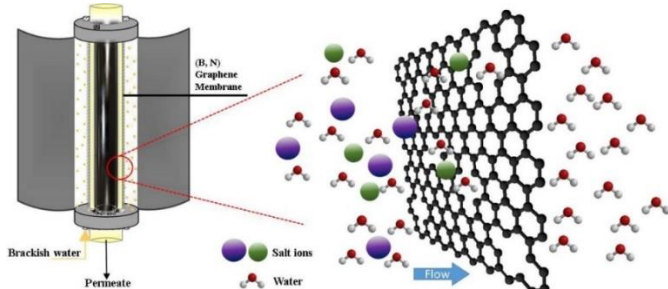


Figure 10. Graphene membrane for water filtration [56].

Graphene exhibits remarkably high carrier mobility at room temperature, and this characteristic renders it suitable for adaptation in transistors. The inception of graphene's field-effect transistors was introduced by M. C. Lemme et al. [57, 58]. In their study, the drain current was controlled by manipulating the top gate. It was observed that monolayer graphene showed superior field-effect attributes compared to silicon transistors.

Nowadays, solar cells have assumed a crucial role in generating electrical power. Their efficiency is a pivotal factor in converting light energy into electricity. S. M. Shin et al. [59] enhanced the efficiency of photovoltaic cells by incorporating carbon nanotubes into the graphene structure. During light absorption, a minor hole transfer occurring along carbon nanotubes led to a notable efficiency increase, reaching 15.2 %.

Graphene is extensively used in biomedicine, with a wide array of applications. Recently, nano-graphene has been engineered for prospective use in imaging and photothermal therapy. The sensing capabilities of graphene-based electrodes can be adjusted by altering the surface chemistry of graphitic materials, leading to diverse biosensing applications encompassing the detection of organic molecules, microbial cells, and biomolecules [60, 61].

1.7.4. Graphene characterization methods

The main methods for the characterization of graphene properties, defects, morphology, and layers are Raman spectroscopy, Scanning electron microscope (SEM), transmission electron microscope (TEM), and X-ray diffraction (XRD).

Raman spectroscopy is used to analyze the layers and structural quality of graphene and is the main graphene characterization method. The interaction of monochromatic Raman radiation with molecular vibrations in graphene leads to radiation scattering and subsequent shifts. Three primary peaks are

evident in the Raman spectrum of graphene: D, G, and 2D peaks. The D peak, situated at 1350 cm^{-1} , signifies a disorder in sp^2 hybridization. The G peak, located at 1580 cm^{-1} , corresponds to lattice vibration, while the 2D peak, at 2700 cm^{-1} , originates from second-order Raman scattering at the Dirac point (see **Figure 11(a)**). The $I(\text{D})/I(\text{G})$ ratio increases with heightened graphene disorder due to elastic scattering from greater defect intensity. Conversely, a more amorphous carbon structure reduces the $I(\text{D})/I(\text{G})$ ratio.

Transmission electron microscopy (TEM) is the predominant technique for assessing graphene's structural quality and layer count. TEM images result from the interaction of an electron beam with the material under study. In **Figure 11(b)**, the TEM image reveals graphene's layer count in dimethyl sulfoxide. Dark fringes representing 3, 4, 5, and 6 graphene layers can be observed. These graphene layers align parallel to the electron beam.

Scanning electron microscopy (SEM) is used to study graphene's morphology. SEM imaging provides insights into impurities, graphene folding, and synthesis-related discontinuities (see **Figure 11(c)**). Nonetheless, its resolution for ultrathin graphene layers is limited.

The X-ray diffraction (XRD) technique is primarily used to identify material phases based on unit cell dimensions. **Figure 11(d)** shows the XRD patterns of graphene, graphite oxide, and graphite. A sharp, pronounced diffraction peak for graphite appears at 26.6 degrees. Subsequently, this peak shifts to 13.3 degrees, signifying the presence of oxygen molecules. Graphene synthesis is successful if there is no peak after fabrication [62].

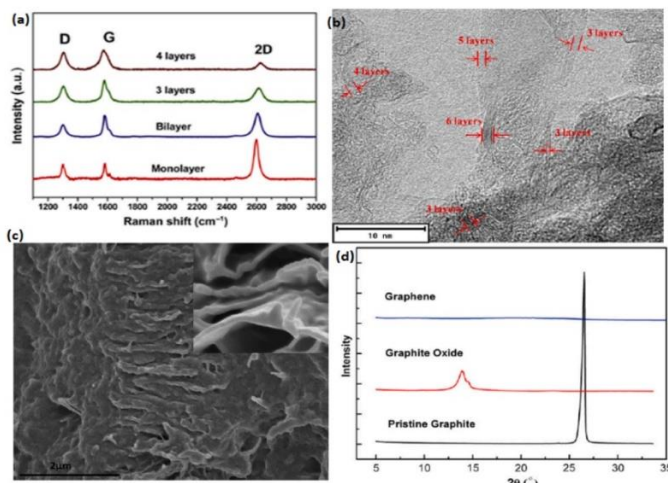


Figure 11. Graphene characterization by: (a) Raman spectra; (b) high-resolution TEM imaging; (c) SEM image of graphene structure, and (d) XRD image of graphite, graphite oxide, and graphene [62].

1.8. Graphene formation methods

1.8.1. Mechanical methods

Production of graphene started with the fundamental and pioneering technique of mechanical exfoliation. Using ordinary adhesive tape delicately, graphite layers were peeled off from a bulk graphite sample until a single graphene layer was obtained. This groundbreaking discovery opened the door to extensive research and exploitation of graphene's extraordinary properties across a wide range of applications. Other mechanical graphene formation methods include peeling graphite layers using ultra-sharp diamonds or grinding graphite between balls until graphene flakes are formed to achieve nano-thickness [63-66].

1.8.2. Graphene formation by chemical vapor deposition

Chemical vapor deposition (CVD) of graphene is a widely used method for the controlled growth and synthesis of graphene layers on various substrates. In this process, graphene is formed by the catalytic decomposition of a carbon-containing gas in a high-temperature environment. The CVD method offers advantages in terms of scalability, reproducibility, and the potential for large-scale production of high-quality graphene. The CVD method for graphene formation involves the following steps. The process begins with substrate preparation, where graphene will be grown. Usually, substrates include copper, nickel, silicon carbide, or various metal foils. Then, the substrate is placed inside a high-temperature reactor, such as a quartz tube or furnace, and heated to a specific temperature (usually from 530 K to 830 K). Later, carbon-containing gas, such as methane (CH_4), ethylene (C_2H_4), or acetylene (C_2H_2), is filled into the reactor [67, 68]. The carbon precursor gas dissociates at high temperatures, releasing carbon atoms onto the substrate surface, where they form graphene islands. The carbon atoms arrange themselves into a hexagonal lattice structure, forming a single graphene layer. The growth process is controlled by adjusting the reaction parameters, such as temperature and gas flow rates, to achieve the desired number of graphene layers. Once the graphene growth is complete, the reactor is cooled down, and the graphene-coated substrate is retrieved [69].

1.8.3. Epitaxial growth

Epitaxial growth is a technique used to create graphene on a substrate with a similar atomic arrangement [70]. During this process, carbon atoms self-

organize into a high-quality and well-ordered graphene layer on the substrate's surface. The preferred substrate for epitaxial growth of graphene is silicon carbide (SiC) because of its structural compatibility with graphene. SiC possesses a hexagonal lattice structure, just like graphene's carbon atoms, facilitating the natural arrangement of carbon atoms on the SiC surface to form a single graphene layer. Epitaxial growth provides several benefits in producing graphene. It enables precise control over the size, shape, and orientation of graphene domains, resulting in exceptional electronic and structural properties. Furthermore, the SiC substrate serves as a stable and insulating platform for graphene, which is crucial for various applications in the fields of electronics and optoelectronics [71, 72].

1.8.4. Chemical reduction of graphene oxide

Reduced Graphene Oxide (rGO) is derived from graphene oxide through a reduction process. Graphene oxide is an oxidized form of graphene containing various oxygen-containing functional groups like epoxy, hydroxyl, and carboxyl, making it hydrophilic and easily dispersible in water. The reduction process eliminates most of these oxygen groups, restoring graphene's sp^2 hybridized carbon lattice and reviving some remarkable properties [73]. The chemical reduction of graphene oxide (GO) is a widely employed technique to produce reduced graphene oxide (rGO). It involves utilizing a chemical reducing agent to strip away the oxygen-containing functional groups from GO, resulting in the formation of rGO with its sp^2 hybridized carbon lattice restored and a reduction in oxygen functional groups [74, 75].

1.8.5. Laser-induced graphene

Laser-induced graphene (LIG) is a unique and innovative technique to create graphene directly on various substrates using laser irradiation. It was discovered by researchers at Rice University in 2014 and has since gained attention as a simple and scalable method for graphene production [76]. To form graphene, a laser beam is directed onto the substrate. The laser's energy causes the carbon-based material to undergo a photothermal reaction, where the localized heat generated by the laser triggers the conversion of the carbon material into graphene. During laser irradiation, the carbon atoms in the coated material are rearranged into a two-dimensional honeycomb lattice structure, resulting in the formation of graphene directly on the substrate surface. The laser parameters, such as power, lasing duration, and scanning speed, can be adjusted to control the thickness and quality of the formed graphene [77-80].

The laser-induced graphene technique offers several advantages, such as simplicity and rapid processing. Most importantly, LIG can be patterned into specific shapes, making it useful for flexible electronics and sensors [81, 82].

1.9. Interaction of laser radiation with polymers

1.9.1. Polymer absorption of laser radiation

The interaction between laser radiation and a material typically starts with the absorption of laser radiation [83, 84]. In the infrared, visible, and near-ultraviolet laser frequency spectrums, radiation absorption is governed by the Bouguer-Lambert law:

$$I(z) = (1-R)I_0 \exp(-\alpha z), \quad (1)$$

where I_0 is the intensity of the laser beam incident on the sample, R is the reflection coefficient, α is the absorption coefficient of the material, and z is the coordinate measured into the depth of the material.

The laser intensity dissipated in a layer of thickness z is:

$$\Delta I = I_0(1-R)(1-\exp(-\alpha z)), \quad (2)$$

At a certain amount of absorbed radiation, laser ablation occurs. Laser ablation is a process in which the material is removed from a solid due to absorbed laser radiation. There exist a few ablation mechanisms depending on the laser wavelength used:

- Photochemical ablation. In this case, a laser photon directly breaks a covalent bond in the polymer chain. The energy of photons must exceed the bonding energy of polymers, which typically starts from several electron volts (eV) (approximately 3.6 eV for C-C bonds). The energy of ultraviolet photons is approximately equal to C-C polymer bond energy, so in this case, a single photon could break the polymer bond directly. Direct bond breaking is a very fast process; it takes place at the fs-ps time scale.
- Photothermal ablation. In the case of infrared irradiation, photon energy is too low to break the bond directly. Absorption occurs through vibrational energy level interactions known as photon-phonon transfers. In this case, the energy is transferred to the polymer matrix, leading to a rise in temperature. This type of interaction is called photothermal. In the case of visible laser, both photothermal and photochemical ablation take part [85].

Table 1 shows the bond energies between different atoms of polyimide molecules (polyimide was mainly used in our experiments). There are six different types of bonds in polyimide, with the energies varying from 3.11 eV to 7.58 eV. The most common is the C-C type bond, which occurs 13 times in polyimide molecules.

Table 1. Bond energies in polyimide and photon energies correspond to various laser wavelengths [86, 87].

Bond type	Bond energy, eV	Bond quantity in Polyimide molecule	Laser wavelength, nm	Photon energy, eV
C-C	3.62	13	10600	0.12
C-O	3.62	2	1064	1.165
N-C	3.11	5	532	2.33
C=O	7.58	4	355	3.49
C=C	6.33	9		
H-C	4.25	10		

Numerous plastic materials incorporate additives, such as fillers and colorants, which exhibit linear absorption characteristics when exposed to laser radiation in a broad spectrum, including the 1064 nm wavelength [83]. When ultrashort pulse lasers, such as picosecond and femtosecond lasers, are used, nonlinear absorption can occur. These processes can involve multiphoton absorption and tunneling effects [88].

1.9.2. Nonlinear absorption

At high levels of optical intensity, in the case of ultrashort pulse lasers (with duration ranging from femtoseconds to tens of picoseconds), it becomes possible to overcome the photon energy limitation through the simultaneous absorption of multiple lower-energy photons, resulting in a combined energy that exceeds the bond energy and directly breaks chemical bonds in polymers. In this case, photochemical ablation is possible; nevertheless, the single photon energy is lower than polymer bond energy. These nonlinear absorption phenomena are referred to as multiphoton absorption. The most straightforward form is two-photon absorption, which necessitates the absorption of precisely two photons. However, when the bonding energy of a material exceeds twice the energy of the laser beam's photons, it becomes possible for three-photon absorption and other higher-order absorption processes to take place, as the photon energy is inadequate for linear and two-

photon absorption. The absorption rate for linear absorption is directly proportional to the optical intensity. In the multiphoton absorption case, the absorption rate could be described as:

$$I(z) = \frac{I_0}{1 + \beta z I_0}, \quad (3)$$

where β is the multiphoton absorption coefficient. Multiphoton absorption rates may be minimal for low or moderate optical intensities but can become predominant for very high optical intensities, especially achievable with focused laser pulses [88-90].

1.9.3. Tunnelling process

Another possible way to overcome the bonding energy is tunnel ionization. Tunnel ionization is the phenomenon when the bonding energy reduces due to extremely high-intensity radiation, causing the low-energy photons to break the bonds directly [68-70].

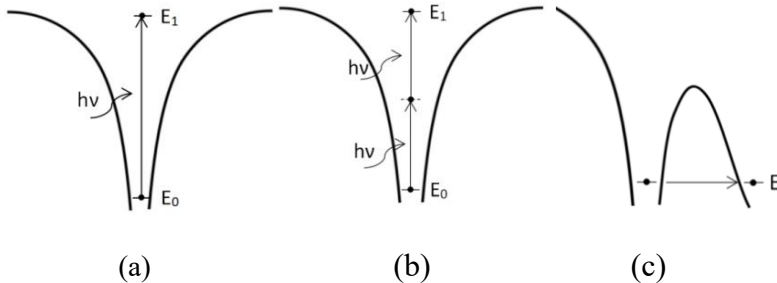


Figure 12. (a) linear absorption, (b) the multiphoton absorption, and (c) the photon tunneling effect [88].

The Keldysh parameter γ describes which nonlinear process will be dominant. The dimensionless parameter is used to quantify the strength of nonlinearity in a material or system:

$$\gamma = \frac{\omega \sqrt{2I_0}}{F}, \quad (4)$$

where ω is the laser frequency, I_0 is the ionization potential, and F is the laser electric field strength.

When $\gamma \ll 1$, the tunnel ionization will be the dominant process (i.e. in the case of low laser frequency and high intensity (10^{14} - 10^{15} W/cm 2)); however,

when $\gamma \gg 1$, multiphoton ionization will be dominant (i.e. in the case of high laser frequency and low intensity ($\sim 10^{13}$ W/cm²)). When γ is approximately equal to 1, both tunnel and multiphoton processes will take effect. The Keldysh parameter is one of the factors that influence the nonlinear response of a material. Additional factors, including the material's unique properties and the intensity distribution of the laser beam, also contribute to shaping the observed nonlinear phenomena in experimental settings [88-90].

1.10. Laser-assisted electric circuit formation methods

The objective of this chapter is to provide a general overview of the current techniques used for generating metallic traces on polymer materials while familiarizing readers with the fundamental issues encountered in this industry. The challenge of metalizing polymers is widely acknowledged and extensively covered in scientific literature. Conventional polymer materials possess insulating properties, making them unsuitable for electroplating.

Several laser-assisted methods are available to produce electric circuits, each with its own set of advantages and limitations. Many of these methods involve electroless plating for metal deposition, which is a considerably slower process compared to electroplating, which was used in our method. Depositing the material by electroless plating could take from a couple of hours to several days, whereas electroplating typically requires only from a few minutes to an hour. Also, not all methods listed below are suitable for 3D materials.

1.10.1. Laser direct structuring

Laser direct structuring (LDS), a method for producing molded interconnect devices (MID), was developed in Germany in 1997 [91]. This is a two-step method: First, a laser writes an electric pattern on the surface of dielectric material. Then, the material is immersed in the electroless copper bath, where copper deposits the laser-activated patterned area (see **Figure 13**).

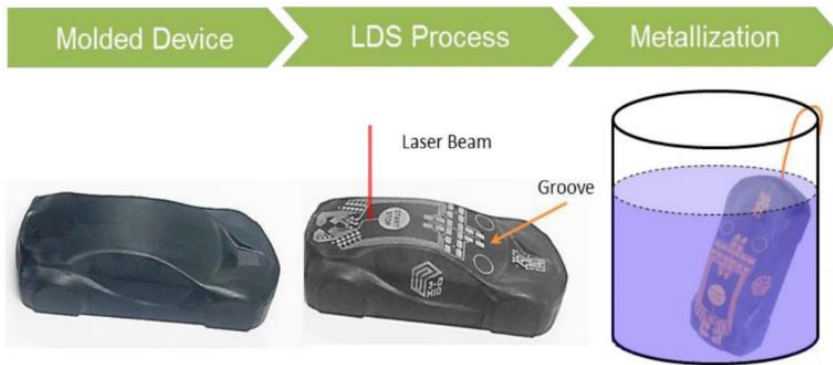


Figure 13. LDS process steps [91].

The advantages of this method are its simplicity, speed, and few processing steps. Conductive pathways can be made on any shape of polymer surface. However, disadvantages include the need for special polymers with metal-containing additives, which can increase the cost of the polymer. Additionally, this method may not be suitable for all electronic applications due to the presence of additives that can cause shielding in high-frequency electronics [92-96].

1.10.2. Selective surface activation induced by laser

Selective surface activation induced by laser (SSAIL) is a novel technique to produce copper tracks. It consists of three steps: first, a picosecond laser modifies the sample surface locally. The second step is the chemical activation of laser-modified areas, and finally, the laser-treated part is immersed into the electroless plating bath, where metal is deposited on the laser-treated areas. The method could produce copper tracks on 3D materials; the materials do not require a special conductive additive, such as in the LDS method. Also, the method could be used not only with polymers but also with other dielectric materials like glass, ceramics, etc. The disadvantage of this method is that it is a slow process, and instability in the plating bath could affect deposition quality [3, 97].

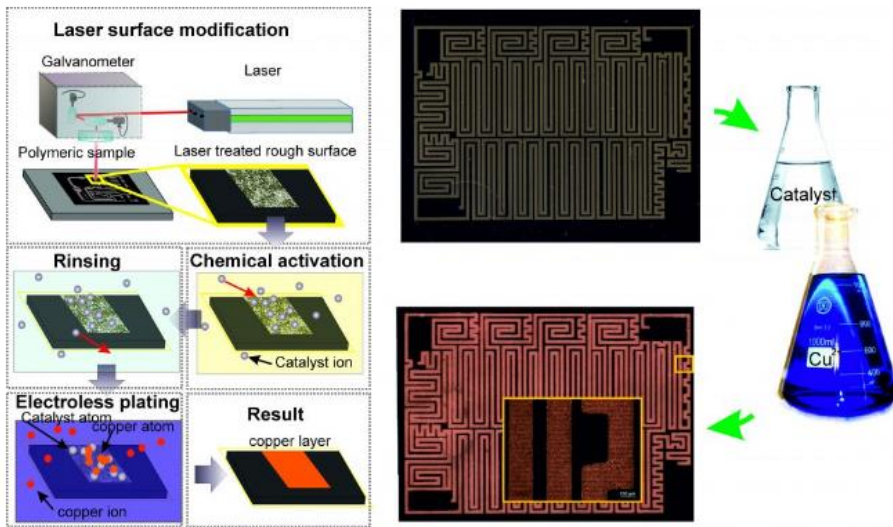


Figure 14. SSAIL process steps [97].

1.10.3. Microscopic integrated processing technology

Microscopic integrated processing technology (MIPTEC) was developed by PANASONIC specifically for the manufacturing of MID [98]. First, a layer of copper is deposited onto the polymer surface by vaporization. Next, laser radiation is used to selectively remove copper from unwanted areas, forming an electrical circuit pattern on the polymer surface. An etching procedure is then carried out to remove copper from the unwanted areas. Finally, nickel and gold layers are deposited onto the surface of the copper tracks by electroless plating. The main disadvantage of this method is that it is a complicated process that requires many steps.

1.10.4. Laser-induced forward transfer

Laser-induced forward transfer (LIFT) is an advanced manufacturing technique that employs laser technology to transfer materials from one substrate to another [99, 100]. The process of laser-induced forward transfer involves the following key steps. Firstly, a thin layer of the material to be transferred, known as the donor material, is applied onto a polymer sample. Then, a pulsed laser is precisely focused onto the donor surface. As the laser energy is absorbed by the donor material, it creates a localized increase in pressure, resulting in the formation of a thin jet or droplet of the material. Finally, the high-pressure jet or droplet of material is then propelled forward

and directed toward the receiving polymer sample, which is positioned near the donor substrate. Upon impact, the material is deposited onto the sample, thus forming the desired pattern or structure.

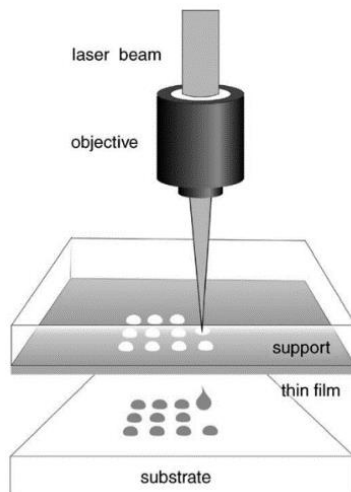


Figure 15. Laser-induced forward transfer scheme [101].

LIFT offers several advantages, including exceptional precision, the capability to transfer diverse materials, and minimal damage to the donor material. This technique finds applications in various fields, such as microfabrication, printed electronics, tissue engineering, and rapid prototyping.

Nevertheless, LIFT also presents some challenges, such as effectively controlling the size and shape of the transferred material and optimizing the transfer efficiency. Researchers continue exploring and refining the LIFT process to address these limitations and enhance its versatility and efficiency for various applications across different industries [102, 103].

1.10.5. Laser-induced surface activation

Laser-induced selective activation (LISA) is a technique that employs lasers to activate specific regions on a substrate surface while keeping other areas unchanged. The typical steps involved in laser-induced selective activation are as follows: firstly, the polymer substrate, polycarbonate, is immersed into a dish with water, and the electric scheme pattern is laser written on the sample surface. Then, the sample is immersed in the palladium solution for a couple of minutes. Finally, the laser-treated sample is immersed in the electroless

plating bath, where copper deposits the laser-affected area (see **Figure 16**) [104-106].

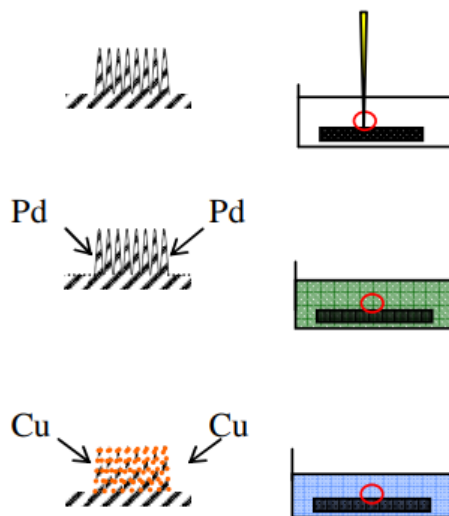


Figure 16. Laser-induced selective activation scheme [105].

1.10.6. Laser-assisted metal deposition from the liquid phase

Laser-assisted metal deposition from the liquid phase is an advanced manufacturing process that uses a laser to melt and deposit metal materials while in a liquid state onto a substrate. The method consists of a few steps. Initially, a metal material, often in the form of wire or powder, is prepared and positioned near the substrate to be coated or built upon. Then, a high-power laser is directed onto the metal material, rapidly heating, and melting it. The laser's intensity and scanning speed are precisely controlled to achieve the desired melting and deposition characteristics. Further, the melted metal material forms a small molten pool on the surface of the substrate. Once deposited, the molten metal rapidly cools and solidifies on the substrate [107-109].

Laser-assisted metal deposition from the liquid phase offers several advantages, including the capability to fabricate complex geometries with exceptional precision and excellent material properties. Additionally, this method allows you to add different alloying elements or additives to the final product. The disadvantages of this method are its costliness, slow speed of the process, and its complexity.

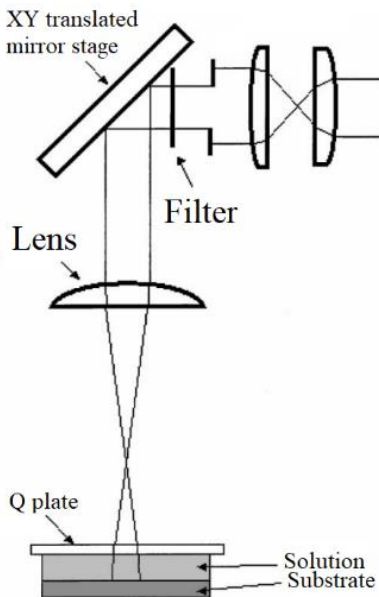


Figure 17. Laser-assisted metal deposition from the liquid phase scheme [107].

1.11. Other electric circuit formation methods

1.11.1. Photolithography

The most common method to produce copper tracks is photolithography. The photolithography process involves several key steps, including alignment of the semiconductor component with the photomask, exposure, hardening, and etching. During alignment, a quartz or glass photomask with the desired electrical circuit pattern is precisely positioned over the semiconductor component. The component is then exposed to UV light, typically with a wavelength of 193 nm, which passes only through transparent areas of the photomask, transferring the circuit pattern to a photoresist layer on the component. The photoresist is then hardened to resist further etching, and unnecessary areas are removed through etching (see **Figure 18**).

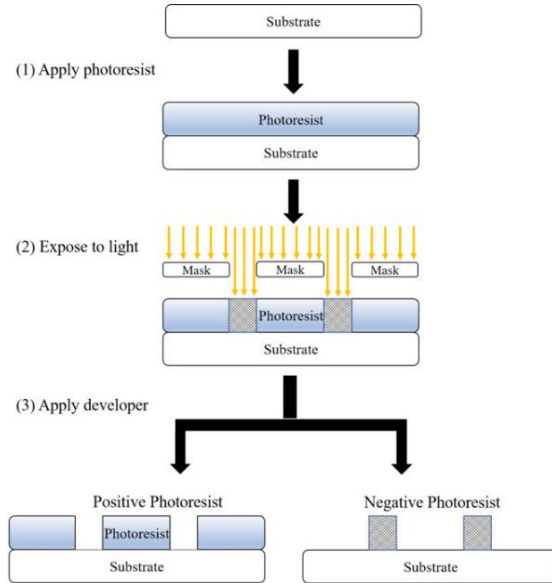


Figure 18. The photolithography process steps [110].

While photolithography is an effective method for mass production of identical components on flat surfaces and is widely used in printed circuit board (PCB) production, it has some limitations. For example, creating a different component with a different electrical circuit pattern requires the creation of a new photomask, which can be expensive. Additionally, the method is complex and requires high precision, such as accurate alignment of the photomask with the sample. Finally, photolithography is primarily suitable for flat surfaces, and current efforts to create electrically conductive pathways on curved surfaces through photolithography have not had much success [111].

1.11.2. Aerosol jet printing

This method contains six steps. At first, aerosol is generated in the chamber using an ultrasonic or pneumatic atomizer (as shown in **Figure 19 (1)**). Then, the carrier gas enters the chamber and transports aerosols with diameters ranging from 1 to 5 μm into the next container, while those aerosols with larger diameters settle back into the solution (see **Figure 19 (2) and (3)**). The aerosols enter the deposition container (see **Figure 19 (4)**). Finally, aerosols are focused and released to the target at high pressure and high speed (see **Figure 19 (5)**). The target is placed on the computer-controlled translation stage (see **Figure 19 (6)**).

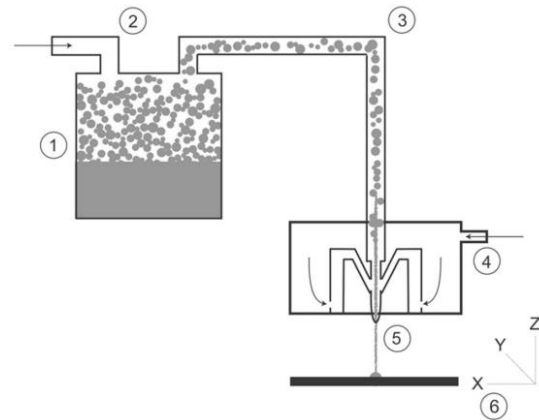


Figure 19. Aerosol jet printing process steps [112].

The main disadvantage of this method is its relatively high cost and the complexity of printing on three-dimensional surfaces [112, 113].

1.11.3. Inkjet printing

This method is similar to the aerosol droplet printing technique, where ink with silver nanoparticles is most commonly used instead of aerosols. A specialized metalized solution is introduced into an enclosed ceramic vessel containing a small opening on one side for injections and a piezoelectric or thermal barrier on the opposite side [114].

The volume of the vessel is manipulated by inducing an electric current or modifying the temperature of the piezoelectric or thermal barrier (see **Figure 20**). The generated pressure expels a droplet onto the specimen through a micro-aperture (needle).

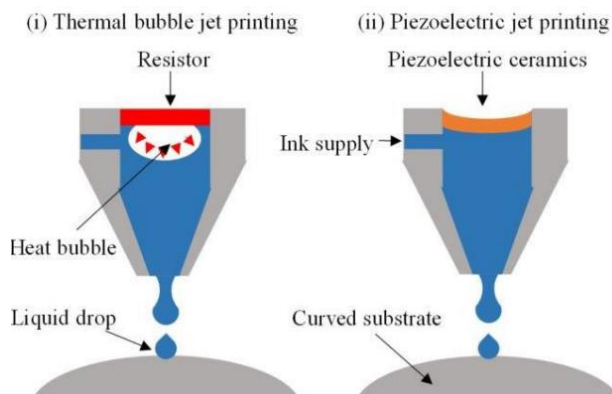


Figure 20. Inkjet printing process steps [115].

The principal drawback of this approach, as with the prior aerosol printing method, is its costliness due to the use of relatively pricey equipment. Moreover, printing on three-dimensional surfaces using this method is challenging [115, 116].

1.11.4. Pressing

The principle of this method is that a metal wire conductor is directly pressed onto the surface of the plastic. This is done using a special heated press, whose working surface contains the desired conductor pattern. A foil made of copper or another metal is placed between the heated press and the plastic part on which the wire conductor is intended to be formed. Then, the press is applied to press the metal foil onto the plastic surface, causing the foil to heat up, and the wire conductor is formed on the plastic part. Unnecessary areas of the pressed metal foil can be mechanically removed by crushing them. This method is primarily used to produce larger parts where high precision is not required. The minimum width of structures made using this method is 1000 μm [117].

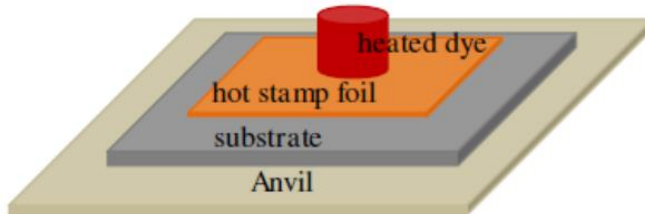


Figure 21. Copper pressing process scheme [117].

1.11.5. Brushing a metal paint

Brushing metal paint on plastic is commonly used to apply a metallic coating to plastic surfaces. In this process, a specialized metal paint or paint containing metallic pigments is applied directly onto the plastic surface using a brush or similar applicator. The metal paint adheres to the plastic substrate and dries to create a thin layer of metallic finish.

However, it's essential to note that this method may not offer the same durability and performance as other metal deposition techniques like electroplating or laser direct structuring. However, it still serves as a straightforward and cost-effective way to achieve a metallic look on plastic surfaces [118-120].

1.11.6. Physical vapor deposition on polymers

Thin metal layers could be deposited on polymers using the physical vapor deposition (PVD) method. B. Wang group has shown this by plating liquid crystal polymers (LCP) for use in molded interconnect device (MID) manufacturing [121]. They deposited a thin chromium layer with a thickness of less than 100 nm and later deposited a copper layer with a thickness of 3 μm . The deposition rates of copper and chromium were approximately 10 $\mu\text{m}/\text{h}$ and 3 $\mu\text{m}/\text{h}$, respectively. The deposition of chromium and copper layer on LCP only slightly increased the roughness of the surface. Strong adhesion between the deposited metal layer and polymers was also reported.

Using this method, the thin and uniform metal layer with strong adhesion to the polymer base could be deposited on polymers. However, it is a slow and very expensive process. Also, if the layer cannot be deposited selectively, it is used to deposit the whole area [122, 123].

1.11.7. Chemical vapor deposition on polymers

Chemical Vapor Deposition (CVD) methods involve the deposition of metal particles onto a product's surface through the chemical reduction or gas decomposition of a chemical precursor. The chemical precursor refers to a compound that occurs or forms in the initial stage of the reaction and transforms into another substance during the process. These reactions can be initiated thermally, through irradiation, or plasma treatment [124]. The temperature and gas pressure during the process influence the rate of metal layer deposition.

However, the chemical vapor deposition on polymer materials is limited due to the high temperatures required, often reaching as high as 1000°C, to initiate and sustain the chemical reactions [124, 125]. CVD methods are also very expensive and require a lot of research on precursors.

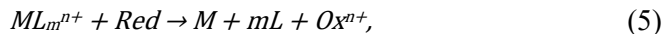
1.12. Comparison between electroless plating and electroplating

1.12.1. Electroless plating

Electroless plating stands as the most common method for plating plastic surfaces, without the need for external electric source assistance during the process (see the principal scheme of electroless plating in **Figure 22**). The electroless deposition process consists of a few steps. In this initial step, the substrate's surface is washed in an ultrasonic bath to eliminate contaminants

that could impact nanoparticle size and lead to suboptimal plating. This process determines both the porosity of the deposited elemental metal and the excellent adhesion of the metal coating. Then, the substrate is immersed in the electroless plating bath solution, where the plating process begins. A metal cation is transformed into elemental metal using a potent reducing agent. Chemical reactions are triggered at the activated surface, causing the metal ions to migrate to the plastic substrate and form a thin layer of metallic film, effectively achieving plating without electrical input [126-128].

Electroless deposition bath solution contains deposition metal ions source (Mn^+), supplied through metal salts (e.g., Cu^{2+} from $CuSO_4$, Ni^{2+} from $NiCl_2$), reducing agent (Red) such as formaldehyde (CH_2O) for Cu^{2+} or sodium (NaH_2PO_2) for Ni^{2+} which donates electrons to the metal cation, facilitating its reduction, ligand (L) (like tartrate, EDTA or acetate) which decrease the concentration of free metal ions, ensuring stable plating conditions and different additives for solution stabilization, buffering, acceleration and so on. The general metal ion reduction process could be expressed by the equation:



The main advantage of electroless deposition is that metal can be plated on any material, not only conductive materials. Also, it does not require an external current source, so it is cheaper to compare with electroplating. The deposition could be performed on complex-shaped three-dimensional parts. Also, the coating layers are uniform. Despite its numerous advantages, this method has its disadvantages. The main disadvantage is that it is a slower process than other deposition techniques. To deposit a coating, sometimes it could take a few days. Also, deposited coating thickness is limited. Due to the nature of the process, electroless deposition is suitable only for thin coatings. Besides, the method is suitable for pure metals; however, depositing metal alloys is very complex. Another problem is the sensitivity of the deposition solution. Small variations in temperature or pH can lead to inconsistent results and the need for frequent bath monitoring and maintenance. Electroless deposition produces a lot of chemical waste in the form of spent plating baths and rinse waters containing potentially hazardous materials.

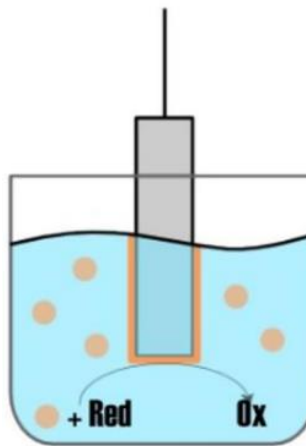


Figure 22. Electroless deposition principal scheme [128].

1.12.2. Electroplating

Electroplating relies on an external current supply. The electroplating operates on a fundamental principle using an electrolytic cell comprising an anode (the metal to be plated) and a cathode (the object to be plated). These two components are submerged within an electrolyte solution (see the principal scheme of electroplating in **Figure 23**).

The electroplating occurs when a direct electric current is applied to the electrolyte solution. An electrolytic solution provides a medium for the movement of ions between the anode and cathode. The main component is a salt derived from the metal intended for plating (i.e. copper sulfate CuSO_4 or nickel sulfate NiSO_4). This salt deposits a metal ion source; it dissociates into metal ions and contributes to the deposits of the object to be plated. Also, the solution often contains acid or base to control the pH level and various additives to modify the properties of the plated layer. Adjustment of pH level could influence the plating rate, whereas additives could affect the deposited layer's hardness, adhesion, and brightness.

Electric current causes metal ions to dissolve from the anode into the electrolyte, and these ions then migrate towards the cathode, where they undergo reduction and are subsequently laid down as a thin and tightly bonded metal coating. The main electroplating equation describes the fundamental process of depositing a metal onto a substrate through electroplating, which can be generalized as follows:



where M^{n+} represents a metal cation with a positive charge, the symbol n^- denotes n electrons required for the reduction of the metal cation, and M signifies the metal undergoing deposition onto the substrate. For example, in copper electroplating (used to create copper layers on various substrates), the main electroplating equation is:



Different variables, such as current density, voltage, plating duration, and bath temperature, could be adjusted for the preferred plating thickness, quality, and visual characteristics.

Finally, after achieving the desired coating thickness, the coated object is removed from the electrolyte bath, undergoes rinsing, and may receive additional treatments like polishing or sealing to enhance its final look and performance [129-133].

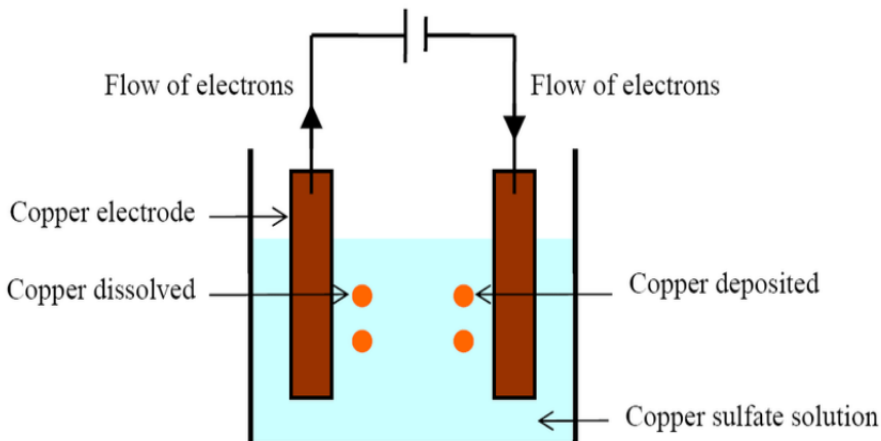


Figure 23. The electroplating scheme is shown [133].

Gold, silver, chromium, nickel, copper, and zinc are the most common materials for electroplating. The main advantage of the electroplating process is that it is much faster than the electroless plating process. To plate the surface, it could take from a few minutes to a few hours, whereas electroless plating could take a few days. Also, the deposited metal layer could be thinner than by electroless plating. However, only conductive materials can be plated by electroplating. Usually, electroplating is used to increase metal thickness when the seed layer is made by other methods.

The comparison of electroless and electroplating advantages and disadvantages is given in **Table 2**:

Table 2. Comparison between electroless plating and electroplating.

	Electroless plating	Electroplating
Plating speed	Slow	Fast
Plating thickness	Thin coatings	Medium thickness coatings
Plating uniformity	Very uniform coatings	Medium uniformity coatings
Materials to be plated	All materials	Only conductive materials
Controlling the process	Difficult	Not difficult

1.13. Electroplating on polymers

1.13.1. Electroplating on conductive polymers

A. Islam group described a method of electroplating polymers. In the proposed method, there were used conductive plastic deposits. This type of plastic is artificially made conductive by doping it with conductive fillers, such as carbon black, graphite, carbon nanotubes, metallic fibers, etc. In their experiments, they used a material Schulteatec TinCo 50 from Schulman Inc. Akron, USA, which consisted of 15 wt.% (56 vol.%) Polyamide 6 (PA6), 52 wt.% of fine copper fibers (average length 0.65 mm, diameter 35 μm) and 33 wt.% of a low-melting Tin/Zinc alloy (199 $^{\circ}\text{C}$).

At the first attempt of electroplating, the specimen was connected to the cathode terminal, and the anode was a pure copper electrode. The specimen was immersed in a plating bath consisting of sulfuric acid and copper sulphate. A current density of 8 A/dm^2 was set, and the plating time was 11 minutes. About 12 % of the area was covered with copper, and the rest remained uncovered.

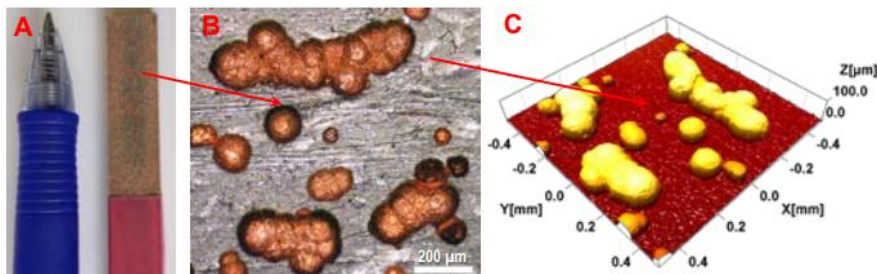


Figure 24. (A) and (B) a plastic part after electroplating, and (C) a 3D image of the electroplated surface [134].

At the second attempt, different surface treatment techniques, such as milling, sandpaper grinding, and wet abrasive blasting, were performed on the surface of specimens before electroplating. This led to an increase in copper-plated surface area; however, the 100 % plated surface coverage was not achieved (see **Figure 25**).

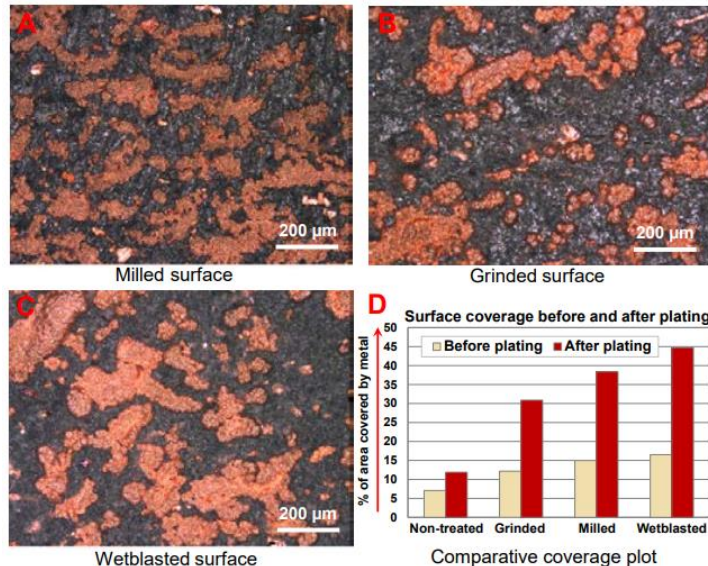


Figure 25. Sample coverage by metal after electroplating on (A) a milled surface, (B) a ground surface (C) a wet-blasted surface, and (D) a comparative copper deposition coverage plot [134].

The highest electrical conductivity was achieved on the electroplated surface, wet blasted before plating. About 70 % of the increase in conductivity was observed after plating with copper, which was 0.85×10^6 S/m. Higher conductivity was observed after plating with nickel, which was 1.21×10^6 S/m [134].

1.13.2. Electroplating process on ABS plastic

M. Bazzaoui's group showed how nickel and copper were successfully deposited on acrylonitrile butadiene styrene (ABS) plastic by electroplating. Their process contained three steps. Initially, they deposited a polypyrrole (Ppy) layer onto the ABS surface to make nonconductive plastic suitable for electroplating. Polypyrrole (Ppy) is an organic conducting polymer created through the oxidative polymerization of pyrrole monomers. Therefore, the initial step involved immersing ABS samples in a pyrrole solution. The Ppy

coating was achieved after two hours with continuous magnetic stirring. Subsequently, the Ppy-coated ABS samples underwent rinsing with distilled water and methanol, followed by copper deposition in an electroplating bath. The final step in their process involved depositing nickel onto the copper coating, which was also carried out in the electroplating bath [135].

1.13.3. Selective electroplating of 3D printed parts

Selective electroplating of 3D printed parts is a post-processing technique that enables the precise application of a thin metal coating onto specific areas of a 3D printed object. This process allows for targeted plating on desired regions of the part, providing enhanced properties such as conductivity, corrosion resistance, or improved aesthetics. The process consists of a few steps. The initial step involves creating the object using 3D printing technology. Those layers, which need to be deposited by copper, are printed from conductive polymers, and the rest are from non-conductive polymers. The later printed part is immersed into the electroplating bath, where an electric current is applied, and copper selectively deposits the printed part layers that were printed from conductive polymer [136].

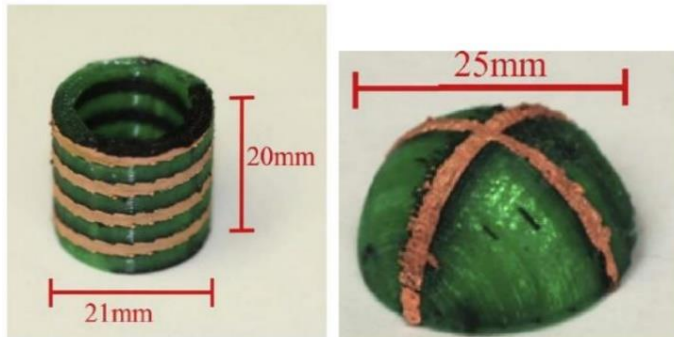


Figure 26. An example of a plastic component with selectively deposited copper is created through the printing of distinct plastic layers [136].

2. EXPERIMENTAL SETUP AND METHODS

2.1. Materials

Polyimide Kapton® HN type films from DuPont with a thickness ranging from 25.4 μm to 127 μm were used in our experiments. Successful applications of this type of polyimide film have been demonstrated at temperatures ranging from -4 K to 130 K. **Table 3** represents the main properties of polyimide film:

Table 3. Main characteristics of Kapton® HN film [137].

Material properties	Typical value
Density, g/cm ³	1.42
Refractive index	1.7
Thermal coefficient of linear expansion, ppm/°C	20
Thermal conductivity, W/mK	0.12
Dielectric constant	3.5
Electrical resistivity, Ωm	10^{17}

Transmission through the sample for different wavelengths was measured experimentally. For a 10.6 μm wavelength, the transmission is 5 %; for 1064 nm – 84 %; for 532 nm, the transmission - 16 %; for 355 nm – 2 %.

Bio-degradable polymer ARBOFORM® F45 from TECNARO GmbH was also used in the experiment. ARBOFORM® is made from 100 % renewable raw materials and is biodegradable. It is composed of the two most abundant natural materials: approximately 30 % lignin and 60 % cellulose. This material shares a similar composition, appearance, and properties with wood, yet it can undergo melting upon heating and be molded like a thermoplastic. The thickness of the biopolymer plates was 1 mm. The main characteristics are given in **Table 4**.

Table 4. Main characteristics of ARBOFORM® F45 [138].

Material properties	Typical value
Density, g/cm ³	1.31
Thermal conductivity, W/mK	0.384
Surface resistivity, Ω	$5 \cdot 10^9$

All the samples were cleaned with ethanol (Sigma Aldrich) before the experiments.

2.2. Laser treatment

Three different laser sources were used in the experiment.

- A nanosecond solid-state laser Baltic HP (Ekspla, Vilnius, Lithuania) operating at the fundamental wavelength of 1064 nm. The pulse duration of this laser was 10 ns, and the pulse repetition rate was tuned from 10 kHz to 100 kHz. The maximum pulse energy of 115 μ J was used.
- A solid-state picosecond laser Atlantic (Ekspla, Vilnius, Lithuania), which generated 355 nm, 532 nm, and 1064 nm wavelengths. The pulse duration was 10 picoseconds, the pulse repetition rate was tunable from 100 kHz to 500 kHz, and the average laser power was up to 8.5 W at the 1064 nm wavelength.
- A pulsed CO₂ Diamond E-150 (Coherent, Inc., Santa Clara, CA, USA) laser generating up to 150 W of average power at 10.6 μ m wavelength. The repetition rate was tunable from 1 kHz to 100 kHz.

The SCAnge, HurrySCAN and SCAncube galvoscanners (Scanlab, Puchheim, Germany) were used for laser beam positioning. Four different f-theta objectives, with focal lengths of 100 mm (for 532 nm), 160 mm (for 1064 nm), 174 mm (for 355 nm), and 250 mm (for 10.6 μ m), were used for laser beam focusing. Beam profile measurements were performed using a CCD camera (Gentec, Markham, ON, Canada).

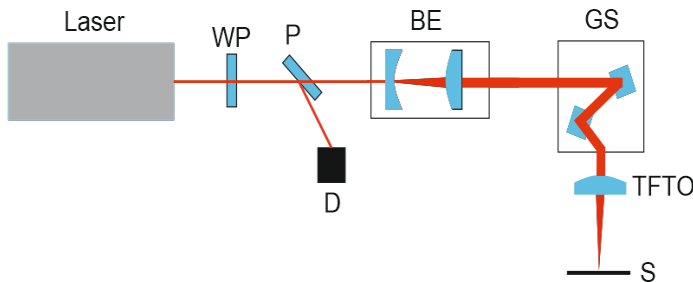


Figure 27. Experimental setup for laser patterning process. WP – half-wavelength wave plate, P – polarizer, D – beam dump, BE – beam expander, GS – galvoscanner, TFTO – telecentric f-theta objective, S – sample.

Samples were processed at the focal plane with a highly focused beam and out of a focal plane with a defocused laser beam (see **Figure 28 (a)**). The treatment out of focus leads to an enlargement of beam diameter on the sample surface. This allows for controlling laser fluence, laser spot size, and pulse

overlap on the Polyimide surface. This way, suitable exposure time and surface temperature could be preserved to facilitate graphene formation. At the initial stage of experiments, the sample was placed at a 45° angle, and the correct distance to the focal plane for graphene formation could be found depending on laser and material parameters (see **Figure 28 (b)**).

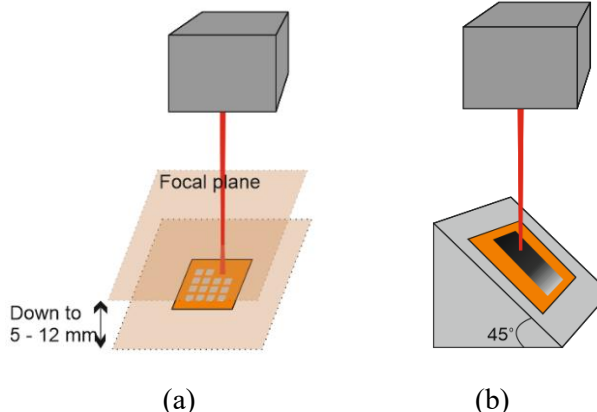


Figure 28. (a) Setup for laser treatment out of focus. (b) Polyimide sample, placed at a 45° angle and laser treated. In this way, various areas of the sample are treated at various distances to the focal plane, and a correct distance to the focal plane can be found for high-quality LIG formation.

The optimal processing parameters, like scanning speed or repetition rate, were found during the testing treatments and kept constant in the later experiments. The matrixes of laser-treated areas were used in a search for optimal parameters. The principle of this method is that the matrix of small squares (5 x 5 mm²) was treated on the sample by changing only the scanning speed value when processing squares in a row and changing the laser pulse energy value when fabricating the next square in a column. Multiple matrixes of squares were treated using different pulse repetition rates. Further, sheet resistances of the laser-treated surface areas were measured. A combination of optimal processing parameters was selected according to treatments, after which surface sheet resistances tended to decrease.

The laser fluence (in J/cm²) was calculated by dividing the pulse energy E by the area of the beam spot S .

$$F = \frac{E}{S}, \quad (8)$$

The irradiation dose, which indicates the amount of energy delivered per square centimeter of the target area, taking into account spot overlap during

the beam scanning, was determined by multiplying the laser fluence by the number of laser pulses per beam spot area:

$$\text{Irradiation dose} = N \cdot F \quad (9)$$

where N indicates the number of pulses per beam spot area. For example, if the beam diameter on the sample surface is 50 μm , the scanning speed is 100 mm/s and the pulse repetition rate is 100 kHz, so it means that per time interval of 1 s, there will be 100000 pulses in 100 mm distance. In 100 mm without overlapping fits 2000 pulses of 50 μm diameter, so it means $N=100000/2000=50$ pulses per spot area.

The irradiation dose (in J/cm^2) parameter was chosen in our experiment because it relates together the scanning speed, pulse repetition rate, and laser fluence. The parameter is widely used in various laser processing applications [139, 18].

2.3. Electroplating

Metal deposition was performed using electroplating. A laser-treated Kapton PI film area with a size of 10 x 20 mm^2 was connected to the cathode terminal for metal deposition, and a deposition metal sheet (copper, nickel, tin, silver, cobalt, or zinc) was connected to the anode terminal. The metal deposition on laser-treated Kapton PI films was performed using electroplating in an acidic solution bath. The principal setup scheme is shown in **Figure 29**.

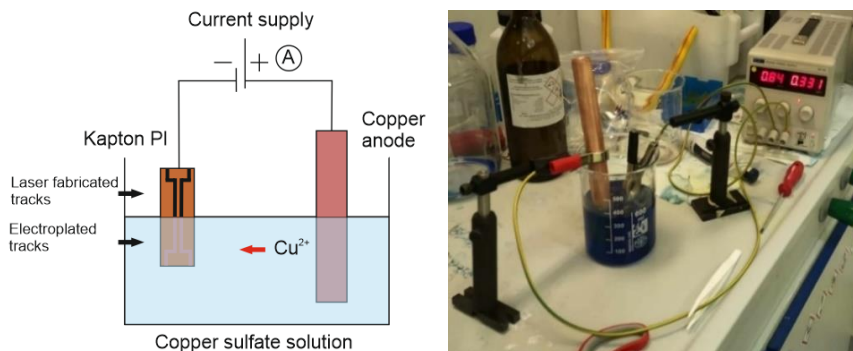


Figure 29. Electroplating scheme and setup.

Plating time ranged from 10 min to 60 min. Electroplating was performed in the electrolytic solutions, whose chemical compositions are given in **Table 5**. The current density of plating was varied from 4 to 20 mA/cm^2 , and the plating speed was 0.2 to 0.5 $\mu\text{m}/\text{min}$. To get a more uniform coating layer, a magnetic stirring of 550 rpm was used in the bath during plating.

Table 5. Electroplating parameters for metal plating on LIG samples.

Metal	Solution	Current density, mA/cm ²	Plating speed, µm/min
Cu	H ₂ SO ₄ 50 g/l, CuSO ₄ ·H ₂ O 200 g/l	20	0.44
Ni	NiSO ₄ ·7H ₂ O 250 g/l, NiCl ₂ ·6H ₂ O 45 g/l, H ₃ BO ₃ 38 g/l	20	0.41
Sn	SnSO ₄ 40 g/l, C ₆ H ₅ Na ₃ O ₇ ·2H ₂ O 120g/l, hydroquinone 1g/l	10	0.51
Ag	Commercial cyanide bath	4	0.256
Co	CoSO ₄ ·7H ₂ O 300 g/l, H ₃ BO ₃ 38 g/l, NaCl 20 g/l	20	0.41
Zn	Commercial chloride bath	30	0.86

2.4. Sheet resistance measurement

Sheet resistance, also referred to as surface resistance or surface resistivity, serves as a prevalent electrical characteristic for characterizing thin films composed of conducting and semiconducting materials. This parameter describes the lateral resistance across a thin square of material, specifically the resistance between opposing sides of the square. The measurement unit is Ω/square. This measurement unit is used only for thin films. The resistance of bulk materials is measured in Ω. The notable advantage of the sheet resistance, compared to other resistance measurements, lies in its independence from the size of the square, facilitating straightforward comparisons between diverse samples.

The sheet resistance measurements of laser-treated areas were performed using the four-probe method. The principle of this method is that four probes are aligned in a row, with 1 mm between adjusted probes. While the current passes through external probes, the inner probes are used to measure the voltage. These values allowed us to calculate the surface resistance. Sheet resistance measurements were performed using the source meter (Keithley 2602A, Tektronix, USA) with the measurement software (TSP® Express, Keithley, USA).

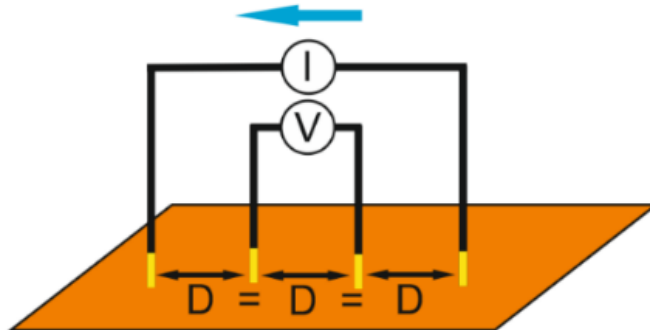


Figure 30. Sheet resistance measurement setup.

2.5. Adhesion measurements

Adhesion measurements were performed using the peel test technique. In this method, scotch tape (Tesa, Norderstedt, Germany) was attached to the surface of the formed graphene layer and then peeled off. The laser-formed graphene layer under investigation must withstand the peel force applied during the peel test. If the graphene layer remains on the polyimide surface after the test, it is considered to have passed the peel test; if not, it is considered to have failed.

2.6. Surface morphology analysis

Microscopic observation of the treated sample surface was done using an optical microscope (Olympus BX52, Olympus, Tokyo, Japan) with a CCD camera. Objectives with magnifications ranging from 5x to 50x were used to image samples in bright and dark field illumination modes.

A scanning electron microscope (JSM-6490LV, JEOL Ltd., Tokyo, Japan) was used for surface analysis. Before SEM analysis, samples were gold-coated using a magnetron sputter coater (Q150T ES, Quorum Technologies Ltd., Laughton, UK) to avoid charging the polymer surface during SEM investigations.

In addition, surface roughness measurements were performed using Sensofar S Neox optical profilometer.

The coverage by a metal of graphene was evaluated using “Image color summarizer” software. The black-colored pixels, which correspond to the non-deposited surface area, were counted.

2.7. Raman spectroscopy

Raman spectra measurements were performed with the Raman spectrometer/microscope in Via (Renishaw, UK) equipped with the thermoelectrically cooled (-70°C) CCD detector. Spectra were excited with the 532 nm wavelength laser and dispersed by 1800 grooves/mm grating. Raman spectra were taken using a 50x/0.75 NA objective lens.

3. RESULTS AND DISCUSSION

The research can be divided into three parts. The initial part involves determining the optimal laser treatment parameters for generating a high-conductivity graphene layer that can be effectively used in electro-deposition processes with diverse metals. A wide array of laser parameters and diverse treatment methodologies were used in the experiment. To measure conductivity, we have selected the commonly used sheet resistance measurement unit. Lower sheet resistance values correspond to higher levels of conductivity.

The second part focused on characterizing laser-formed graphene layers. The primary method of characterization involved obtaining Raman spectra from samples treated at the focal plane and with a defocused laser beam. Additionally, heat conduction modeling was conducted on Polyimide sample surfaces during laser irradiation to determine the optimal conditions for LIG formation.

The third part of the research was focused on the electroplating of the laser-formed conductive graphene layer. The primary objective in this phase was to identify the appropriate parameters that ensure the efficiency of the deposition process.

The results of experiments are published in scientific publications [A1] and [A2] and presented at conferences [C1-C5]

3.1. Laser treatment of samples

In this part of the experiment, laser treatment was performed on polyimide and bio-degradable polymer samples with focused and defocused laser beam, nanosecond, and picosecond laser. Various laser sources were used, ranging from UV radiation 355 nm wavelength, VIS 532 nm to near-IR 1064 nm and mid-IR 10.6 μ m wavelengths. Samples were treated in the room atmosphere and in a nitrogen atmosphere.

Also, in this section polyimide sample heat conduction modeling after laser irradiation was performed.

3.1.1. Polyimide treatment with picosecond and nanosecond lasers at the focal plane

In the initial part of the experiment, Kapton PI films were placed at the focal plane of the laser beam and treated with the nanosecond Baltic and picosecond Atlantic lasers at 1064 nm wavelength. Rectangles with edge lengths of

10 mm and 20 mm were treated in the scanning direction along the minor edge. The treated area was obtained by treating with partly overlapping laser tracks (hatch = 30 μm and laser spot diameter at the focal plane – 52 μm). The pulse repetition rate was 100 kHz, and the scanning speed was 100 mm/s. Irradiation doses were increased by increasing the laser power from 1.25 to 6 watts. All other parameters were kept constant.

Changes in the sheet resistance appeared when the irradiation doses were higher than 20.41 J/cm^2 after treatment with ns laser and 17.75 J/cm^2 after treatment with ps laser. The sheet resistance of the laser-treated surface started to decrease at those values, and soot began to appear on the surface of the samples (see **Figure 31**). An increase in the irradiation dose led to the formation of a thicker soot layer with lower sheet resistance.

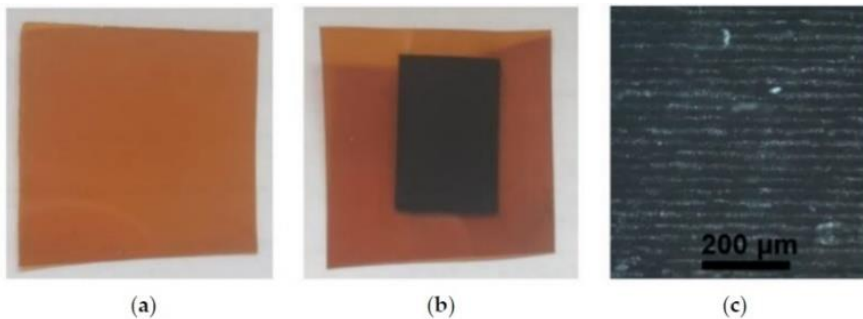


Figure 31. Polymer Kapton PI film: (a) before laser treatment, (b) after laser treatment, and (c) magnified ($\times 10$) view of the laser-treated area.

The lowest achieved sheet resistance was 354 Ω/sq . during the nanosecond laser irradiation with 184 J/cm^2 , and one-order lower values were obtained after the picosecond laser irradiation. At this regime, the lowest sheet resistance was 30 Ω/sq . when the irradiation dose was 130 J/cm^2 (see **Figure 32**).

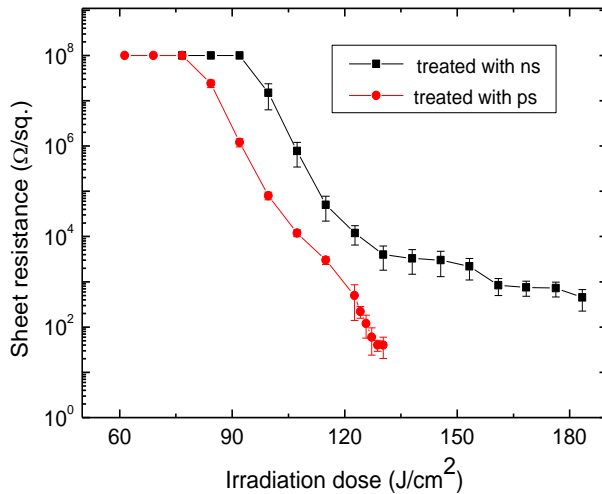


Figure 32. Dependence of the polymer Kapton® sheet resistance on the irradiation dose after treating at the focal plane with nanosecond (black line), and picosecond laser pulses (red line).

Irradiation with higher doses damaged the sample. The treated surface became cracked and improper for further use. Thin PI samples were deformed using the ns-regime due to excessive heating at irradiation doses higher than 128 J/cm^2 . Also, the treatment repeatability was better using the ps-laser irradiation. Therefore, the experiments were later continued only using the ps-regime.

3.1.2. Irradiation at the non-focal plane with 1064 nm

The second processing method of Kapton PI films was performed with the picosecond laser when the sample was placed below the focal plane and treated with a defocused laser beam. Different beam spot diameters on the sample surface were adjusted by changing the sample position relative to the laser beam focal plane. The specimen was moved below the focal plane as much as 12 mm in 0.25 mm steps, and that caused the spot size to change from $52 \mu\text{m}$ at the focal plane to $754 \mu\text{m}$ at 12 mm below the focal plane (see **Figure 33**). The use of an out-of-focus treatment enables the control of laser fluence, laser spot size, and pulse overlap on the Polyimide surface. All other process parameters, including laser power, repetition rate, or scanning speed, were kept constant during this experiment. Only the sample position relative to the focal plane was changed.

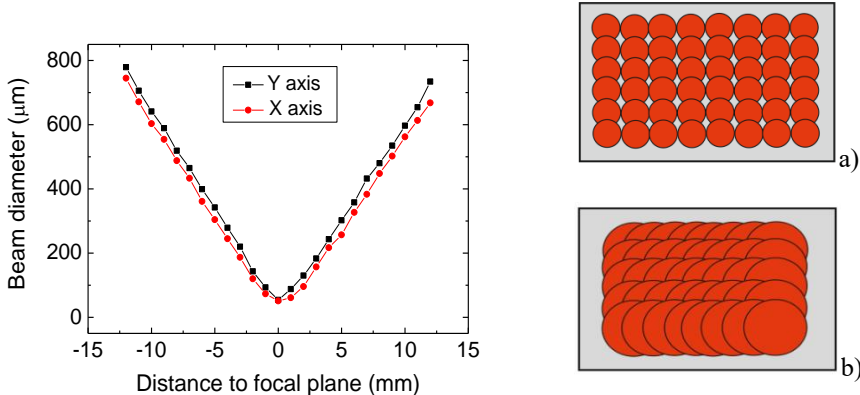


Figure 33. The beam diameter out of focus. At the focal plane, almost non-overlapping spots were obtained (a). With increasing defocusing, overlap increased due to a significantly larger beam diameter on the sample surface (b).

The sample was initially placed at the focal plane. Later, the sample was moved down below the focal plane by 3 mm in 0.25 mm steps. The irradiation dose at this distance was from 130 J/cm^2 (at the focal plane) to 17.75 J/cm^2 (3 mm below the focal plane). Soot formed on the sample surface in this treatment range (see **Figure 34**). A strong dependence of sheet resistance and applied irradiation dose was observed after treatment in this defocus range. A thicker layer of soot formed when treated with a high irradiation dose, and, accordingly, surface sheet resistance was lower. Sheet resistance was as low as $30 \Omega/\text{sq}$. when treated at the focal plane with 130 J/cm^2 irradiation dose and $20 \text{ M}\Omega/\text{sq}$. when treated at 3 mm below the focal plane with a 17.75 J/cm^2 irradiation dose.

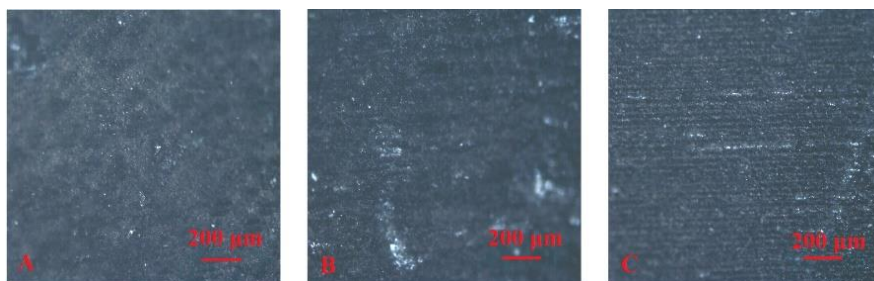


Figure 34. The samples, treated at the focal plane (A), 1.5 mm below the focal plane (B), and 3 mm below the focal plane (C). Black-colored, carbon-like structures appeared on the surface of the sample. At the focal plane treated sample surface was covered with soot. Lowering down the sample, a thinner layer of soot was formed.

Moving the sample down beyond 3 mm, the treated area started to appear greyish. In the range from 3.25 mm to 4.75 mm below the focal plane, the laser irradiation dose in this distance was from 15.5 J/cm^2 (3.25 mm below the focal plane) to 11.4 J/cm^2 (4.75 mm below the focal plane). After treatment with these irradiation doses, part of the treated area was covered by grey structures (see **Figure 35**). Those structures were with a sheet resistance of 70-80 Ω/sq . However, adhesion between the formed cluster and the sample surface was weak. As a result, part of the structures dropped off when the sample was bent over a few times.

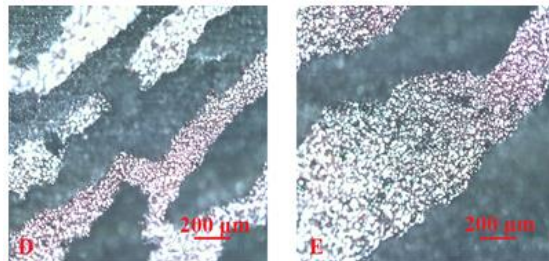


Figure 35. The samples treated 4 mm below the focal plane (D) and 5 mm below the focal plane (E). Clusters of grey-colored structures appeared in this regime.

Further moving the sample out of focus led to the formation of smooth grey graphite-like structures, as we suggest laser-induced graphene (LIG) (see **Figure 36**). Those structures were formed when treating in the distance range from 5 mm to 12 mm below the focal plane, where irradiation dose in this range varied from 10.76 J/cm^2 (5 mm below the focal plane) to 4.42 J/cm^2 (12 mm below the focal plane). The sheet resistance was constant on the whole treated area in this defocus range, and it was $8 \Omega/\text{sq}$.

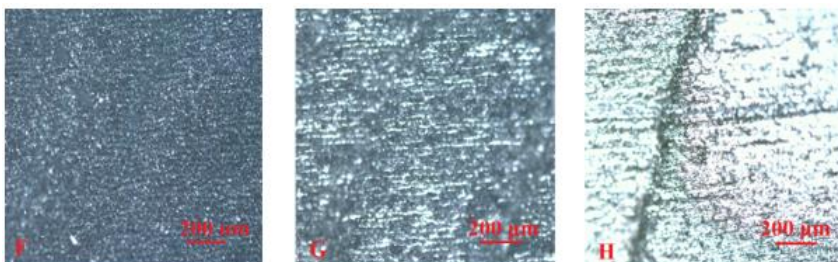


Figure 36. The samples treated 6 mm below the focal plane (F), 7 mm below the focal plane (G), and 8 mm below the focal plane (H). A grey-colored graphene structure with a smooth and low-sheet-resistance surface was formed in that defocus position.

Moving down the sample below 12 mm, the PI surface became unaffected after the laser irradiation. This was because energy density was too low to affect the sample. The treatments were performed when the samples were lifted above the focal plane to 12 mm in height as well. The results were the same.

Three different modifications of the PI surface after irradiation with the laser could be distinguished after treatment at various distances from the focal plane with 1064 nm (**Figure 37**). Soot was formed on the surface of the sample when treated in the range around the focal plane (0 mm to 3 mm below the focal plane; the irradiation dose was from 130 J/cm^2 to 17.75 J/cm^2). Clusters of grey-color structures formed when the polyimide sample was placed from 3.25 mm to 4.75 mm below the focal plane (irradiation dose 15.5 J/cm^2 - 11.4 J/cm^2). Finally, laser-induced graphene occurred when the sample was placed from 5 mm to 12 mm below the focal plane (irradiation dose 10.76 J/cm^2 - 4.42 J/cm^2).

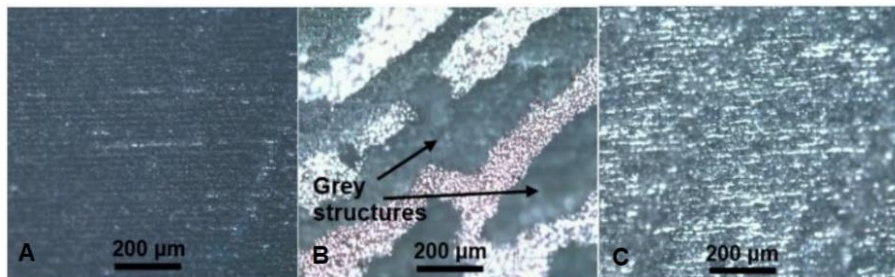


Figure 37. Microscope images of the sample surface: (A) treated at the focal plane. Soot appeared on the surface of the sample; (B) treated 4 mm below the focal plane, where clusters of grey-colored structures formed; (C) treated 7 mm below the focal plane. LIG structures, with smooth surfaces and low sheet resistance, were formed in this regime.

The sheet resistance of PI surface after treatment with a 1064 nm laser in a wide range of irradiation doses is presented in **Figure 38**. Different types of PI surface modification could be explained because of differences in surface temperature distribution when irradiating at the focal plane and out of focus. Treating at the focal plane, there was low laser pulse overlap, which was causing the sudden temperature increases/decreases on the polyimide surface. On the other hand, when treatment was performed out of focus, the laser pulse overlap was much higher. Therefore, it helped to keep the elevated temperature on the Polyimide surface for a longer time during scanning with a laser beam.

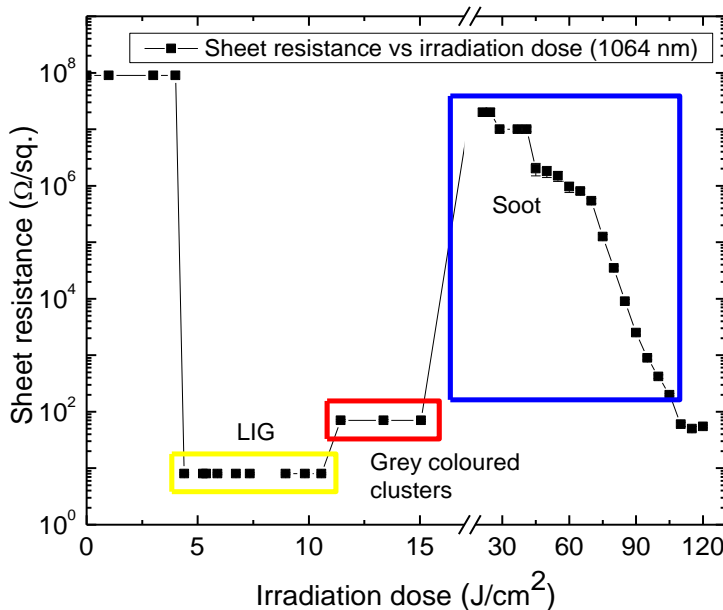


Figure 38. The sheet resistance of the laser-treated polyimide surface versus irradiation dose. The irradiation dose was varied only by changing the beam diameter on the sample surface (defocusing). Three different polyimide surface modification regimes were distinguished. Depending on the applied irradiation dose, soot, laser-induced graphene, or transitional state were found on the PI surface.

The main challenge to form graphene from PI was to keep the required beam spot overlap and this way to keep for a specific time duration the surface temperature above a certain value, which is high enough for the decomposition of imide molecules into hexagonal carbon rings, forming graphene [140, 141]. The occurrence of LIG structures on the PI sample strongly depends on irradiation time and surface temperature. Irradiation time could be controlled by changing repetition rate, scanning speed, and beam diameter, while the surface temperature is determined by laser fluence. We found that irradiation dose (fluence x number of pulses) quite well represents experimental conditions for LIG formation.

LIG was formed on the Polyimide sample when treated with an irradiation dose of 10.76 J/cm^2 (5 mm below the focal plane) to 4.42 J/cm^2 (12 mm below the focal plane). When treating the PI surface positioned 5 mm below the focal plane, the number of pulses per spot area N was equal to 300, and the laser fluence F was 0.035 J/cm^2 . In the treatment where the sample was positioned 12 mm below the focal plane, the beam enlargement resulted

in an N value of 730 and an F value of 0.006 J/cm^2 . To initiate polyimide decomposition and LIG formation, the laser fluence should be in a particular range to heat the material, and a certain exposure time is required for the decomposition reaction.

In conclusion, to achieve the appropriate exposure time and surface temperature for the PI sample, it should be exposed by 1064 nm wavelength with a fluence ranging from 0.006 J/cm^2 to 0.035 J/cm^2 , with a beam overlap of 300 to 730 pulses per spot area. The pulse per beam spot area N value could be expressed in time. Treating the sample at a 100 kHz pulse repetition rate, each pulse is emitted every 10 μs . For graphene formation on the PI surface, it is required from 300 to 730 pulses per spot area, or, in time scale, the beam spot area must be irradiated from 3 ms to 7.3 ms.

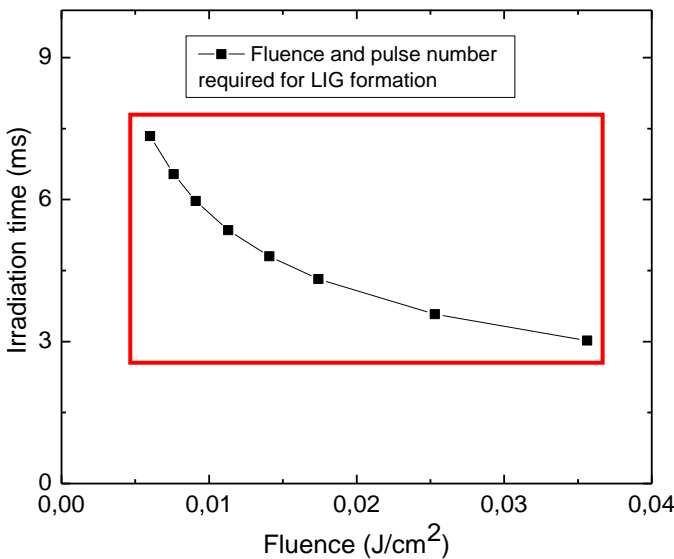


Figure 39. Relation between the pulse number per beam spot area and laser fluence, when LIG was formed on PI surface.

LIG could be formed when treating at the focal plane, however, to get the required pulse overlap, a much lower scanning speed will be needed when treating at the focal plane, and this will significantly slow down the process. Therefore, we chose treatment with a defocused beam in our experiment.

This treatment approach, involving the use of a defocused laser beam, is widely used by other research groups for the purpose of LIG formation [142-144].

3.1.3. Fabricating with 355 nm and 532 nm out of the focal plane

Polyimide samples were treated with the defocused laser beam, using 355 nm and 532 nm. The goal was to understand how each wavelength affects the formation of LIG. The photon energy of an ultraviolet laser is sufficient to directly break the bonds in polyimide, as the C-C bond energy is approximately equal to the photon energy corresponding to the 355 nm wavelength. Alternately, when infrared radiation is used, the photon energy is too low to break the chemical bonds, resulting in heating effects dominating. Using visible wavelength, both effects take part [29, 30, 89, 145-147].

Samples were initially placed at the focal plane of the laser beam and then moved down below the focal plane to 12 mm in 0.25 mm steps and processed with the defocused laser beam. All the parameters were kept constant except the sample distance to the focal plane. A fixed average laser power was used, fixed repetition rate, and scanning speed. Rectangles of size $10 \times 20 \text{ mm}^2$ were treated on the sample surface.

The irradiation doses from 2.1 J/cm^2 to 14.8 J/cm^2 were needed to transform the polyimide surface into LIG treating with a 355 nm wavelength. LIG was found on the sample surface after irradiation from 3.2 J/cm^2 to 14 J/cm^2 with 532 nm (see **Figure 40**). The lowest sheet resistance of processed sample areas, where LIG appeared, was $18 \Omega/\text{sq}$. after treatment with 355 nm and $13 \Omega/\text{sq}$. with 532 nm.

Treatment with a highly focused beam (irradiation dose higher than 26 J/cm^2) led to the formation of a soot layer on the Polyimide sample surface. A ticker soot layer was formed with reduced sheet resistance by reducing the beam diameter. The sheet resistance of the soot layer, formed after the treatment with 26 J/cm^2 irradiation dose, was $20 \text{ M}\Omega/\text{sq}$. and, at the focal plane, was $70 \Omega/\text{sq}$.

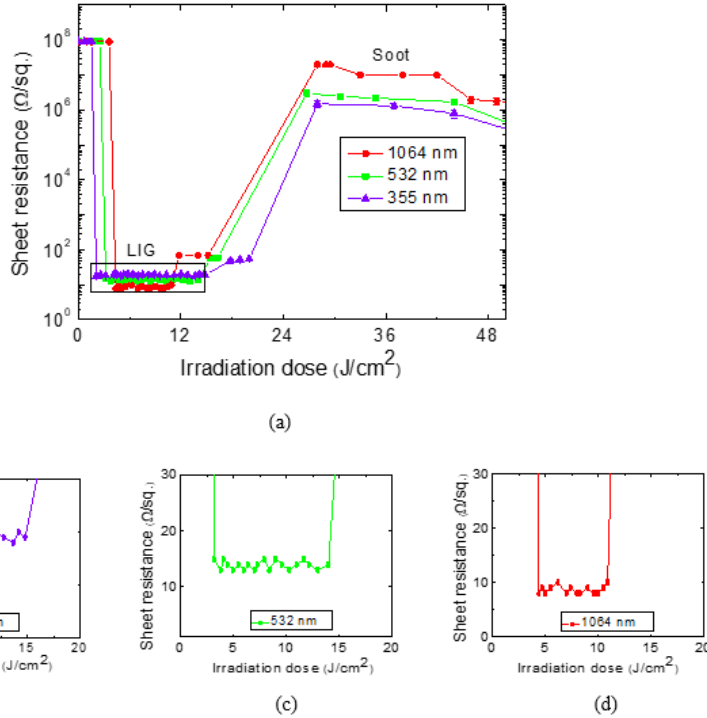


Figure 40. The sheet resistance of the laser-treated surface after irradiation with 355 nm, 532 nm, and 1064 nm wavelengths with irradiation doses up to $50 \text{ J}/\text{cm}^2$ (a). Graphs (b-d) magnified view of sheet resistance dependence on the irradiation dose where LIG was achieved.

The surface morphology of formed graphene layers, treated with $7 \text{ J}/\text{cm}^2$ at 355 nm, 532 nm, and 1064 nm wavelengths, is shown in **Figure 41**. LIG, which was formed after irradiating with 1064 nm wavelength, was partially cracked. No surface cracks were observed on the samples treated with 355 nm and 532 nm radiation. LIG surface formed after irradiation with 355 nm and 532 nm was smooth and well bonded to the polyimide substrate. It did not peel off after bending. This might be caused by different LIG formation mechanisms irradiating with different wavelengths: to form LIG with infrared radiation causes a heating effect and pyrolysis of the sample surface; on the other hand, irradiating with ultraviolet, photon energy is high enough to directly break C-C, C-O, C-N chemical bonds of material, but preserves hexagon benzene rings with C=C bonds [89, 145-147].

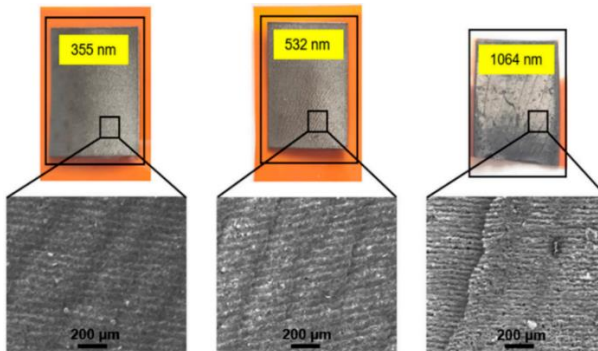


Figure 41. LIG formed on the Kapton PI surface after treatment with 7 J/cm^2 irradiation dose using 355 nm, 532 nm, and 1064 nm wavelength. Surface cracks were found on LIG, formed with 1064 nm.

3.1.4. LIG formation in a nitrogen atmosphere

The laser treatment mechanism of PI in the air can be described as the oxidative reaction between laser-irradiated PI and atmospheric oxygen. Atmospheric oxygen results in high-temperature combustion of the PI structure. In this case, the polyimide surface not only forms graphene but also graphene oxide, which contains defects. In contrast, in treatment under inert atmospheric conditions, the absence of an oxidizing agent leads to the formation of a comparatively stable graphene structure [148-150].

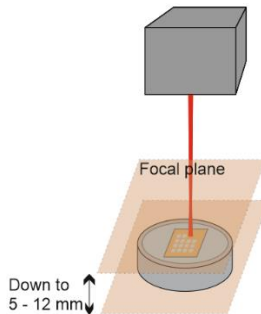


Figure 42. Schematic view of PI treatment in nitrogen chamber.

The polyimide sample was placed in a chamber with nitrogen, and the surface was treated with a defocused laser beam at the 1064 nm wavelength (see **Figure 42**). The chamber was moved down from 0.25 mm to 8 mm below the focal plane. The pulse repetition rate was 100 kHz, and the sample processing speed was 100 mm/s. Surface modification occurred when the irradiation dose was 5 J/cm^2 or higher. **LIG with the lowest in our**

experiments sheet resistance of $5 \Omega/\text{sq}$. was formed on the sample surface when the sample was placed from 7 to 8 mm below the focal plane corresponding to the irradiation dose from $7.3 \text{ J}/\text{cm}^2$ to $7.8 \text{ J}/\text{cm}^2$.

3.1.5. PI treatment with $10.6 \mu\text{m}$ wavelength

In the next part of the experiments, polyimide samples were processed with a CO_2 laser, generating a $10.6 \mu\text{m}$ wavelength. In this case, the energy carried by photons was significantly lower than the energy required to break C-C bonds. As a result, the heating effect had a substantial impact. Samples were processed using 10 W of average power, operating at a 100 kHz pulse repetition rate. The scanning speed was 200 mm/s, the laser beam spot diameter at the focal plane was $400 \mu\text{m}$, and the laser-line overlap hatching was $200 \mu\text{m}$. Samples were treated with a defocused laser beam at different distances when samples were placed down to as low as 42 mm below the focal plane in 3 mm steps. When treating at the focal plane or down to 6 mm below the focal plane, samples were burned through due to too high laser intensity. The lowest sheet resistance was $7 \Omega/\text{sq}$. after treatment when the sample was placed 9 mm below the focal plane with an irradiation dose of $8.6 \text{ J}/\text{cm}^2$ (see **Figure 43**).

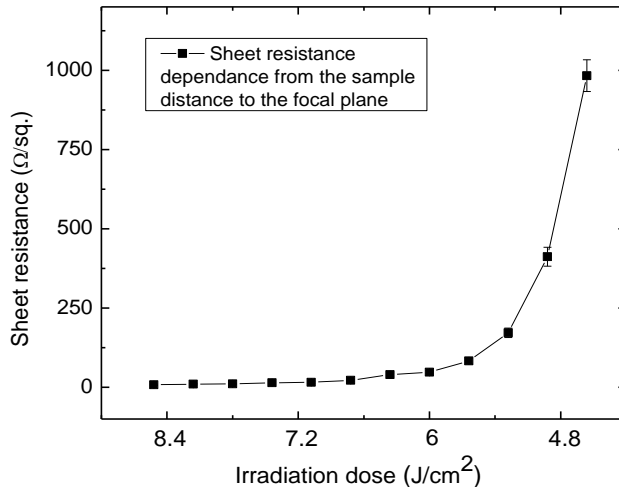


Figure 43. Treated surface sheet resistance dependence on irradiation dose of $10.6 \mu\text{m}$ wavelength.

To conclude, all the treatment parameters required for LIG formation are given in **Table 6**. It was found that optimal laser beam spot overlap for high-

quality LIG formation on the PI surface is 400-500 pulses per beam spot area, with a laser fluence of 0.02 J/cm².

Table 6. The comparison of exposure parameters for LIG formation using laser radiation with 355 nm, 532 nm, 1064 nm and 10.6 μ m wavelengths.

Wavelength, nm	1064	532	355	1064, in the N ₂	10600
Optical PI transmission, %	84	16	2	84	5
Average laser power, W	3.25	0.8	0.8	3.25	10
Pulse repetition rate, kHz	100	100	100	100	100
Pulse duration	10 ps	10 ps	10 ps	10 ps	3 μ s
Scanning speed, mm/s	100	40	40	100	200
Focal spot diameter, μ m	52	24	25	52	400
Min dose for LIG formation, J/cm ²	4.4	3.2	2.1	5	4.2
Max dose for LIG formation, J/cm ²	10.8	14	14.8	12	11.3
Min fluence for LIG formation, J/cm ²	0.006	0.004	0.002	0.006	0.007
Max fluence for LIG formation, J/cm ²	0.035	0.04	0.043	0.031	0.052
Number of pulses per spot area required for LIG formation	300-730	340-940	350-1160	320-750	220-610
Irradiation time, ms	3-7.3	3.4-9.4	3.5-11.6	3.2-7.5	2.2-6.1
Min sheet resistance of LIG, Ω /sq.	8	13	18	5	7
Required number of pulses per spot area for min sheet resistance LIG	430	490	500	440	410
Corresponding irradiation time, ms	4.3	4.9	5	4.4	4.1
Optimal dose for the lowest sheet resistance LIG, J/cm ²	7.34	8.27	8.95	7.34	9.2
Optimal fluence for the lowest sheet resistance LIG, J/cm ²	0.018	0.019	0.021	0.018	0.027

There were also many experiments performed to increase polyimide conductivity by other research groups. For comparison, **Table 7** shows the results of other research groups, treatment of polyimide using a wide variety of different laser sources and laser parameters.

Table 7. Sheet resistance of polyimide samples after treatment with various laser sources.

Laser type	Wavelength	Power/fluence	Pulse duration	Sheet resistance/conductivity	References
CO ₂	10.6 μm	5.4 W	14 μs	25 S/cm	[84]
CO ₂	10.6 μm	6.25 W	CW	5 Ω/sq.	[152]
CO ₂	10.6 μm	11 J/cm ²	10 μs	20 Ω/sq.	[89]
Diode	405 nm	0.161 W	CW	108 Ω/sq.	[153]
Pulsed laser					
Yb:YVO ₄	1064 nm	0.4 W	10 ns	35 Ω/sq.	[18]
Nd:YVO ₄	355 nm	8 J/cm ²	8 ns	160 Ω/sq.	[89]
Excimer	248 nm	0.2 J/cm ²	30 ns	100 Ω/sq.	[154]
Ultrashort pulse laser					
Yb:YVO ₄	1064 nm	0.3 W	10 ps	179 Ω/sq.	[18]
Ti:sapphire	795 nm	0.03 W	300 fs	40 S/cm.	[151]
Ti:sapphire	794 nm	0.04 W	200 fs	15 S/cm	[151]

3.1.6. Biopolymer processing with 1064 nm

In the next part of the experiment, biodegradable polymer was used instead of polyimide for the laser processing. The ARBOFORM bioplastic was treated in two regimes: firstly, it was treated in a room atmosphere with a defocused laser beam. In the other part of the experiment, the bioplastic was treated with a defocused laser beam, but the sample was placed in a nitrogen cuvette. In both cases, samples were treated with the same laser parameters: pulse repetition rate was 100 kHz, scanning speed was 10 mm/s, pulse duration was 10 ps and the wavelength was 1064 nm. The laser power was constant and set to 1.8 W. The treatment of the bioplastic sample, whose thickness was 1 mm, required a much higher irradiation dose than treating thin polyimide films. The scanning speed was reduced from 100 mm/s to 10 mm/s to increase the irradiation dose. The sheet resistance dependence on the irradiation dose is plotted in **Figure 44**.

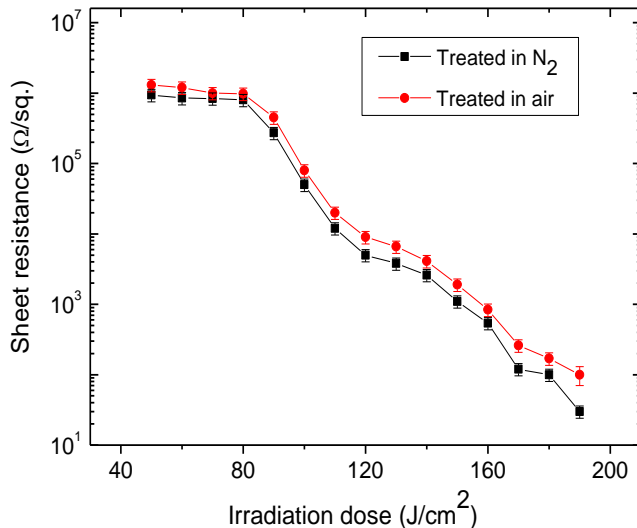


Figure 44. Sheet resistance dependence on irradiation dose of ABROFORM sample treated in nitrogen atmosphere (black line), red line – in room atmosphere.

Sheet resistance measurement of treated samples showed that lower resistance was achieved on the samples treated in a nitrogen atmosphere with the lowest sheet resistance of $30 \Omega/\text{sq}$, whereas after treatment in a room atmosphere, the lowest achieved sheet resistance was $100 \Omega/\text{sq}$.

3.1.7. Modelling of the Polyimide temperature after laser pulse exposition to a substrate

Simulation of temperature dynamics after laser irradiation was carried out using COMSOL Multiphysics software. Transient temperature distribution in $127 \mu\text{m}$ -thick Polyimide (Kapton) film was simulated using the pulsed laser irradiation with the Gaussian beam profile and various wavelengths of radiation.

The finite element method was used to solve the transient heat conduction equation (10) [155, 156]. The 3D model was built for the Gaussian laser beam heat source (11), assuming that 80 percent of absorbed laser energy was absorbed by linear absorption. The first modelling was performed with the conditions when the applied irradiation dose of 1064 nm to the polyimide sample surface was 7.34 J/cm^2 . At this irradiation dose, we received the lowest sheet resistance ($8 \Omega/\text{sq}$) of formed graphene structure when irradiating with

1064 nm at ambient atmosphere, which correspond to the optimal processing conditions.

The initial temperature of a sample was set to 296 K. The heat source was applied for 430 pulses scanned in the line with an X_l shift of 1 μm (which correspond our experimental conditions of 100 kHz and 100 mm/s).

$$\rho C \frac{\partial T}{\partial t} = \nabla(\kappa \nabla T) + Q, \quad (10)$$

ρ is the material density (1.42 g/cm² for Polyimide), κ is the thermal conductivity (0.12 W/m·K for Polyimide), Q is the heat source, T is the temperature, C is the thermal heat capacity (1.09 J/g·K), t is time.

$$Q_n = \frac{2P}{f t_p \pi w_0^2} \alpha (1 - R) \exp\left(-\frac{2(x-x_n)^2}{w_0^2} - \frac{2(y-y_n)^2}{w_0^2}\right) \exp(-\alpha z) \text{rect}(t/t_p), \quad (11)$$

Here, α is the absorption coefficient of polyimide (4.9512 cm⁻¹ for Polyimide at 1064 nm), R is the reflection coefficient of polyimide (0.077 at 0° angle of incidence) [157], P is the laser power, equal to 3.25 W. x_n and y_n are the shifts of the coordinate depending on the subsequent position of the pulse, w_0 is the laser beam radius (at energy level 1/e², it was 216 μm), z is the coordinate in the laser beam propagation direction, t_p is the pulse duration (10 ps), $\text{rect}(t)$ is the rectangular function to turn off the heat source, n refers to the pulse number. A schematic illustration of pulse laser beam translation is given in **Figure 45**.

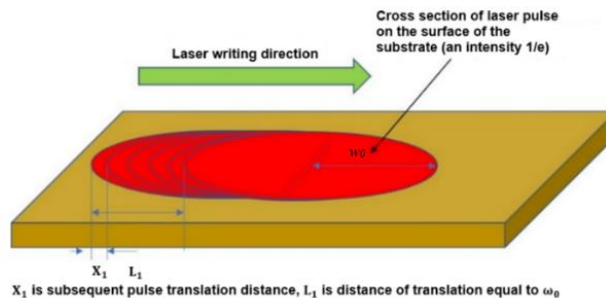


Figure 45. The schematic illustration of laser beam translation, used for thermal modelling.

The time interval between pulses was 10 μs (100 kHz). Irradiation with a dose of 7.34 J/cm² led to the temperature increase up to 1355 K. To transform Polyimide surface area into a low-sheet-resistance graphene layer, it was needed to irradiate the polyimide surface for 4.3 ms time duration and heat up the surface temperature to 1355 K (see **Figure 46**).

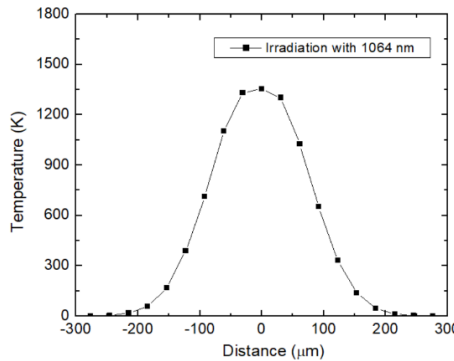


Figure 46. Temperature dependence at a particular point on PI surface relative to the laser beam center position. Zero value on x scale corresponds to the moment when laser pulse center hits the surface point. The laser wavelength is 1064 nm and the irradiation dose of 7.34 J/cm^2 .

Heat conduction modelling was also carried out for wavelengths of 532 nm, 355 nm, and 10600 nm. The modelling was performed at three different conditions with each wavelength: during the treatment with the maximal irradiation dose at which LIG still was formed, with the minimal irradiation dose high enough to form LIG, and with the optimal irradiation dose at which LIG with the lowest sheet resistance was produced. **Table 8.** represents the parameters, used in the heat conduction modelling with each wavelength.

Table 8. Parameters used for heat conduction modelling.

Wavelength, nm	1064	532	355	10600
Optical PI transmission, %	84	16	2	5
Average laser power, W	3.25	0.8	0.8	10
Pulse repetition rate, kHz	100	100	100	100
Pulse duration	10 ps	10 ps	10 ps	3 μ s
Scanning speed, mm/s	100	40	40	200
Optimal dose for the lowest sheet resistance LIG, J/cm^2	7.34	8.27	8.95	9.2
Min dose for LIG formation, J/cm^2	4.4	3.2	2.1	4.2
Max dose for LIG formation, J/cm^2	10.8	14	14.8	11.3
Beam radius for the optimal dose, μm	216	147	131	265
Beam radius for min dose, μm	367	215	310	610
Beam radius for max dose, μm	151	70	65	220
Absorption coefficient, cm^{-1}	4.95	77.59	27739	74.39 [158] [159]

Treatment with lower than the minimal irradiation dose resulted in no detectable changes on PI surface, while treatment with higher than the

maximal irradiation dose led to the formation of a soot layer on the PI surface. The irradiation with the optimal dose resulted in formation of graphene layer with the lowest sheet resistance.

The results of the heat conduction modelling at three different regimes with 1064 nm, 532 nm, 355 nm and 10600 nm are presented in **Figure 47**. The modelling parameters are listed in **Table 8**.

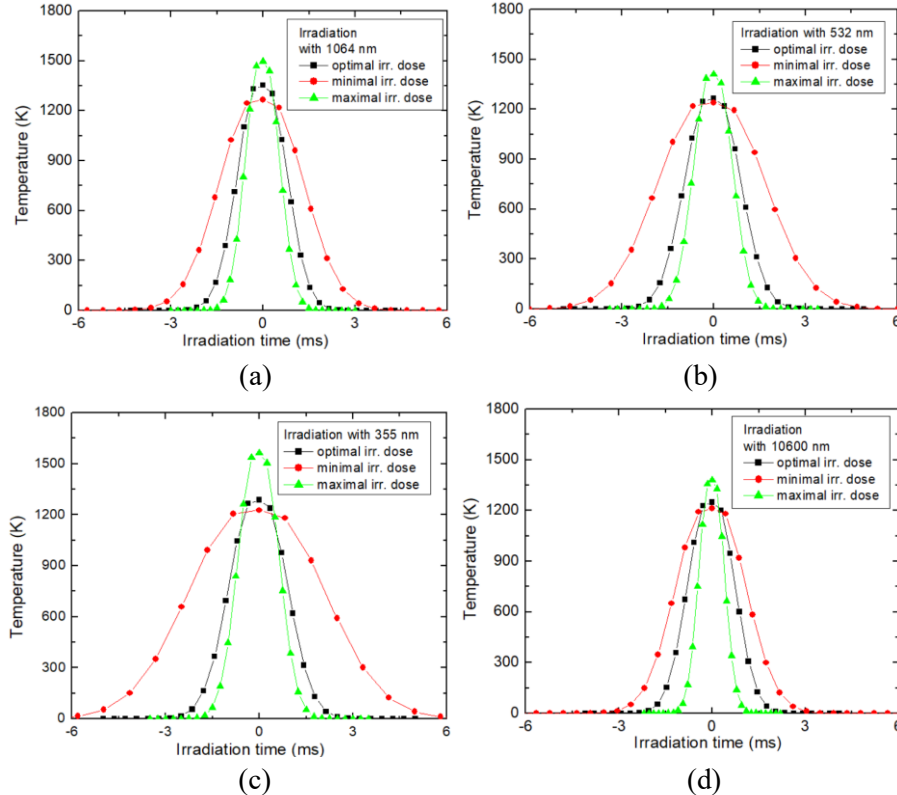


Figure 47. Variation of the surface temperature on a particular point of polyimide when scanning laser beam passes it. Zero time corresponds to the moment just after the laser pulse, which center hits the surface point. The laser irradiation at wavelengths of 1064 nm (a), 532 nm (b), 355 nm (c) and 10600 nm (d) in three different regimes: fabrication with the minimal, maximal and optimal irradiation doses for LIG formation.

The modelling results indicate that LIG could be formed on the polyimide surface when heated up to temperatures ranging from 1213 K to 1564 K. The time duration when the temperature was above 1000 K, was from 0.8 to 3.4 ms. To form the lowest sheet resistance LIG, the PI surface should be heated to between 1249 and 1355 K, and the temperature of polyimide surface should

be kept above 1000 K for 1.2 – 1.6 ms time duration. All the modelling results are presented in **Table 9**. Irradiation time for graphene formation with 355 nm or 532 nm wavelength was a bit longer than with infrared radiation (1064 nm or 10.6 μm). This could be related to the dominance of photothermal process on the sample surface, when irradiating with lower energy infrared photons, and heating and pyrolysis occurs on the sample. On the other hand, when irradiating with 355 nm or 532 nm, photon energy is high enough to directly break C-C, C-O, C-N the bonds and form graphene and photochemical process take effect.

Table 9. The highest temperature of the PI surface spot, which was treated with different laser wavelengths at various limiting irradiation doses.

Laser wavelength, nm	1064	532	355	10600
PI surface maximal temperature required to form LIG with the lowest sheet resistance (optimal regime), K	1355	1268	1288	1249
PI surface maximal temperature after treatment with min irradiation dose, K	1267	1241	1227	1213
PI surface maximal temperature after treatment with max irradiation dose, K	1497	1411	1564	1381
Time, when PI surface temperature is >1000 K (optimal regime), ms	1.4	1.5	1.6	1.2
Time, when PI surface temperature is >1000 K (after treatment with min irradiation dose), ms	2.2	2.7	3.4	1.7
Time, when PI surface temperature is >1000 K (after treatment with max irradiation dose), ms	1.1	1.2	1.3	0.8

Figure 48. show the variation of the surface temperature after laser irradiation required to form LIG with the lowest sheet resistance (optimal irradiation dose). The surface temperature required to convert polyimide to LIG is similar and it is ranging from 1249 K to 1355 K.

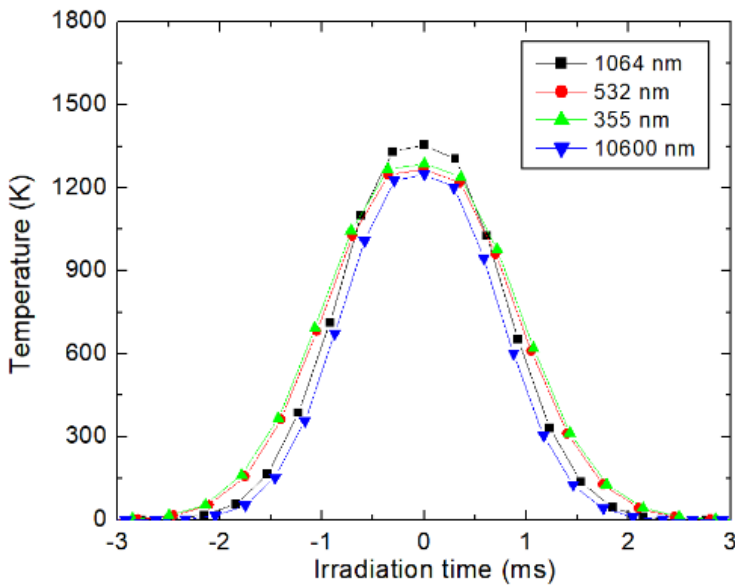


Figure 48. Temperature dynamics of a certain point of polyimide surface during laser irradiation at wavelengths of 355 nm, 532 nm, 1064 nm, and 10600 nm, with optimized parameters to achieve the lowest sheet resistance of LIG on a PI surface.

Figure 49. (a) illustrates the minimal, optimal, and maximal temperatures required for LIG formation on a polyimide surface. The minimal temperature marks the threshold at which LIG starts to form—below this point, no graphene formation was detected. The minimal temperature is achieved when irradiated with a minimal irradiation dose. On the other hand, the maximal temperature is the highest temperature at which LIG still could be formed; exceeding this temperature results in surface burning and the formation of a soot layer. The maximal temperature is achieved when irradiated with a maximal irradiation dose. The optimal temperature is the specific surface temperature of the polyimide required to produce a graphene layer with the lowest sheet resistance. The temperatures of PI surface need to be kept for a specific time in order to form LIG. **Figure 49 (b)** depicts the irradiation time required to maintain the polyimide (PI) surface at a specific temperature for LIG formation. Successful LIG formation occurs when the PI surface is irradiated within a defined time range, using the appropriate fluence to achieve the necessary temperature. If the irradiation time is too short, no changes will occur on the PI surface, whereas excessive irradiation above the maximal time will result in surface burning and soot layer formation. The PI surface temperature can be controlled by adjusting laser fluence, while irradiation

time is regulated through scanning speed and pulse repetition rate. The fluence required to achieve suitable temperatures for LIG formation on the PI surface ranges from 0.002 J/cm^2 to 0.052 J/cm^2 .

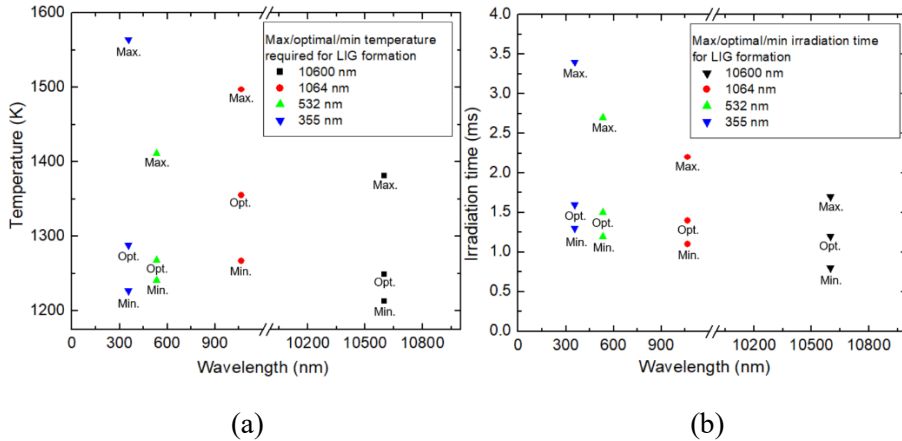


Figure 49. Minimal, optimal and maximal temperatures (a) and irradiation times (b) required to form LIG on polyimide surface after irradiation with different wavelengths are shown.

Our heat conduction modeling correlates with other results found in the literature. In R. Trusovas publication, the graphene oxide surface was heated by laser to a temperature of up to 1127 K using a 1064 nm wavelength to form graphene [140].

3.1.8. Summary

Treatment with picosecond laser pulses was found to be more suitable for polyimide surface modification than nanosecond laser. Lower sheet resistance could be achieved after fabrication with picosecond pulses, and no sample deformations due to the heating effects were observed in this regime.

Polyimide laser treatment at the focal plane led to soot formation with the sheet resistance as low as $30 \Omega/\text{sq}$. Treatment with a defocused 1064 nm laser beam led to the formation of a smooth, grey-colored graphene layer with sheet resistance as of $8 \Omega/\text{sq}$. The irradiation doses required to form graphene with 1064 nm were from 4.4 J/cm^2 to 10.8 J/cm^2 (sample distance to the focal plane from 5 to 12 mm). LIG adhesion to the surface was weak.

Treatment with 355 nm and 532 nm led to the formation of LIG layer with a sheet resistance as low as $18 \Omega/\text{sq}$. after treatment with 355 nm, and $13 \Omega/\text{sq}$. after treatment with 532 nm. PI treatment with mid-IR wavelength ($10.6 \mu\text{m}$) led to the formation of a conductive LIG layer with sheet resistance of 7

Ω/sq . The lowest sheet resistance was achieved when the sample was treated in a nitrogen atmosphere with a defocused 1064 nm laser beam. The sheet resistance was $5 \Omega/\text{sq}$. The surface morphology of LIG, formed after irradiation with 355 nm and 532 nm differed with the surface morphology, formed by 1064 nm or $10.6 \mu\text{m}$ radiation. The formed LIG adhesion after irradiation with 355 nm and 532 nm was much stronger than after irradiation with IR.

The heat conduction modeling has shown that the polyimide sample surface must be heated up above 1000 K for at least 1.4 ms time duration to form a conductive LIG layer.

3.2. Raman spectra analysis of treated surfaces

Raman spectra were taken from polyimide samples treated with various wavelengths at the focal plane, out of the focal plane, and treated in a room or nitrogen atmosphere. Raman spectra are the main LIG characterization method.

3.2.1. Raman spectra investigation of samples treated with 1064 nm laser wavelength

Raman spectra of graphene-like materials show standard features in the $1000\text{--}3000 \text{ cm}^{-1}$ region. The G-peak at $\sim 1560 \text{ cm}^{-1}$ corresponds to the E_{2g} phonon in the Brillouin zone center. The D-peak at $\sim 1360 \text{ cm}^{-1}$ is due to the breathing modes of sp^2 atoms and requires a defect for its activation. Therefore, this peak shows the presence of structural defects in graphene. The 2D peak at $\sim 2700 \text{ cm}^{-1}$, the second order of the D-peak, is the most intrinsic to graphene [160]. The intensity ratio for the D, G, and 2D Raman bands is often used to evaluate the graphene phase quality. The lower $I(\text{D})/I(\text{G})$ ratio indicates the lower defect number in graphene, whereas the higher $I(\text{2D})/I(\text{G})$ ratio indicates the lower number of graphene layers. So, the minimum of $I(\text{D})/I(\text{G})$ and a maximum of $I(\text{2D})/I(\text{G})$ correspond to the highest quality of graphene and is the result desired to achieve in our experiment. Perfect single-layer graphene should have an $I(\text{2D})/I(\text{G})$ equal to 2 [160].

Treating samples at the focal plane with a highly focused beam led to soot formation on the sample surface. The well-known graphene quality parameters $I(\text{D})/I(\text{G})$ and $I(\text{2D})/I(\text{G})$ in the best case were accordingly 0.71 and 0.13 (see **Figure 50**).

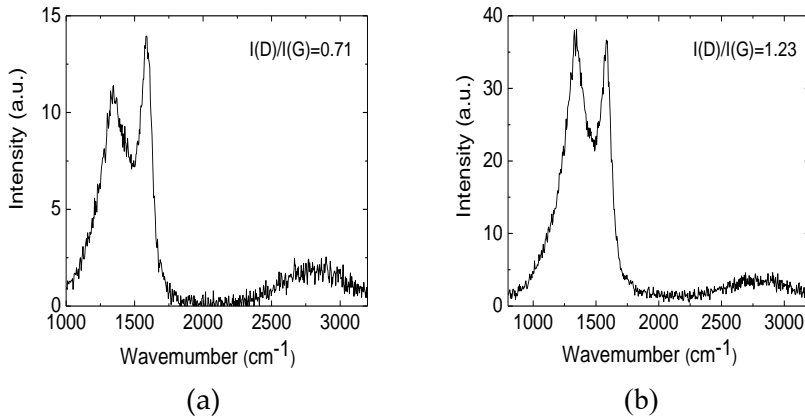


Figure 50. Raman spectra of surfaces treated at focal plane with 120 J/cm^2 (a) and 130 J/cm^2 (b).

Defocusing the laser beam led to changes in the formed structure on the PI sample surface. The dose varied from 130 J/cm^2 at the focal plane to 4.42 J/cm^2 at 12 mm below the focal plane at 1064 nm . An increase in the 2D peak was observed when the sample was lowered down by 4 to 10 mm below the focal plane, with the highest intensity peak at 7-8 mm below the focal plane (see **Figure 51**).

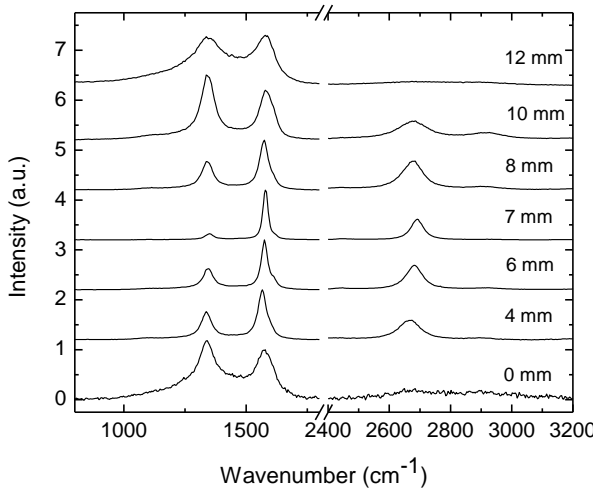


Figure 51. Raman spectra of surfaces treated at the focal plane and down to 12 mm below the focal plane.

Various Raman spectra parameters indicated the formation of high-quality LIG in a certain range of irradiation doses. A comparison of FWHM values for main spectral bands D, G, and 2D is presented in **Figure 52 (a)**. These bands exhibit a narrowing starting from the irradiation dose of 5.4 J/cm^2 , reaching a sharp FWHM minimum at 7.34 J/cm^2 (treatment when the sample was placed 7 mm below the focal plane). At that irradiation dose, $\text{FWHM(D)}=38.3 \text{ cm}^{-1}$, $\text{FWHM(G)}=24.4 \text{ cm}^{-1}$ and $\text{FWHM(2D)}=48.7 \text{ cm}^{-1}$. Above that dose, all spectral bands broaden significantly slower by further increasing the irradiation dose. A decrease of FWHM of the D and G corresponds to decreasing disorder in material [161]. FWHM of the 2D band also tends to decrease when the number of graphene layers decreases [162-164]. Raman spectrum obtained at the optimal irradiation dose of 7.34 J/cm^2 is shown in **Figure 52 (b)**. Sheet resistance of this sample – $8 \Omega/\text{sq}$. All spectral bands prominent to graphene are present: D-band with peak central position at 1350 cm^{-1} , G-band at 1579 cm^{-1} , and 2D-band at 2691 cm^{-1} . It is worth noting that the D-band, representing the structural defects, possesses particularly low intensity compared to the G-band. Intensity ratios $I(2D)/I(G)$ and $I(D)/I(G)$ are recognized markers for the investigation of graphene. In this case, the $I(2D)/I(G)=0.4$ and $I(D)/I(G)=0.1$.

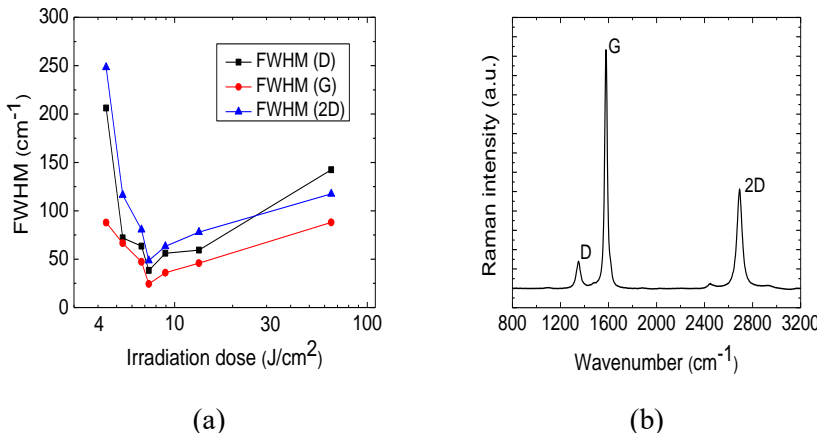


Figure 52. Dependence of FWHM of D, G, and 2D bands on the irradiation dose (a); Raman spectra of LIG in PI achieved after treatment with 7.34 J/cm^2 irradiation dose (b).

Structural defects of graphene can be assessed using the information provided by Raman spectra. Line defects can be identified by the average crystallite size L_α . The spatial confinement of the crystallites determines the

width of the G-band, and L_α can be approximately determined by the equation [163]:

$$L_\alpha = \frac{l_c}{2} \ln \left[\frac{C}{FWHM(G) - FWHM(G_0)} \right], \quad (12)$$

where the coherence length $l_c = 32$ nm, $C = 95$ cm⁻¹, and $FWHM(G_0)$ is the width of the G-band of undoped pristine graphene (15 cm⁻¹).

Using this equation, the crystallite size of LIG was evaluated at various irradiation doses. Dependence is plotted in **Figure 53**. The apparent maximum crystallite size was 37 nm when a 7.34 J/cm² irradiation dose was applied. The dose value coincides with the narrowest FWHMs for spectral D, G, and 2D bands. At this dose, a minimum of $I(D)/I(G) = 0.1$. On the other hand, the maximum value of $I(2D)/I(G) = 0.58$ ratio was reached at a lower irradiation dose of 6.72 J/cm².

To conclude, spectral band intensity ratios, together with estimated crystallite size and FWHM of prominent spectral bands, indicate that structural properties of LIG can be tuned by varying laser irradiation doses. LIG formation with minimal structural defects and fewer layers of graphene structures with the largest crystallites is in the range of irradiation doses 5.73-13.4 J/cm². Furthermore, the formation of the best quality LIG – closest to spectral properties of graphene is at the irradiation dose of 7.34 J/cm².

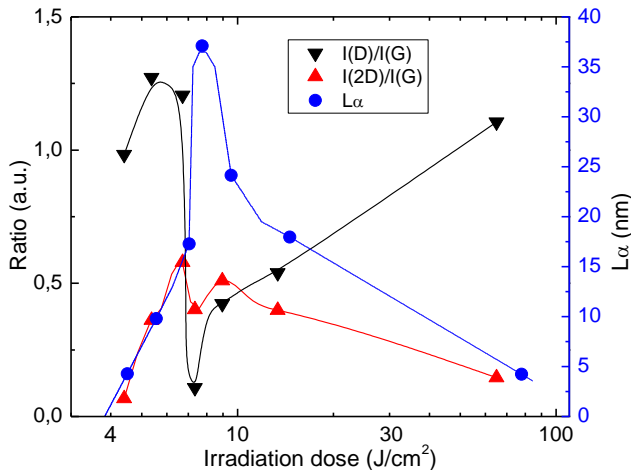


Figure 53. Dependence of $I(D)/I(G)$ and $I(2D)/I(G)$ intensity ratios and crystallite size L_α on laser irradiation dose at 1064 nm.

3.2.2. Raman spectra of samples treated with 355 nm and 532 nm laser wavelengths

Raman spectroscopy measurements were performed on the samples, treated in a room atmosphere with a defocused laser beam at 355 nm and 532 nm wavelengths. As mentioned in **Chapter 3.1.3**, the LIG structure formed with a UV or VIS wavelength laser differs from that formed with IR. LIG, formed with UV or VIS, is better bonded to the surface but has a higher sheet resistance. The different laser-polyimide interaction mechanisms take effect when exposed to different wavelengths: in the IR case, the photothermal effect is dominant, and in the UV or VIS cases – photochemical.

The lowest achieved sheet resistance of samples treated with the defocused beam at 355 nm wavelength was $18 \Omega/\text{sq}$. and with 532 nm - $13 \Omega/\text{sq}$. Intensity peak ratios, the well-known graphene quality parameters in this case, were $I(D)/I(G)=1.05$ and $I(2D)/I(G)=0.5$ for samples treated with the 355 nm defocused laser beam at an irradiation dose of 7.5 J/cm^2 and $I(D)/I(G)=0.92$, $I(2D)/I(G)=0.65$ were for samples treated with defocused 532 nm wavelength at an irradiation dose of 6.8 J/cm^2 (see **Figure 54**).

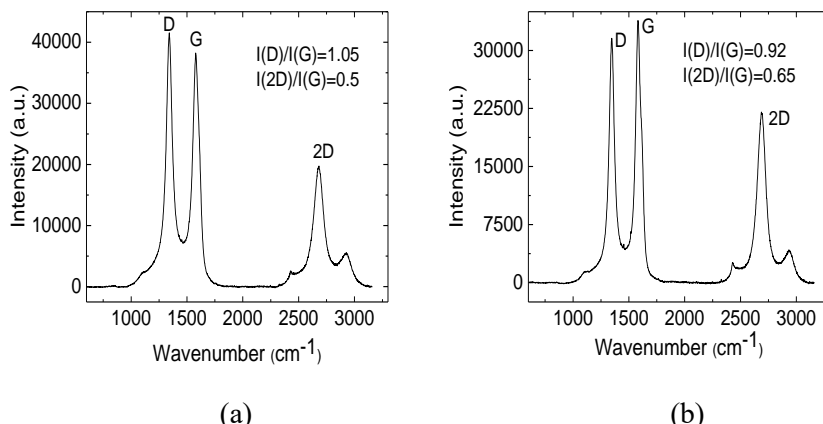


Figure 54. Raman spectra are shown of the samples, treated with a defocused laser beam at 355 nm and irradiation dose 7.5 J/cm^2 (a), 532 nm, and irradiation dose 6.8 J/cm^2 (b).

3.2.3. Raman spectra of samples treated with 1064 nm laser wavelength in a nitrogen atmosphere

Further, samples treated with a defocused 1064 nm wavelength beam in the nitrogen atmosphere were measured. During the treatment conducted within

an inert atmosphere, the lack of an oxidizing agent resulted in the generation of a relatively stable configuration of graphene. Treating samples with an irradiation dose of 7.3 J/cm^2 and 7.8 J/cm^2 in a nitrogen chamber led to the formation of the highest intensity 2D peaks in our experiment (see **Figure 55**). The intensity ratios $I(D)/I(G)$ and $I(2D)/I(G)$ of samples treated with 7.3 J/cm^2 were accordingly 0.46 and 0.81. The intensity ratios of samples treated with 7.8 J/cm^2 were 0.6 and 0.81. The sheet resistance of samples treated in a nitrogen chamber with irradiation doses of $7.3 - 7.8 \text{ J/cm}^2$ was also the lowest in our experiment and equal to $5 \Omega/\text{sq}$.

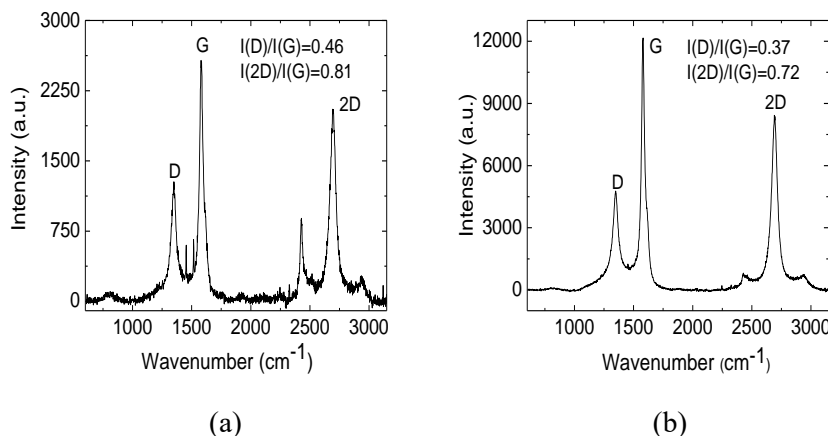


Figure 55. Raman spectra of the sample surfaces, treated with 1064 nm wavelength at 7 mm below the focal plane in the nitrogen atmosphere, with 7.3 J/cm^2 (a) and 7.8 J/cm^2 (b).

3.2.4. Raman spectra of samples treated with $10.6 \mu\text{m}$ laser wavelength

Raman spectra were measured on the samples, treated with $10.6 \mu\text{m}$ wavelength when a sample was moved down to 42 mm from the focal plane in 3 mm steps. The highest intensity 2D peak was observed on the sample, which was treated at a 9 mm distance from the focal plane with an irradiation dose of 8.6 J/cm^2 , and the sheet resistance of the formed structure was $7 \Omega/\text{sq}$. In this case, $I(D)/I(G)=0.57$ and $I(2D)/I(G)=0.63$. The results strongly correlated with sheet resistance measurements of the sample surfaces treated at various distances to the focal plane. Intensity ratios $I(2D)/I(G)$ were highest when the sheet resistances of the treated sample surfaces were lowest, and the intensity ratio value decreased when sheet resistance increased (see **Figure 56**).

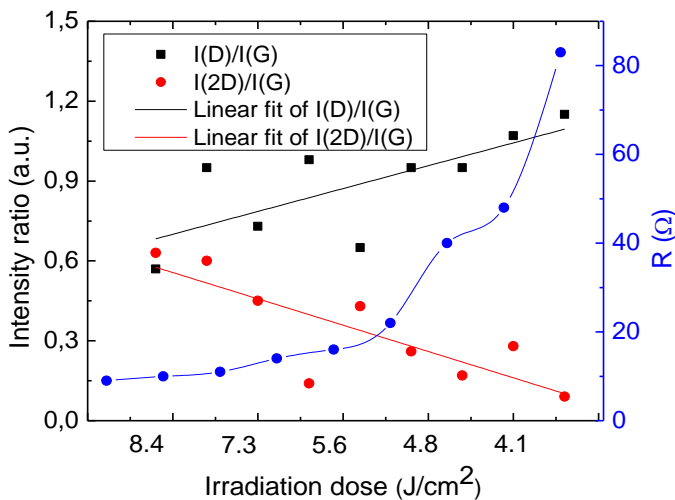


Figure 56. Sheet resistance dependence on the irradiation dose after treatment with a CO₂ laser (blue line). Dependence of intensity ratio I(D)/I(G) (black line) and I(2D)/I(G) (red line) on the irradiation dose.

Table 10. presents the lowest sheet resistances and best Raman spectra characteristics of the samples treated with various laser wavelengths. The results showed that LIG with the lowest sheet resistance and best Raman spectra characteristics could be formed on the PI surface after irradiation with the defocused 1064 nm beam in the nitrogen atmosphere. Eliminating oxygen in an inert atmosphere laser treatment promoted stability in the graphene structure.

Table 10. Sheet resistance and Raman spectra parameters after picosecond laser treatment with different wavelengths.

Wavelength, nm	Irradiation dose, J/cm ²	Sheet resistance, Ω/sq.	Adhesion	I(D)/I(G)	I(2D)/I(G)
355	7.5	18	Strong	1.05	0.5
532	6.8	13	Strong	0.92	0.65
1064	7.3	8	Weak	0.1	0.4
10600	8.6	7	Weak	0.57	0.63
1064, in the N ₂	7.3	5	Weak	0.46	0.81
1064, in the N ₂	7.8	5	Weak	0.37	0.72

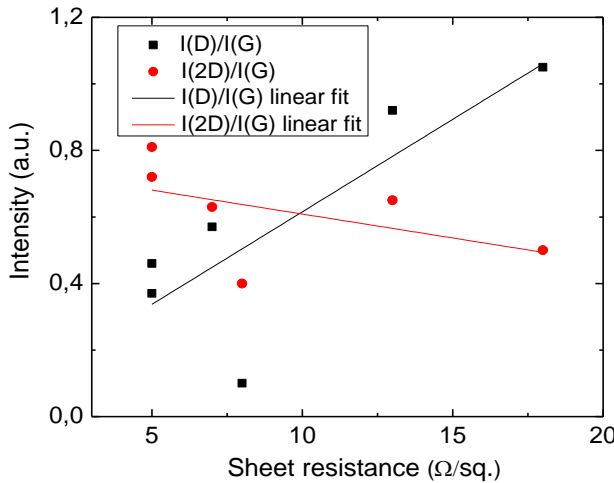


Figure 57. Intensity ratios $I(D)/I(G)$ and $I(2D)/I(G)$ dependence from sheet resistance experimental points and linear fit showing the trend of Raman spectra ratios according to sheet resistance.

According to V. Kumar's group research [161], the Raman spectra intensity ratio $I(2D)/I(G)$ is approximately equal to 2 when there is a single-layer graphene case. If $I(2D)/I(G)=1$ (approx.), it is double-layer graphene; when $I(2D)/I(G)=0.8$ (approx.), it is few-layer (less than 5 layers) graphene; when $I(2D)/I(G)=0.5$ (approx.), so it is multi-layer graphene (less than 10 layers). Our best result was when the PI sample was treated with a defocused 1064 nm laser beam in a nitrogen atmosphere. The $I(2D)/I(G)$ ratio was 0.81 in this case. Therefore, it could be assumed that treatment in a nitrogen atmosphere could potentially lead to the formation of a few-layer graphene. During the other treatments, with different wavelengths in the room atmosphere, the $I(2D)/I(G)$ ratio showed that a multi-layer graphene was formed. The same correlation could be adapted to the sheet resistance measurement. When the sheet resistance of the laser-treated surface is 5 Ω/sq . or less, few-layer graphene is expected; when 5-30 Ω/sq ., it could be multi-layer graphene. If the sheet resistance is more than 30 Ω/sq ., no graphene but soot is formed after laser treatment on a Polyimide surface.

Treating polyimide at the focal plane can lead to the formation of a thick soot layer on the surface with sheet resistance as low as 30 Ω/sq . Treating with a defocused laser beam, the LIG structure with a sheet resistance as low as 5 Ω/sq . could be formed in the nitrogen atmosphere. The sheet resistance of clean polyimide (not treated by laser) is around $10^9 \Omega/\text{sq}$. After laser treatment,

it could be reduced by approximately 8 orders of magnitude to $10^1 \Omega/\text{sq}$. According to Markovska's group research [165], the resistivity of other polymers ranges from $2 \times 10^7 \Omega$ to more than $10^{15} \Omega$. Some rubber materials or polymer foams exhibit a resistivity as low as $10^3 \Omega$. The resistivity of conducting polymers could be $< 10^2 \Omega$. In our experiment, the laser-formed graphene electrical resistivity is lower than most semiconductor materials, comparable to conductive polymers, but by six orders of magnitude lower than the worst conducting metals. The LIG we formed is a better electrical conductor than most semiconductor materials. The resistivity of metals starts from $3 \times 10^{-6} \Omega$ to $10^{-8} \Omega$. The lowest resistivity has silver - $1.59 \times 10^{-8} \Omega$, copper - $1.68 \times 10^{-8} \Omega$, gold - $2.44 \times 10^{-8} \Omega$.

3.2.5. Summary

Raman spectra of samples treated in various regimes were taken. After treatment with a 1064 nm wavelength defocused laser beam, the Raman parameters $I(D)/I(G)$ and $I(2D)/I(G)$ in the best case were accordingly 0.1 and 0.4. After treatment with 355 nm, 532 nm and $10.6 \mu\text{m}$ – 1.05 and 0.5, 0.92 and 0.65, 0.57 and 0.63. The best Raman spectra characteristics were achieved after polyimide treatment with a defocused 1064 nm laser beam when a sample was placed in a nitrogen chamber. $I(D)/I(G)$ and $I(2D)/I(G)$ parameters were 0.37 and 0.72.

3.3. Electroplating of LIG surfaces

Electroplating was carried out on three distinct types of samples. The first category involved samples treated at the focal plane, forming a conductive soot layer. The second category comprised samples treated with a defocused infrared beam, leading to the formation of smooth, low-sheet-resistance LIG. The third category involved samples treated with a defocused visible or ultraviolet beam, resulting in lower-quality LIG compared to the infrared-treated samples. It is important to mention that typically electroplating is used to deposit metals, which bulk resistivity starts from $3 \times 10^{-6} \Omega$ to $10^{-8} \Omega$.

Copper was mainly used for metal deposition due to its significant role in electronic applications. Additionally, nickel, cobalt, zinc, and silver were employed for plating on LIG.

3.3.1. Copper plating on LIG formed with 1064 nm wavelength

The copper deposition on laser-treated Kapton PI films was performed using electroplating in an acidic copper bath (see **Figure 29**). Plating was performed

on a 10 x 20 mm size rectangle laser-treated area. The top part of that area was used to attach an electrode and, therefore, was not covered by metal. The coverage by a metal of the laser-treated area depended on the sheet resistance of the polymer. Low sheet resistance (high conductivity) facilitated the instantaneous deposition of metal on the whole laser-treated area not covered by the electrode. In the case of high sheet resistance, the metal film started to grow from the electrode down over the laser-treated area. Therefore, the thickness of the metal film was not uniform (thick near the electrode, thin or absent on the opposite side of the area).

The applied current density was the main parameter for the electroplating. The optimized plating current and electrolysis conditions on different types of surface treatment were determined from the voltammogram of Cu deposition on laser-treated polyimide (see **Figure 58**).

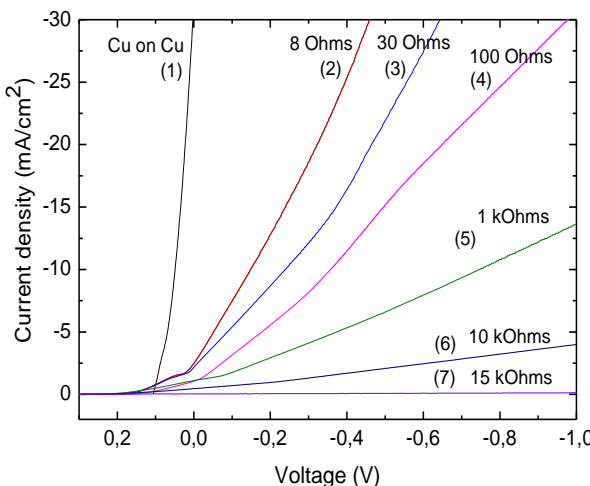


Figure 58. The voltammograms of Cu deposition on laser-treated surfaces with different sheet resistances. The voltammogram of Cu on Cu was also performed as a reference. The potential sweep rate was 2 mV/s, and the potentials were given versus the Ag/AgCl/KCl (sat.) electrode. The measurements were carried out at room temperature using the potentiostate/galvanostate Reference 600 (Gamry Instruments).

The current density that could be applied for plating depended on the sheet resistance of the treated surface. An increase in the treated-surface sheet resistance resulted in decreased cathode current that could be applied. When sheet resistance increases, the Cu electrodeposition curve shifts to the negative

side. The negative shift increases the overpotential of the Cu electrodeposition at a constant current density. For example, during the plating on the LIG structure (8 $\Omega/\text{sq.}$, curve 2, **Figure 58**), the current density of 10 mA/cm² was at a low voltage of -0.17 V, in contrast, plating on the soot surface with a sheet resistance of 100 $\Omega/\text{sq.}$ (curve 4, **Figure 58**) was achieved when the voltage was -0.34 V. During the plating on higher sheet resistances than 100 $\Omega/\text{sq.}$ (curves 5-7, **Figure 58**), a significant decrease in plating current was observed. The best plating results were achieved when plating on LIG (curve 2, **Figure 58**). It was almost like copper-on-copper plating (curve 1, **Figure 58**).

Two types of surfaces were formed on the PI sample after laser treatment with 1064 nm: soot formed when treated with a high-intensity beam at the focal plane and down to 3 mm below the focal plane. Surface sheet resistance varied at these irradiation doses from 20 M $\Omega/\text{sq.}$ to 30 $\Omega/\text{sq.}$ (curves 3-7, **Figure 58**). LIG structures formed when the sample was placed from 5 mm to 12 mm below the focal plane, with a sheet resistance of 8 $\Omega/\text{sq.}$ (curve 2, **Figure 58**). Selective copper deposition on the laser-treated surface was possible when the treated surface sheet resistance was 10 k $\Omega/\text{sq.}$ or lower.

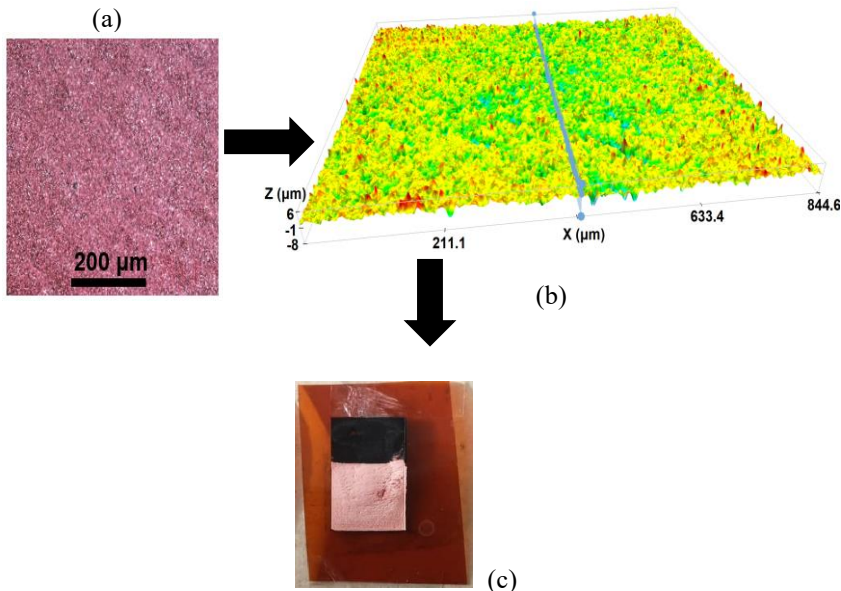


Figure 59. (a) homogeneous copper layer plated on the LIG surface (magnified x10). (b) 3D optical profilometer image of copper-plated sample surface topography, and the line shows 2D surface topography along the middle of the image. (c) Laser-treated samples after copper electroplating are shown.

However, the deposition of metals on sheet resistance of $10 \text{ k}\Omega/\text{sq}$. was uneven. Much more metal was deposited around the cathode than on the other side of the sample. To plate the whole treated area with a uniform layer of copper was possible only when the sheet resistance of the sample surface was lower than $100 \Omega/\text{sq}$. The thickness of a copper layer of $10\text{-}20 \mu\text{m}$ was required to get full uniform coverage of the laser-treated area on the samples treated at the focal plane where soot formed (sheet resistance of formed soot was $30\text{-}100 \Omega/\text{sq}$.). Copper plating on LIG (sheet resistance of $8 \Omega/\text{sq}$.) formed a thin and homogeneous copper layer. A minimal thickness of only $5\text{-}7 \mu\text{m}$ was needed on LIG to uniformly cover this type of laser-treated area (**Figure 59**).

3.3.2. Copper plating on LIG formed with 532 nm wavelength

Different LIG surface patterns formed after treatment with infrared and visible or ultraviolet wavelengths, as presented in **Figure 41**. LIG, formed after the treatment with 355 nm or 532 nm radiation, was better bonded to the sample surface than with 1064 nm or $10.6 \mu\text{m}$, although this LIG has higher sheet resistance. Therefore, PI samples treated with 532 nm wavelength were also selected for metal plating experiments. The smallest copper thickness required for full coverage of the area of the formed $13 \Omega/\text{sq}$. LIG layer was $3 \mu\text{m}$. On samples with a higher sheet resistance, a thicker layer of copper was required to get full coverage of the patterned area: $25 \Omega/\text{sq}$. - $7 \mu\text{m}$ thickness copper layer, $30 \Omega/\text{sq}$. - $10 \mu\text{m}$ thickness copper layer (see **Figure 60**).

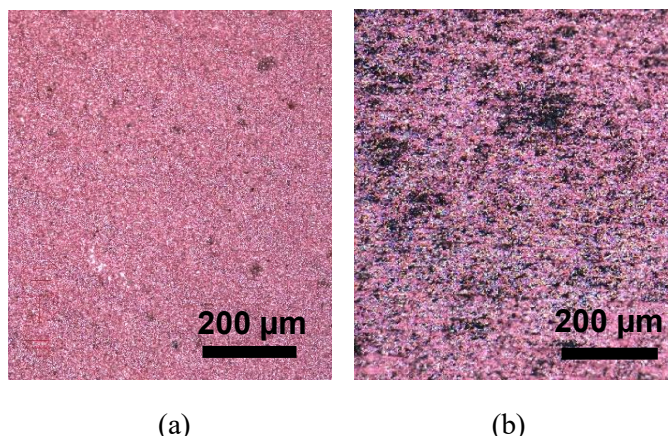


Figure 60. (a) a uniform $7 \mu\text{m}$ thickness copper layer deposited on the LIG surface with a sheet resistance of $13 \Omega/\text{sq}$. Surface coverage by metal after plating – 98 %, (b) copper deposited on the LIG surface with a sheet resistance of $100 \Omega/\text{sq}$. Surface coverage after the plating – 76 %.

We did not succeed in uniform, defect-free plating when the treated surface sheet resistance was higher than $100 \Omega/\text{sq}$. The plating was uneven, with many undeposited areas, and plating was more intensive around the cathode terminal. A LIG layer with a low sheet resistance is needed to deposit a smooth metal layer. The lower the surface sheet resistance, the thinner and continuous metal layer could be deposited.

3.3.3. LIG deposition with other metals

LIG surface was also plated with silver (Ag), nickel (Ni), tin (Sn), cobalt (Co) and zinc (Zn). Silver has the highest electrical conductivity of all metals [166] and is widely used to produce electrical tracks in electronics. On the other hand, nickel is an excellent material for electroplating due to its compactness: nickel could be selectively plated on very small structures [167]. Also, nickel is used as a sublayer for copper deposition in electronics to enhance adhesion [168, 169]. Tin, cobalt, and zinc are also used for electroplating to increase hardness, corrosion resistance, etc.

Plating was performed on LIG samples treated with 532 nm with a sheet resistance of $13 \Omega/\text{sq}$. The lowest deposited layer thickness required for the entire deposition of LIG with silver was 9 μm , with nickel was 1 μm , with tin was 7 μm , cobalt - 2 μm , and zinc - 10 μm . A conclusion can be drawn from this, that the deposited metal layer thickness depends not only on the surface sheet resistance but also on the metal origin to be deposited as.

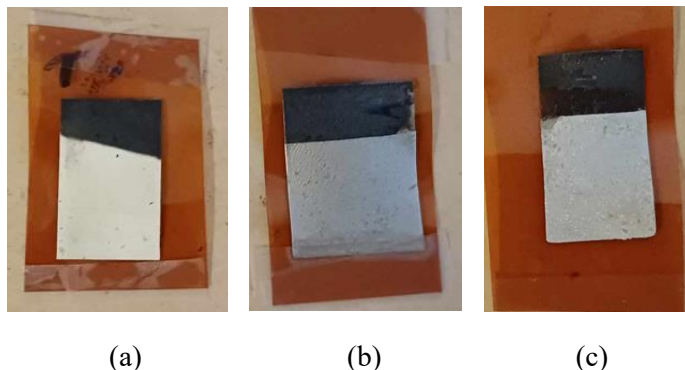


Figure 61. (a) 532 nm treated LIG sample with a sheet resistance of 13Ω deposited with a 10 μm thickness of the silver layer, (b) with a 10 μm thickness of the nickel layer, and (c) with a 10 μm thickness of the tin layer.

3.3.4. Summary

The copper electro-plating on the polyimide surface is possible when sheet resistance on the laser-formed conductive layer is lower than $10 \text{ k}\Omega/\text{sq}$. In this case, the copper deposition will be uneven – a thicker layer of copper will be deposited on the areas around the anode. To deposit the surface with a uniform metal layer, structures with a sheet resistance of $100 \Omega/\text{sq}$. or lower is required.

The thinnest copper layer required to uniformly deposit LIG was $3 \mu\text{m}$. This copper layer was deposited on a sample treated with a 532 nm defocused laser beam with a sheet resistance of $13 \Omega/\text{sq}$. Zinc, silver, tin, cobalt, and nickel were also deposited on these samples. The lowest thickness of zinc deposited layer was $10 \mu\text{m}$, silver - $9 \mu\text{m}$, tin - $7 \mu\text{m}$, cobalt - $2 \mu\text{m}$ and nickel $1 \mu\text{m}$.

LIST OF CONCLUSIONS

1. Treatment with picosecond laser pulses was found to be more suitable for polyimide PI sample surface modification than with a nanosecond laser. Lower sheet resistance could be achieved after treatment with picosecond pulses. Also, no sample deformations were observed in this regime.
2. It was shown that laser process parameters significantly impact sheet resistance. Treatment with a 1064 nm focused high-intensity beam led to soot formation on the sample surface, whose sheet resistance was strongly dependent on the irradiation dose and could be adjusted by changing laser power. Treatment out of focus led to laser-induced graphene formation.
3. To form polyimide into graphene, polyimide surface temperature should be kept at a specific temperature for a certain time duration. For LIG formation on PI surface, the optimal irradiation duration is 1.4 ms irradiating with a dose of 7-9 J/cm².
4. The morphology of the formed LIG surface differed when treated with infrared and visible or ultraviolet radiation. Irradiation with an infrared laser resulted in low sheet resistance LIG (8 Ω/sq.) with a very smooth surface but with cracks and weakly bonded to the sample surface, while treatment with visible and ultraviolet lasers produced LIG with higher sheet resistance (13 Ω/sq.), a rougher LIG surface however well bonded to the sample surface.
5. The highest-quality LIG was obtained when the sample was treated with a defocused 1064 nm laser beam in a nitrogen atmosphere. Irradiation doses from 7.3 J/cm² to 7.8 J/cm² were used to form LIG with an excellent surface sheet resistance of 5 Ω/sq. Raman spectra of treated samples showed the highest intensity ratio $I(2D)/I(G) = 0.81$. The $I(D)/I(G)$ was 0.46.
6. The sheet resistance of the LIG structure was correlated with the Raman spectra peaks $I(D)/I(G)$ and $I(2D)/I(G)$ ratios. Low sheet resistance indicated a higher $I(2D)/I(G)$ ratio and a lower $I(D)/I(G)$ ratio.
7. The thickness and uniformity of electroplated metal layers on the LIG surface were strongly correlated with its sheet resistance; thinner and more uniform metal layers, covering the whole area were obtained on surfaces with a lower sheet resistance. Higher sheet resistance required thicker metal layers to achieve full coverage.
8. The lowest copper layer thickness required to electroplate the entire laser-treated LIG area was 3 μm. To deposit on the laser-formed soot layer, it was 10-20 μm. The uniform copper layer could not be deposited when

sheet resistance was higher than 100 Ω/sq . The metal deposition was impossible when the laser-treated surface sheet resistance was higher than 10000 Ω/sq .

9. The type of metal affected the minimal thickness of the metal layer required for full coverage of the conductive LIG layer (13 Ω/sq). For copper, it is 3 μm , for silver - 9 μm , for nickel - 1 μm , for tin - 7 μm , cobalt - 2 μm and zinc – 10 μm .

SANTRAUKA

Pastarųjų dešimtmečių pažanga puslaidininkų pramonėje lėmė įvairių elektronikos prietaisų miniatiūrizavimą. Atsirado poreikis gaminti vis mažesnius elektronikos komponentus, taip pat atsirado vis didėjantis poreikis elektronikos komponentus gaminti ant lankstaus pagrindo arba trimačio paviršiaus. Klasikinės PCB (angl. *printed circuit board*) plokštės, naudojant klasikinius jų gamybos būdus, yra gaminamos plokščios formos, t.y. dvimatės, dėl to, jas dažnai būna sunku įtalpinti kai kuriuose prietaisuose kur erdvė yra ribota. Šią problemą dalinai galima būtų išspręsti naudojant technologijas, leidžiančias gaminti elektrai laidžius takelius ant trimačių paviršiaus.

Šio tiriamojo darbo tikslas yra sukurti lazeriu asistuotą metodą selektyviam elektrai laidžių takelių formavimui ant sudėtingos formos trimačių polimerinių paviršių. Metodas susideda iš kelių žingsnių: pirma, elektros grandinės raštas lazeriu yra užrašomas ant polimerinės detalės. Tuomet, detalė yra panardinama į indą su metalo, kuriuo norima dengti tirpalą, ir Jame galvaniniu būdu metalas yra nusodinamas ant lazeriu paveiktu vietų. Galvaniniu būdu metalu galima dengti tik elektrai laidžias detales, o polimerai iš prigimties yra nelaidžios elektrai medžiagos. Tačiau, yra tam tikra grupė polimerų, kuriuos paveikus lazerine spinduliuote, jų laidumas elektrai gali būti ženkliai padidintas. Kai kuriuos polimerus, paveikus tam tikrais lazerinės spinduliuotės parametrais, tose vietose gali susiformuoti grafenas, kuris yra laidus elektrai. Lazeriu suformuotas grafenas yra laidus ne tiek, kad būtų galima tiesiogiai tą detalę naudoti elektronikos prietaisuose, tačiau laidus pakankamai, kad būtų galima jo paviršių padengti metalu, galvaniniu būdu. Šiame darbe daugiausiai buvo dirbama su Kapton® HN 127 μm storio poliimido juosta. Poliimidas buvo pasirinktas dėl to, jog jo atomai yra susijungę į taip vadinamus aromatinius žiedus, o tokios cheminės struktūros medžiagose yra nesudėtinga lazeriu suformuoti grafeno sluoksnį. Taigi, gryno poliimido, nepaveikto lazeriu, varža yra $10^9 \Omega/\text{kv.}$, paveikus jį, galima suformuoti grafeno sluoksnį, kurio varža galėtų būtų apie $10 \Omega/\text{kv.}$, o padengus variu - $10^4 \Omega/\text{kv.}$ Šio metodo pagrindinis privalumas prieš tradicinius elektronikos plokščių gamybos metodus, tokius kaip fotolitografija, yra galimybė formuoti elektrai laidžius takelius ant trimačių paviršių. Taip pat, šis metodas yra greitaus, paprastas ir ekonomiškas.

Dėl savo ypatingų cheminių ir fizinių savybių, grafeno medžiagos sulaukia didelio dėmesio elektronikos pramonėje. Grafenas tai viena iš anglies atmainų, kurios anglies atomai yra išsidėstę šešiakampio korio formos gardelėse, vienoje plokštumoje. Kai tokį plokštumą yra daug, ir jos išsidėsčiusios su nedideliais tarpais ($\sim 0.335 \text{ nm}$) viena virš kitos, tuomet tai

Yra grafitas. Pirmą kartą grafeno struktūros koncepcija buvo paminėta dar 20 amžiaus viduryje, tačiau didelis proveržis įvyko 2004 metais, kuomet K. Novoselov ir A. Geim pavyko iš tūrinio grafito išskirti vieną sluoksnį grafeno naudojant lipnią juostą ir perkelti jį ant silicio padéklo. Už šį pasiekimą jie buvo apdovanoti Nobelio premija 2010 metais. Grafenas kaip medžiaga, išsiskiria savo unikaliomis savybėmis, tokiomis kaip aukštas šiluminis ir elektrinis laidumas bei itin didelis tvirtumas. Pagrindiniai grafeno charakterizavimo metodai tai Ramano spektroskopija (angl. *Raman spectroscopy*), leidžianti analizuoti grafeno sluoksnius, o paviršiaus morfologijai tirti naudojamas skenuojantis elektroninis mikroskopas (angl. *SEM, scanning electron microscope*). Grafeno sluoksnį skaičius gali būti nustatytas naudojant pralaidumo elektroninį mikroskopą (angl. *TEM, transmission electron microscope*), o grafeno gardelės sandara gali būti tiriamą Rentgeno spindulių difrakcijos metodu (angl. *XRD, X-ray diffraction*). Grafenas gali būti suformuotas mechaniniais metodais, kaip jau minėtu, lipnios juostos metodu, atplėšiant sluoksnį nuo grafito. Taip pat, grafenas gali būti atskirtas nuo grafito naudojant aštrius deimantinius skustukus. Grafenas gali būti užaugintas ant padéklo naudojant cheminį garų nusodinimo metodą (angl. *CVD, chemical vapor deposition*). Iškaitintą kamerą yra įleidžiamos anglies turinčios dujos (tokios kaip metanas (CH_4) ar etilenas (C_2H_4)), ir esant pakankamai aukštai temperatūrai, anglies atomai atsiskiria ir nusėda ant padéklo, suformuodama grafeno sluoksnį. Kontroliuojant kameros temperatūrą bei įleidžiamų dujų srautą, galima labai preciziškai kontroliuoti susiformuojančio grafeno sluoksnį skaičių. Grafeno formavimas lazeriu (angl. *LIG, laser-induced graphene*) būdas buvo atrastas 2014 metais, Rice universitete. Paveikus lazerine spinduliuote anglies pagrindu sudarytas medžiagas, jų anglies atomai persigrupuoja į šešiakampes korio formos gardeles, taip suformuodamos grafeną medžiagoje. Suformuoto grafeno kokybę ir sluoksnį kiekis gali būti kontroliuojamas, keičiant lazerinės spinduliuotės parametrus, tokius kaip galia, apdorojimo greitis ar ekspozicijos trukmė. Lazeriu formuoti grafeną yra labai patogu, nes galima jį formuoti ant sudėtingos formos trimačių detalių, be to, tai greitas ir sąlyginai pigus bei nesudėtingas procesas.

Be mūsų kuriamo metodo, taip pat yra keletas kitų lazeriu asistuotų metodų elektrai laidžių takelių formavimui. Bene labiausiai naudojamas metodas tai tiesioginis lazerinis išryšumas (angl. *LDS, laser direct structuring*). Tai dviejų žingsnių procesas, kur pirmajame žingsnyje lazeriu yra užrašomas elektros grandinės raštas detalės paviršiuje, tuomet detalė yra patalpinama į metalo tirpalą, kur metalas yra nusodinamas ant lazeriu aktyvuotų vietų katalitiniu būdų. Metodo trūkumai yra, jog šiam metodui yra tinkami tik tam

tikri polimerai, turintys savyje laidžių priemaišų, tokį kaip metalai ar anglies nanovamzdeliai. Polimerai su laidžiomis priemaišomis, negali būti naudojami kai kuriose srityse, tokiose kaip didelio dažnio elektronikoje. Taip pat, naudojamas katalitinis dengimo metalu būdas yra gerokai lėtesnis, nei galvaninis dengimas. Padengti detalę katalitiniu būdų gali užtruktai nuo kelių valandų iki kelių dienų, priklausomai kokio storio metalo sluoksnui norima padengti, kai tuo tarpu galvaninis dengimas trunka nuo kelių minučių iki valandos. Kitas metodas tai lazeriu indukuotas perkėlimas (angl. *LIFT, laser-induced forward transfer*). Jo principas yra, jog plonas donorinės medžiagos sluoksnis yra pakabinamas virš detalės, ir tuomet lazeriu yra pernešama medžiaga nuo donoro ant detalės. Šis metodas yra gana sudėtingas, reikalaujantis daug precizikos, taip pat nėra duomenų jog jis būtų sekmingai pritaikytas ant trimačių paviršių. Kitas metodas – lazeriu-indukuota selektyvi paviršiaus aktyvacija (angl. *SSAIL, selective surface activation induced by laser*). Metodas sudarytas iš keleto žingsnių, pirma, elektros grandinės raštas lazeriu yra užrašomas detalės paviršiuje. Sekantis žingsnis – tai cheminė aktyvacija, ir galiausiai, bandinys yra patalpinamas į metalo tirpalą, kur lazerio paveiktos, aktyvuotos vietas yra padengiamos metalu, katalitiniu būdu. Metodo privalumas yra, jog jį galima naudoti ant bet kokios nelaidžios medžiagos, t. y. ne tik ant polimerų, bet ir ant stiklo ar keramikos. Trūkumas būtų tai, jog katalitinis dengimo būdas riboja dengimo spartą.

Mūsų tyrimo, kurio tikslas buvo sukurti lazeriu-asistuotą technologiją selektyviam elektrai laidžių takelių formavimui ant polimerinių paviršių galvaniniu būdu, pagrindiniai uždaviniai buvo atrasti lazerinės spinduliuotės parametrus, su kuriais pavyktų suformuoti laidų grafeno sluoksnį bei atrasti tinkamiausius parametrus lazeriu apdirbto bandinio galvaniniam dengimui įvairiais metalais. Eksperimento metu buvo naudojami trys skirtingi lazeriai, generuojantys ultravioletinę (355 nm), regimąją (532 nm), artimąją infraraudonąją (1064 nm) bei vidurinę infraraudonąją (10.6 μm) spinduliuotę. Naudoti lazeriai buvo impulsiniai, generuojantys nanosekundinės trukmės (10 ns) arba pikosekundinės trukmės impulsus (10 ps). Lazerinis bandinių apdirbimas buvo vykdomas naudojant įvairius būdus, tokius kaip apdirbimas fokusuotu spinduliu, išfokusuotu spinduliu ar apdirbimas azoto atmosferoje. Lazerinio apdirbimo metu buvo fabrikuojamos 10 x 20 mm dydžio stačiakampių matricos, kur kiekviename matricos eilutės sekanciame stačiakampyje pakeičiamas vienas parametras, o sekanciame stulpelyje – kitas parametras. Lazeriniame apdirbime naudotas dydis - apšvitos dozė, kuris nurodo sugertos šviesos kiekį. Jis buvo apskaičiuojamas dauginant energijos tankį iš impulsų skaičiaus per spindulio plotą. Energijos tankis apskaičiuojamas dalinant impulso energiją iš spindulio ploto bandinio

paviršiuje. Po lazerinio apdirbimo sekė bandinių paviršiaus varžos matavimai, atliekami keturių zondų metodu bei Ramano spektrų sudarymas ir analizė. Varžos matavimai buvo atliekami siekiant sužinoti kaip pasikeitė paviršiaus laidumas po lazerinio apdirbimo, kuo mažesnė varža, tuo didesnis laidumas. Iš Ramano spektrų buvo įvertinama susiformavusio grafeno kokybė. Ramano spektrai yra pagrindinis matavimo būdas siekiant charakterizuoti grafeną. Ramano smailių $I(2D)/I(G)$ ir $I(D)/I(G)$ intensyvumų santykis indikuoja grafeno kokybę. Kuo didesnis Ramano smailių $I(2D)/I(G)$ intensyvumų santykis ir kuo mažesnis $I(D)/I(G)$, tuo grafenas yra kokybiškesnis, t. y. grafenas sudarytas iš mažiau sluoksnių, ir Jame yra mažiau defektų. Kuomet $I(2D)/I(G)$ santykis yra ~ 0.5 , tuomet tai daugiasluoksnis grafenas, kuomet ~ 0.8 – tai kelių sluoksnių grafenas, kuomet ~ 1 – tai dviejų sluoksnių, o kuomet ~ 2 – tai vieno sluoksnio grafenas. Po Ramano spektrų analizės sekė bandinių galvaninis dengimas. Eksperimente buvo išbandytos įvairios galvaninio tirpalo sudėtys, dengimo trukmės, ir naudojami skirtinių elektrinės srovės tankiai. Dažniausiai bandiniai buvo dengiami variu, kadangi tai yra pagrindinis metalas, naudojamas elektronikoje bei itin geras elektros laidininkas. Tačiau taip pat buvo atliktas lazeriu apdirbtų bandinių dengimas sidabru, nikeliu, alavu, kobaltu bei cinku. Sidabras – geriausias elektros laidininkas, plačiai taikomas elektronikos prietaisuose. Nikelis dažnai naudojamas kaip pasluoksnis vario dengimui. Alavas, kobaltas ir cinkas naudojami siekiant padidinti kietumą, atsparumą korozijai ir kituose taikymuose. Taigi, mūsų eksperimentą galima būtų suskirstyti į tris dalis: lazerinį apdirbimą, Ramano spektrų analizę bei bandinių dengimą metalu.

Pradinėje tyrimo dalyje, bandiniai buvo apdirbtai sufokusuotu 1064 nm bangos ilgio lazerio spinduliu židinio plokštumoje, nanosekundiniu bei pikosekundiniu lazeriu. Naudotas apdirbimo greitis buvo 100 mm/s, impulsų pasikartojimo dažnis – 100 kHz, atstumas tarp fabrikuojamų linijų – 30 μm , spindulio diametras bandinio paviršiuje – 52 μm . Šie parametrai nebuvo keičiami, o apšvitos doze buvo variuojama keičiant lazerio galią nuo 1.25 iki 6 W, apdirbant tiek su nanosekundiniu, tiek su pikosekundiniu lazeriu. Varžos pokyčiai bandinių paviršiuje buvo pastebimi kuomet apšvitos dozė buvo didesnė nei 20.41 J/cm^2 apdirbant nanosekundiniu lazeriu bei didesnė nei 17.75 J/cm^2 po apdirbimo pikosekundiniu lazeriu. Ties šiomis vertėmis paviršinė poliimido varža pradėjo mažėti, paviršiuje pradėjo formuotis juodos spalvos struktūros – suodžiai. Mažiausia pasiekta paviršinė varža, apšviečiant bandinį su nanosekundiniu lazeriu apšvitos doze 184 J/cm^2 buvo $354 \Omega/\text{kv.}$, su pikosekundiniu lazeriu apšviečiant 130 J/cm^2 doze buvo $30 \Omega/\text{kv.}$ Pastebėta, jog bandiniai deformavosi po apdirbimo nanosekundiniu lazeriu

apšvitos doze, didesne kaip 118 J/cm^2 , todėl tolimesniuose tyrimuose buvo naudojamas tik pikosekundinis lazeris.

Sekančioje eksperimento dalyje buvo keičiama nebe lazerio galia, o bandinio atstumas iki lazerio židinio plokštumos nuo 0 iki 12 mm, t. y. bandinys kas kart buvo nuleidžiamas po atstumą, lygų 0.25 mm žemiau židinio plokštumos iki 12 mm. Visi kiti apdirbimo parametrai nebuvo keičiami. Didinant bandinio atstumą iki židinio plokštumos, mažėja spinduliuotės energijos tankis bandinio paviršiuje, tačiau keičiasi lazerio impulsų persiklojimas, dėl to kinta apšvitos trukmė ir poliimido paviršiaus temperatūra. Gauti rezultatai parodė, jog apdirbant poliimidą didelio intensyvumo spinduliuote, t. y. kai poliimidas yra lazerio židinio plokštumoje arba iki 3 mm žemiau jos, paviršiuje susiformuoja suodžiai, kurių varža buvo nuo $30 \Omega/\text{kv}$. (apdirbant židinio plokštumoje) iki $20 \text{ M}\Omega/\text{kv}$. (3 mm žemiau židinio plokštumos). Apdirbus poliimidą nuo 3.25 mm iki 4.75 mm atstumu žemiau židinio plokštumos, vietomis susiformavo pilkos spalvos struktūros, kurių varža buvo $70\text{-}80 \Omega/\text{kv}$. Apdirbus bandinius, kuomet jie buvo padėti nuo 5 iki 12 mm atstumu žemiau židinio plokštumos, apšvitos doze nuo 10.76 J/cm^2 (5 mm žemiau židinio plokštumos) iki 4.42 J/cm^2 (12 mm žemiau židinio plokštumos), susiformavo grafeno sluoksnis, kurio paviršinė varža buvo $8 \Omega/\text{kv}$. Padarius bandinių Ramano spektrus, geriausias rezultatas buvo gautas kuomet bandinys buvo apdirbtas lazeriu, kai jis buvo padėtas 7 mm atstumu žemiau židinio plokštumos, apdirbus jį 7.34 J/cm^2 apšvitos doze. Ramano smailių $I(2D)/I(G)$ bei $I(D)/I(G)$ intensyvumų santykiai buvo atitinkamai 0.4 ir 0.1.

Toliau buvo atliktas poliimido apdirbimas nefokusuotu spinduliu naudojant ultravioletinę (355 nm) bei regimojo spekto diapazono spinduliuotę (532 nm). Tikslas buvo suprasti, kaip kiekvienas bangos ilgis daro įtaką grafeno formavimuisi. Ultravioletinio lazerio fotonų energijos pakanka tiesiogiai nutraukti poliimido tarp atominius ryšius, kadangi anglies atomų C-C jungties energija yra apytiksliai lygo fotono energijai, atitinkančiai 355 nm bangos ilgį. Kita vertus, kai naudojama infraraudonoji spinduliuotė, fotonų energija yra per maža, kad tiesiogiai būtų nutraukti cheminiai ryšiai, todėl šiuo atveju vyrauja šiluminiai procesai. Apdirbant poliimidą regimojo spekto spinduliuote (532 nm) gali pasireikšti abu atvejai. Apdirbus poliimidą nefokusuotu spinduliu, grafenas susiformavo poliimido paviršiuje kuomet apšvitos dozė buvo nuo 2.1 J/cm^2 iki 14.8 J/cm^2 apdirbant su 355 nm bangos ilgiu, bei nuo 3.2 J/cm^2 iki 14 J/cm^2 apdirbant 532 nm bangos ilgiu. Mažiausia pasiekta varža, apdirbant su 355 nm buvo $18 \Omega/\text{kv}$., o su 532 nm – $13 \Omega/\text{kv}$. Grafeno, suformuoto naudojant 355 nm ar 532 nm spinduliuotę, paviršiaus morfologija skyrėsi nuo grafeno, suformuoto su 1064 nm bangos ilgio

spinduliuote. Su 1064 nm suformuotas grafeno paviršius buvo labai lygus, tačiau nestipriai prikibės prie polimero pagrindo. Po kelių bandinio palankstymų, grafenas nukrisdavo. Tuo tarpu, grafenas, suformuotas naudojant 355 nm ar 532 nm spinduliuotę, buvo stipriai prikibės prie polimero, tačiau turėjo aukštesnę varžą. Ramano smailių I(2D)/I(G) bei I(D)/I(G) intensyvumų santykiai apdirbus bandinius atitinkamai su 355 nm ir 532 nm spinduliuote buvo 0.5 ir 1.05 bei 0.65 ir 0.92.

Kitame eksperimento etape poliimido bandiniai buvo apdirbti CO_2 lazeriu, generuojančiu 10.6 μm bangos ilgio spinduliuotę su išfokusuotu spinduliu. Geriausias pasiektas rezultatas buvo gautas, kuomet bandinys buvo padėtas 9 mm žemiau židinio plokšumos, apdirbant 8.6 J/cm^2 apšvitos doze. Susiformavusio grafeno varža buvo $7 \Omega/\text{kv}$. Ramano smailių intensyvumų santykiai 0.63 ir 0.57.

Kokybiškiausias grafenas buvo gautas, apdirbant poliimidą išfokusuotu 1064 nm spinduliu, kuomet poliimidas buvo patalpintas azoto kameroje. Apdirbant inertinių dujų aplinkoje, kuomet nėra deguonies, poliimidas mažiau dega ir oksiduoja, ir labiau yra linkęs transformuotis į grafeną. Mažiausia varža buvo pasiekta apdirbus poliimidą 7.3 J/cm^2 apšvitos doze, kuomet azoto kamera buvo nuleista 7 mm žemiau lazerio židinio plokšumos. Susiformavusio grafeno sluoksnio varža buvo mažiausia mūsų eksperimente – $5 \Omega/\text{kv}$, o Ramano smailių intensyvumų santykis I(2D)/I(G) bei I(D)/I(G) – 0.81 ir 0.46. Šis rezultatas indikuoja, jog tai yra kelių sluoksnų grafenas.

Sekančioje tyrimo dalyje buvo atliktas šilumos laidumo modeliavimas naudojant COMSOL Multiphysics programinę įrangą. Buvo simuliuojamas 355 nm, 532 nm, 1064 nm bei 10.6 μm impulsinės lazerinės spinduliuotės sąveika su 127 μm storio poliimido juosta. Simuliacija buvo skirta gausiniams pluoštai, darant prielaidą, jog 80% spinduliuotės buvo sugerta per tiesinę sugertį. Simuliacija parodė, jog norint suformuoti žemos paviršinės varžos grafeną, poliimido paviršių reikia pakaitinti 1000 K temperatūroje laiko tarpą, lygų 1.4 ms.

Paskutinėje mūsų tyrimo dalyje, sekė bandinių dengimas metalais galvaniniu būdu. Poliimido bandiniai, su suformuotu $10 \times 20 \text{ mm}$ dydžio stačiakampio formos įvairaus laidumo grafeno sluoksniu buvo nardinami į galvaninio nusodinimo tirpalą. Galvaniniam dengimui buvo reikalingas išorinis elektros srovės šaltinis. Anodo gnybtas buvo prikabinamas prie panardinto į metalo tirpalą, dengiamo bandinio, o katodas prikabinamas prie panardinto į tirpalą metalo, kuriuo norima padengti (pavyzdžiui, prie vario strypo). Naudotas dengimo srovės tankis buvo nuo 4 iki 20 mA/cm^2 , prie tokio srovės tankio, dengimo sparta buvo $0.2\text{--}0.5 \mu\text{m/min}$. Dengimo trukmė buvo nuo 10 iki 60 minučių, o siekiant išgauti tolygų bandinio padengimą, buvo

naudojamas tirpalo maišymas 550 apsisukimų per minutę greičiu. Dengimui variu, tirpalas buvo sudarytas iš vario sulfato (CuSO_4), sieros rūgšties (H_2SO_4) ir vandens (H_2O). Dengimas pavyko ant bandinių, kurių paviršinė varža buvo mažesnė nei $10 \text{ k}\Omega/\text{kv.}$, tačiau ant bandinių, kurių varža didesnė nei $100 \text{ }\Omega/\text{kv.}$, dengimas nebuvo tolygus – storesnis sluoksnis vario padengė sritį aplink srovės šaltinio gnybtą. Tolygus viso paviršiaus dengimas pavyko tik ant bandinių, kurių varža buvo mažesnė nei $100 \text{ }\Omega/\text{kv.}$ Dengimo sparta tiesiogiai priklausė nuo lazeriu suformuotos struktūros paviršinės varžos. Sparčiausiai dengėsi bandiniai su mažesne paviršine varža. Ploniausias sluoksnis, kuriuo pavyko tolygiai padengti variu $13 \text{ }\Omega/\text{kv.}$ varžos grafeno sluoksnį buvo $3 \text{ }\mu\text{m}$. Taip pat, lazeriu suformuoto laidaus sluoksnio dengimas buvo atliktas ir dengiant kitais metalais. Ant $13 \text{ }\Omega/\text{kv.}$ varžos grafeno sluoksnio pavyko tolygiai padengti ne mažesnio storio kaip: $9 \text{ }\mu\text{m}$ sidabro sluoksnį, $1 \text{ }\mu\text{m}$ nikelio, $7 \text{ }\mu\text{m}$ alavo, $2 \text{ }\mu\text{m}$ kobalto arba $10 \text{ }\mu\text{m}$ cinko sluoksnį.

Taigi, apibendrinus disertaciją galima būtų daryti išvadą, jog lazeriu suformuotas grafenas yra tinkamas galvaniniam dengimui metalu ir ši, lazeriu asistuota technologija, galėtų būti pritaikyta elektronikos pramonėje. Eksperimento metu buvo pademonstruota, jog lazeriu formuojamo grafeno kokybė gali būti kontroliuojama, keičiant lazerinės spinduliuotės parametrus. Norint suformuoti grafeną poliimido paviršiuje, jo paviršių reikia pakaitinti 1000 K laiko tarpą ne mažesnį nei 1 ms . Mažiausia grafeno paviršinė varža gauta apdirbus poliimidą, patalpintą azoto kameroje su 1064 nm bangos ilgio spinduliuote, ji lygi $5 \text{ }\Omega/\text{kv.}$ Eksperimento metu rasta koreliacija tarp paviršinės varžos ir Ramano spektrų smailių $I(2D)/I(G)$ ir $I(D)/I(G)$. Mažesnė varža indikuoja didesnį $I(2D)/I(G)$ ir mažesnį $I(D)/I(G)$ santykį. Taigi, grafeno paviršinė varža galėtų būti parametras grafeno kokybei nustatyti. Grafeno dengimo metalu sparta ir minimalus storis priklauso ne tik nuo dengimo parametrų, bet ir nuo dengiamo metalo rūšies. Su vienais metalais galima padengti plonesniu sluoksniu, su kitais – storesniu. Tyrimų metu gauti duomenys buvo publikuoti dviejuose straipsniuose *Polymers* žurnale, taip pat pristatyti 4 tarptautinėse bei 3 Lietuvos konferencijose.

BIBLIOGRAPHY

1. Bachy, B. Experimental Investigation, Modeling, Simulation and Optimization of Molded Interconnect Devices (MID) Based on Laser Direct Structuring (LDS), (PhD thesis, Friedrich-Alexander-University Erlangen-Nuremberg) (2017).
2. Bohandy, J.; Kim, B. F.; Adrian, F. J. Metal Deposition from a Supported Metal Film Using an Excimer Laser. *J. Appl. Phys.* **60**(4), 1538–1539 (1986).
3. Ratautas, K.; Jagminienė, A.; Stankevičienė, I.; Sadauskas, M.; Norkus, E.; Račiukaitis, G. Evaluation and Optimisation of the SSAIL Method for Laser-Assisted Selective Electroless Copper Deposition on Dielectrics. *Results Phys.* **16**, 102943 (2020).
4. Fiodorov, V.; Ratautas, K.; Mockus, Z.; Trusovas, R.; Mikoliūnaitė, L.; Račiukaitis, G. Laser-assisted selective fabrication of copper traces on polymers by electroplating. *Polymers*, **14**(4), 781 (2022).
5. Augustyn, P.; Rytlewski, P.; Moraczewski, K.; Mazurkiewicz, A. A Review on the Direct Electroplating of Polymeric Materials. *J. Mater. Sci.* **56**(27), 14881–14899 (2021).
6. Islam, A.; Hansen, H. N.; Tang, P. T. Direct Electroplating of Plastic for Advanced Electrical Applications. *CIRP Ann.* **66**(1), 209–212 (2017).
7. Geim, A. K.; Novoselov, K. S. The Rise of Graphene. *Nat. Mater.* **6**, 183–191 (2007).
8. Jian, M.; Wang, C.; Wang, Q.; Wang, H.; Xia, K.; Yin, Z.; Zhang, M.; Liang, X.; Zhang, Y. Advanced Carbon Materials for Flexible and Wearable Sensors. *Sci. China Mater.* **60**(11), 1026–1062 (2017).
9. Avouris, P.; Dimitrakopoulos, C. Graphene: Synthesis and Applications. *Mater. Today* **15**(3), 86–97 (2012).
10. Zhu, Y.; Murali, S.; Cai, W.; Li, X.; Suk, J. W.; Potts, J. R.; Ruoff, R. S. Graphene and Graphene Oxide: Synthesis, Properties, and Applications. *Adv. Mater.* **22**(35), 3906–3924 (2010).
11. Luong, D. X., Laser Induced Graphene Nanomaterials and Applications, (PhD thesis, Rice University) (2017).
12. Sokolov, D. A.; Shepperd, K. R.; Orlando, T. M. Formation of Graphene Features from Direct Laser-Induced Reduction of Graphite Oxide. *J. Phys. Chem. Lett.* **1**(18), 2633–2636 (2010).
13. Marengo, M.; Marinaro, G.; Kosel, J. Flexible Temperature and Flow Sensor from Laser-Induced Graphene. *Proc. IEEE Sensors* 1–3 (2017).
14. Lithium-ion, H. A. Photothermally Reduced Graphene as Batteries. *ACS Nano* **6**, 7867–7878 (2012).

15. Petridis, C.; Lin, Y. H.; Savva, K.; Eda, G.; Kymakis, E.; Anthopoulos, T. D.; Stratakis, E. Post-Fabrication, in Situ Laser Reduction of Graphene Oxide Devices. *Appl. Phys. Lett.* **102**(9), 093115 (2013).
16. Rahimi, R.; Ochoa, M.; Yu, W.; Ziaie, B. Highly Stretchable and Sensitive Unidirectional Strain Sensor via Laser Carbonization. *ACS Appl. Mater. Interfaces* **7**(8), 4463–4470 (2015).
17. Celiešiute, R.; Trusovas, R.; Niaura, G.; Švedas, V.; Račiukaitis, G.; Ružele, Ž.; Pauliukaite, R. Influence of the Laser Irradiation on the Electrochemical and Spectroscopic Peculiarities of Graphene-Chitosan Composite Film. *Electrochim. Acta* **132**, 265–276 (2014).
18. Trusovas, R.; Ratautas, K.; Račiukaitis, G.; Niaura, G. Graphene Layer Formation in Pinewood by Nanosecond and Picosecond Laser Irradiation. *Appl. Surf. Sci.* **471**, 154–161 (2019).
19. Ye, R.; James, D. K.; Tour, J. M. Laser-Induced Graphene. *Acc. Chem. Res.* **51**(7), 1609–1620 (2018).
20. Khan, W.; Sharma, R.; Saini, P. Carbon Nanotube-Based Polymer Composites: Synthesis, Properties and Applications. 1–46, InTech (2016).
21. Rahimi, R.; Ochoa, M.; Yu, W.; Ziaie, B. A Highly Stretchable PH Sensor Array Using Elastomer-Embedded Laser Carbonized Patterns. 18th Int. Conf. Solid-State Sensors, Actuators Microsystems, pp. 1897–1900, (2015 June).
22. Luo, J.; Duan, X.; Chen, Z.; Ruan, X.; Yao, Y.; Liu, T. A Laser-Fabricated Nanometer-Thick Carbon Film and Its Strain-Engineering for Achieving Ultrahigh Piezoresistive Sensitivity. *J. Mater. Chem. C* **7**(36), 11276–11284 (2019).
23. Rahimi, R.; Ochoa, M.; Ziaie, B. Direct Laser Writing of Porous-Carbon/Silver Nanocomposite for Flexible Electronics. *ACS Appl. Mater. Interfaces* **8**(26), 16907–16913 (2016).
24. Ruan, X.; Wang, R.; Luo, J.; Yao, Y.; Liu, T. Experimental and Modeling Study of CO₂ Laser Writing Induced Polyimide Carbonization Process. *Mater. Des.* **160**, 1168–1177 (2018).
25. Luo, J.; Yao, Y.; Duan, X.; Liu, T. Force, and Humidity Dual Sensors Fabricated by Laser Writing on Polyimide/Paper Bilayer Structure for Pulse and Respiration Monitoring. *J. Mater. Chem. C* **6**(17), 4727–4736 (2018).
26. In, J. Bin.; Hsia, B.; Yoo, J. H.; Hyun, S.; Carraro, C.; Maboudian, R.; Grigoropoulos, C. P. Facile Fabrication of Flexible All Solid-State Micro-Supercapacitor by Direct Laser Writing of Porous Carbon in Polyimide. *Carbon* **83**, 144–151 (2015).
27. Cheng, C.; Wang, S.; Wu, J.; Yu, Y.; Li, R.; Eda, S.; Chen, J.; Feng, G.;

Lawrie, B.; Hu, A. Bisphenol A Sensors on Polyimide Fabricated by Laser Direct Writing for Onsite River Water Monitoring at Attomolar Concentration. *ACS Appl. Mater. Interfaces* **8**(28), 17784–17792 (2016).

28. Liu, W.; Huang, Y.; Peng, Y.; Walczak, M.; Wang, D.; Chen, Q.; Liu, Z.; Li, L. Stable Wearable Strain Sensors on Textiles by Direct Laser Writing of Graphene. *ACS Appl. Nano Mater.* **3**(1), 283–293 (2020).

29. Crompton, T. R. Polymer reference book. iSmithers Rapra Publishing (2006).

30. Shrivastava, A. Introduction to plastics engineering. William Andrew (2018).

31. Young, R. J., Lovell, P. A. Introduction to polymers. CRC press. (2011).

32. Biron, M. Thermosets and composites. Elsevier (2003).

33. Awuzie, C. I. Conducting polymers. *Materials Today: Proceedings* **4**(4), 5721-5726 (2017).

34. Szeluga, U.; Kumanek, B.; Trzebicka, B. Synergy in hybrid polymer/nanocarbon composites. A review. *Composites Part A: Applied Science and Manufacturing*, **73**, 204-231 (2015).

35. Hussain, A. R. J. A study of effects of filler content on processing and properties of thermally conductive plastics, (PhD thesis, University of Massachusetts Lowell) (2016).

36. Zaaba, N. F.; Ismail, H.; Saeed, A. M. A Review: Metal Filled Thermoplastic Composites. *Polymer-Plastics Technology and Materials*, **60**(10), 1033-1050 (2021).

37. Al Christopher, C.; da Silva, I. G.; Pangilinan, K. D.; Chen, Q.; Caldona, E. B.; Advincula, R. C. High performance polymers for oil and gas applications. *Reactive and Functional Polymers* **162**, 104878 (2021).

38. Fink, J. K. High performance polymers. William Andrew (2014).

39. Takacs, C. J.; Treat, N. D.; Krämer, S.; Chen, Z.; Facchetti, A.; Chabiny, M. L.; Heeger, A. J. Remarkable order of a high-performance polymer. *Nano letters* **13**(6), 2522-2527 (2013).

40. Mark, H. F.; Bikales, N. M.; Overberger, C. G.; Menges, G.; Kroschwitz, J. I. *Encyclopedia of Polymer Science and Engineering*, 2nd ed., Volume 8, Wiley Interscience (1987).

41. Mishra, M., *Encyclopedia of Polymer Applications*, Volume 3. CRC Press (2018).

42. Mittal, K. L., Ed. *Polyimides: Synthesis, Characterization and Applications*. Volume 1, Springer (2013).

43. Hrabovsky, J.; Liberatore, C.; Mirza, I.; Sladek, J.; Beranek, J.; Bulgakov, A. V.; Bulgakova, N. M. Surface structuring of Kapton polyimide with femtosecond and picosecond IR laser pulses. *Interfacial Phenomena and*

Heat Transfer, **7**(2) (2019).

- 44. Ghosh, M. K. Polyimides Fundamentals and Applications. CRC Press (2018).
- 45. Woo, H. G.; Li, H.; Ha, C. S.; Mathews, A. S. Polyimides and high-performance organic polymers. Advanced Functional Materials, 1-36, (2011).
- 46. Maurya, P. M. Review of Current Developments on Natural and Synthetic Biodegradable Polymers and Their Biomedical Applications. South Asian Research Journal of Nursing and Healthcare. **1**(2) (2019).
- 47. Balaji, A. B.; Pakalapati, H.; Khalid, M.; Walvekar, R.; Siddiqui, H. Natural and synthetic biocompatible and biodegradable polymers. Biodegradable and biocompatible polymer composites **286**, 3-32 (2018).
- 48. Oganov, A. R.; Hemley, R. J.; Hazen, R. M.; Jones, A. P. Structure, bonding, and mineralogy of carbon at extreme conditions. Reviews in Mineralogy and Geochemistry **75**(1), 47-77 (2013).
- 49. Karthik, P. S.; Himaja, A. L.; Singh, S. P. Carbon-allotropes: synthesis methods, applications and future perspectives. Carbon Letters **15**(4), 219-237 (2014).
- 50. Ghany, N. A. A.; Elsherif, S. A.; Handal, H. T. Revolution of Graphene for different applications: State-of-the-art. Surfaces and Interfaces **9**, 93-106 (2017).
- 51. Rudrapati, R. Graphene: Fabrication methods, properties, and applications in modern industries (Vol. 1). London, UK: IntechOpen (2020).
- 52. Randviir, E. P.; Brownson, D. A.; Banks, C. E. A decade of graphene research: production, applications and outlook. Materials Today **17**(9), 426-432 (2014).
- 53. Zhen, Z.; Zhu, H. Structure and properties of graphene. In Graphene (pp. 1-12). Academic Press (2018).
- 54. Abergel, D. S. L.; Apalkov, V.; Berashevich, J.; Ziegler, K.; Chakraborty, T. Properties of graphene: a theoretical perspective. Advances in Physics **59**(4), 261-482 (2010).
- 55. Cai, X.; Lai, L.; Shen, Z.; Lin, J. Graphene and graphene-based composites as Li-ion battery electrode materials and their application in full cells. Journal of Materials Chemistry A **5**(30), 15423-15446 (2017).
- 56. Presumido, P. H.; Primo, A.; Vilar, V. J.; Garcia, H. Large area continuous multilayer graphene membrane for water desalination. Chemical Engineering Journal **413**, 127510 (2021).
- 57. Lemme, M. C.; Echtermeyer, T. J.; Baus, M.; Szafranek, B. N.; Bolten, J.;

Schmidt, M.; Wahlbrink, T.; Kurz, H. Mobility in graphene double gate field effect transistors. *Solid-State Electronics*, **52**(4) 514-518 (2008).

58. Lemme, M. C. Current status of graphene transistors. *Solid State Phenomena* **156**, 499-509 (2010).

59. Das, S.; Sudhagar, P.; Kang, Y. S.; Choi, W. Graphene synthesis and application for solar cells. *Journal of Materials Research* **29**(3), 299-319 (2014).

60. Zhou, X.; Liang, F. Application of graphene/graphene oxide in biomedicine and biotechnology. *Current Medicinal Chemistry* **21**(7), 855-869 (2014).

61. Zhang, H.; Gruener, G.; Zhao, Y. Recent advancements of graphene in biomedicine. *Journal of Materials Chemistry B* **1**(20), 2542-2567 (2013).

62. Mbayachi, V. B.; Ndayiragije, E.; Sammani, T.; Taj, S.; Mbuta, E. R. Graphene synthesis, characterization and its applications: A review. *Results in Chemistry* **3**, 100163 (2021).

63. Jayasena, B.; Subbiah, S. A novel mechanical cleavage method for synthesizing few-layer graphene. *Nanoscale Research Letters* **6**, 1-7 (2011).

64. Annett, J.; Cross, G. L. Self-assembly of graphene ribbons by spontaneous self-tearing and peeling from a substrate. *Nature* **535**(7611), 271-275 (2016).

65. Yi, M.; Shen, Z. A review on mechanical exfoliation for the scalable production of graphene. *Journal of Materials Chemistry A* **3**(22), 11700-11715 (2015).

66. Dash, P.; Dash, T.; Rout, T. K.; Sahu, A. K.; Biswal, S. K.; Mishra, B. K. Preparation of graphene oxide by dry planetary ball milling process from natural graphite. *RSC advances* **6**(15), 12657-12668 (2016).

67. Campos-Delgado, J.; Botello-Méndez, A. R.; Algara-Siller, G.; Hackens, B.; Pardoén, T.; Kaiser, U.; Dresselhaus, M. S.; Charlier, J. C.; Raskin, J. P. CVD synthesis of mono-and few-layer graphene using alcohols at low hydrogen concentration and atmospheric pressure. *Chemical Physics Letters* **584**, 142-146 (2013).

68. Min, B. H.; Kim, D. W.; Kim, K. H.; Choi, H. O.; Jang, S. W.; Jung, H. T. Bulk scale growth of CVD graphene on Ni nanowire foams for a highly dense and elastic 3D conducting electrode. *Carbon* **80**, 446-452 (2014).

69. Kataria, S.; Wagner, S.; Ruhkopf, J.; Gahoi, A.; Pandey, H.; Bornemann, R.; Vaziri, S.; Smith, A. D.; Ostling, M.; Lemme, M. C. Chemical vapor deposited graphene: From synthesis to applications. *physica status solidi (a)* **211**(11), 2439-2449 (2014).

70. Mishra, N.; Boeckl, J.; Motta, N.; Iacopi, F. Graphene growth on silicon

carbide: A review. *physica status solidi (a)* **213**(9), 2277-2289 (2016).

- 71. Tetlow, H.; De Boer, J. P.; Ford, I. J.; Vvedensky, D. D.; Coraux, J.; Kantorovich, L. Growth of epitaxial graphene: Theory and experiment. *Physics Reports* **542**(3), 195-295 (2014).
- 72. Yang, W.; Chen, G.; Shi, Z.; Liu, C. C.; Zhang, L.; Xie, G.; Cheng, M.; Wang, D.; Yang, R.; Shi, D.; Watanabe, K.; Taniguchi, T.; Yao, Y.; Zhang, Y.; Zhang, G. Epitaxial growth of single-domain graphene on hexagonal boron nitride. *Nature Materials* **12**(9), 792-797 (2013).
- 73. Chua, C. K.; Pumera, M. Chemical reduction of graphene oxide: a synthetic chemistry viewpoint. *Chemical Society Reviews* **43**(1), 291-312 (2014).
- 74. De Silva, K. K. H.; Huang, H. H.; Joshi, R. K.; Yoshimura, M. Chemical reduction of graphene oxide using green reductants. *Carbon* **119**, 190-199 (2017).
- 75. Pham, V. H.; Pham, H. D.; Dang, T. T.; Hur, S. H.; Kim, E. J.; Kong, B. S.; Chung, J. S. Chemical reduction of an aqueous suspension of graphene oxide by nascent hydrogen. *Journal of Materials Chemistry* **22**(21), 10530-10536 (2012).
- 76. Lin, J.; Peng, Z.; Liu, Y.; Ruiz-Zepeda, F.; Ye, R.; Samuel, E. L.; Yacaman, M. J.; Yakobson, B. O; Tour, J. M. Laser-induced porous graphene films from commercial polymers. *Nature Communications* **5**(1), 5714 (2014).
- 77. Huang, L.; Su, J.; Song, Y.; Ye, R. Laser-induced graphene: En route to smart sensing. *Nano-micro letters* **12**, 1-17 (2020).
- 78. Tiliakos, A.; Ceaus, C.; Iordache, S. M.; Vasile, E.; Stamatin, I. Morphic transitions of nanocarbons via laser pyrolysis of polyimide films. *Journal of Analytical and Applied Pyrolysis* **121**, 275-286 (2016).
- 79. Carvalho, A. F.; Fernandes, A. J.; Leitão, C.; Deuermeier, J.; Marques, A. C.; Martins, R.; Fortunato, E.; Costa, F. M. Laser-induced graphene strain sensors produced by ultraviolet irradiation of polyimide. *Advanced Functional Materials* **28**(52), 1805271 (2018).
- 80. Santos, N. F.; Pereira, S. O.; Moreira, A.; Girão, A. V.; Carvalho, A. F.; Fernandes, A. J.; Costa, F. M. IR and UV Laser-Induced Graphene: Application as Dopamine Electrochemical Sensors. *Advanced Materials Technologies* **6**(6), 2100007 (2021).
- 81. Wang, L.; Wang, Z.; Bakhtiyari, A. N.; Zheng, H. A comparative study of laser-induced graphene by CO₂ infrared laser and 355 nm ultraviolet (UV) laser. *Micromachines* **11**(12), 1094 (2020).
- 82. Zhang, Z.; Song, M.; Hao, J.; Wu, K.; Li, C.; Hu, C. Visible light laser-induced graphene from phenolic resin: A new approach for directly writing graphene-based electrochemical devices on various substrates.

Carbon **127**, 287-296 (2018).

- 83. Schaffer, C. B.; Brodeur, A.; Mazur, E. Laser-induced breakdown and damage in bulk transparent materials induced by tightly focused femtosecond laser pulses. *Measurement Science and Technology*. **12**(11), 1784 (2011).
- 84. Kunizhev, B. I.; Torshkhoeva, Z. S.; Zhelikhazhev, R. N.; Starov, A. V. Destruction of polymers under the action of laser radiation. In *IOP Conference Series: Materials Science and Engineering* **1083**, 1, 012040 (2011).
- 85. Rebollar, E.; Castillejo, M. Laser interactions with organic/polymer materials. *Handbook of Laser Micro-and Nano-Engineering*, 1-49, Springer (2020).
- 86. Luo, Y. R. *Comprehensive handbook of chemical bond energies*. CRC press. (2007).
- 87. Keller, O. *Light-The physics of the photon*. CRC press. (2014).
- 88. Butkutė, A.; Jonušauskas, L. 3D manufacturing of glass microstructures using femtosecond laser. *Micromachines* **12**(5), 499 (2021).
- 89. Scott, A. *Encyclopedia of nonlinear science*. Routledge (2006).
- 90. Derrien, T. J. Y.; Levy, Y.; Bulgakova, N. M. Insights into laser-matter interaction from inside: Wealth of processes, multiplicity of mechanisms and possible roadmaps for energy localization. In *Ultrafast Laser Nanostructuring: The Pursuit of Extreme Scales* (pp. 3-64). Cham: Springer International Publishing (2023).
- 91. Franke, J. *Three-dimensional molded interconnect devices (3D-MID): Materials, manufacturing, assembly and applications for injection molded circuit carriers*. Carl Hanser Verlag GmbH Co KG (2014).
- 92. Yang, J. U.; Cho, J. H.; Yoo, M. J. Selective metallization on copper aluminate composite via laser direct structuring technology. *Composites Part B: Engineering* **110**, 361-367 (2017).
- 93. Bachy, B.; Franke, J. Experimental investigation and optimization for the effective parameters in the laser direct structuring process. *Journal of Laser Micro Nanoengineering* **10**(2), 202 (2015).
- 94. Heininger, N.; John, W.; Boßler, H. J. Manufacturing of molded interconnect devices from prototyping to mass production with laser direct structuring. In *International Congress MID* (pp. 1-20) (2004).
- 95. Cihangir, A.; Sonnerat, F.; GIANESELLO, F.; Gloria, D.; Luxey, C. Antenna solutions for 4G smartphones in laser direct structuring technology. *Radioengineering* **25**(3), 419-428 (2016).
- 96. Gath, C.; Drummer, D. Circuit board application to additive manufactured components by laser-direct-structuring. In *2016 12th International*

Congress Molded Interconnect Devices (MID) (pp. 1-6). IEEE (2016).

- 97. Ratautas, K.; Andrulevičius, M.; Jagminienė, A.; Stankevičienė, I.; Norkus, E.; Račiukaitis, G. Laser-assisted selective copper deposition on commercial PA6 by catalytic electroless plating—Process and activation mechanism. *Applied Surface Science*, **470**, 405-410 (2019).
- 98. Kobayashi, M. Development of New Molded Interconnect Device-- Innovative MID technology to realize a micro device. IEICE Technical Report; IEICE Tech. Rep., **107**(46), 13-16 (2007).
- 99. Serra, P.; Piqué, A. Laser-induced forward transfer: fundamentals and applications. *Advanced Materials Technologies* **4**(1), 1800099 (2019).
- 100. Willis, D. A.; Grosu, V. Microdroplet deposition by laser-induced forward transfer. *Applied Physics Letters* **86**(24) (2005).
- 101. Colina, M.; Serra, P.; Fernández-Pradas, J. M.; Sevilla, L.; Morenza, J. L. DNA deposition through laser induced forward transfer. *Biosensors and Bioelectronics* **20**(8), 1638-1642 (2005).
- 102. Delaporte, P.; Alloncle, A. P. Laser-induced forward transfer: A high resolution additive manufacturing technology. *Optics & Laser Technology* **78**, 33-41 (2016).
- 103. Morales, M.; Munoz-Martin, D.; Marquez, A.; Lauzurica, S.; Molpeceres, C. Laser-induced forward transfer techniques and applications. *Advances in Laser Materials Processing*, Elsevier, 339-379 (2018).
- 104. Zhang, J.; Feng, J.; Jia, L.; Zhang, H.; Zhang, G.; Sun, S.; Zhou, T. Laser-induced selective metallization on polymer substrates using organocopper for portable electronics. *ACS applied materials & interfaces* **11**(14), 13714-13723 (2019).
- 105. Zhang, Y.; Hansen, H. N.; De Grave, A.; Tang, P. T.; Nielsen, J. S. Selective metallization of polymers using laser induced surface activation (LISA)—characterization and optimization of porous surface topography. *The International Journal of Advanced Manufacturing Technology*, **55**, 573-580. (2011).
- 106. Rytlewski, P.; Jagodziński, B.; Malinowski, R.; Budner, B.; Moraczewski, K.; Wojciechowska, A.; Augustyn, P. Laser-induced surface activation and electroless metallization of polyurethane coating containing copper (II) L-tyrosine. *Applied Surface Science* **505**, 144429 (2020).
- 107. Kordás, K.; Békési, J.; Vajtai, R.; Nánai, L.; Leppävuori, S.; Uusimäki, A.; Moilanen, P. Laser-assisted metal deposition from liquid-phase precursors on polymers. *Applied Surface Science* **172**(1-2), 178-189 (2001).
- 108. Manshina, A.; Povolotskiy, A.; Ivanova, T.; Kurochkin, A.; Tver'yanovich, Y.; Kim, D.; Kwon, S. C. Laser-assisted metal deposition

from CuSO₄-based electrolyte solution. *Laser Physics Letters* **4**(2), 163 (2006).

- 109. Van der Putten, A. M.; Jacobs, J. W.; Rikken, J. M.; de Kort, K. G. Laser-induced metal deposition from the liquid phase. In *Laser Assisted Processing* (Vol. 1022, pp. 71-76). SPIE (1989).
- 110. Richard, C. *Understanding Semiconductors: A Technical Guide for Non-Technical People* (pp. 57-80). Berkeley, CA: Apress (2022).
- 111. Qin, D.; Xia, Y.; Black, A. J.; Whitesides, G. M. Photolithography with transparent reflective photomasks. *Journal of Vacuum Science & Technology B: Microelectronics and Nanometer Structures Processing, Measurement, and Phenomena* **16**(1), 98-103 (1998).
- 112. Wilkinson, N. J.; Smith, M. A.; Kay, R. W.; Harris, R. A. A review of aerosol jet printing—a non-traditional hybrid process for micro-manufacturing. *The International Journal of Advanced Manufacturing Technology*, **105**, 4599-4619 (2019).
- 113. Secor, E. B. Principles of aerosol jet printing. *Flexible and Printed Electronics*, **3**(3), 035002 (2018).
- 114. Singh, M.; Haverinen, H. M.; Dhagat, P.; Jabbour, G. E. Inkjet printing—process and its applications. *Advanced Materials* **22**(6), 673-685 (2010).
- 115. Huang, Y.; Wu, H.; Xiao, L.; Duan, Y.; Zhu, H.; Bian, J.; Ye, D; Yin, Z. Assembly and applications of 3D conformal electronics on curvilinear surfaces. *Materials Horizons*, **6**(4), 642-683 (2019).
- 116. Calvert, P. Inkjet printing for materials and devices. *Chemistry of materials* **13**(10), 3299-3305 (2001).
- 117. Unnikrishnan, D. Mid technology potential for RF passive components and antennas, (PHD thesis, Université Grenoble Alpes) (2015).
- 118. Kim, G. W.; Kim, Y. J.; Kim, H. K. Review of brush painting for cost-efficient paintable electronics. *Applied Science and Convergence Technology* **30**(1), 1-5 (2021).
- 119. Jin, I. S.; Lee, W.; Lim, S. J.; Ko, J. H.; Jung, J. W. Ultra-flexible, stretchable, highly conductive and multi-functional textiles enabled by brush-painted PEDOT: PSS. *Smart Materials and Structures* **29**(9), 095002 (2020).
- 120. Jeong, J. A.; Jeon, Y. J.; Kim, S. S.; Kim, B. K.; Chung, K. B.; Kim, H. K. Simple brush-painting of Ti-doped In₂O₃ transparent conducting electrodes from nano-particle solution for organic solar cells. *Solar energy materials and solar cells* **122**, 241-250 (2014).
- 121. Wang, B.; Eberhardt, W.; Kück, H. Metal deposition on liquid crystal polymers for molded interconnect devices using physical vapor deposition. *Journal of Adhesion Science and Technology* **18**(8), 883-891

(2004).

- 122. Lackner, J. M.; Waldhauser, W.; Hartmann, P.; Bruckert, F.; Weidenhaupt, M.; Major, R.; Heim, D. Hemocompatibility of inorganic physical vapor deposition (PVD) coatings on thermoplastic polyurethane polymers. *Journal of Functional Biomaterials* **3**(2), 283-297 (2012).
- 123. Mattox, D. M. *Handbook of physical vapor deposition (PVD) processing*. William Andrew (2010).
- 124. Norman, J. A.; Perez, M.; Schulz, S. E.; Waechter, T. New precursors for CVD copper metallization. *Microelectronic Engineering* **85**(10), 2159-2163 (2008).
- 125. Kaloyeros, A. E.; Fury, M. A. Chemical vapor deposition of copper for multilevel metallization. *MRS Bulletin* **18**(6), 22-29 (1993).
- 126. Okinaka, Y.; Osaka, T. Electroless deposition processes: fundamentals and applications. *Advances in electrochemical science and engineering* **3**, 55-116 (2008).
- 127. Ghosh, S. Electroless copper deposition: A critical review. *Thin Solid Films* **669**, 641-658 (2019).
- 128. Djokić, S. S. Electroless deposition of metals and alloys. In *Modern aspects of electrochemistry* (pp. 51-133). Boston, MA: Springer US. (2002).
- 129. Schlesinger, M.; Paunovic, M. (Eds.). *Modern electroplating* (Vol. 52). John Wiley & Sons (2014).
- 130. Miura, S.; Honma, H. Advanced copper electroplating for application of electronics. *Surface and Coatings Technology* **169**, 91-95 (2003).
- 131. Augustyn, P.; Rytlewski, P.; Moraczewski, K.; Mazurkiewicz, A. A review on the direct electroplating of polymeric materials. *Journal of Materials Science* **56**(27), 14881-14899 (2021).
- 132. Osaka, T.; Komaba, S.; Momma, T. Conductive polymers: Electroplating of organic films. *Modern Electroplating* **5**, 421-432 (2010).
- 133. Swain, A.; Preparation of coated microtools for electrochemical machining applications, (PHD thesis, University of Nebraska-Lincoln) (2010).
- 134. Islam, A.; Hansen, H. N.; Tang, P. T. Direct electroplating of plastic for advanced electrical applications. *CIRP Annals* **66**(1), 209-212 (2017).
- 135. Bazzaoui, M.; Martins, J. I.; Bazzaoui, E. A.; Albourine, A. Environmentally friendly process for nickel electroplating of ABS. *Applied surface science* **258**(20), 7968-7975 (2012).
- 136. Angel, K.; Tsang, H. H.; Bedair, S. S.; Smith, G. L.; Lazarus, N. Selective electroplating of 3D printed parts. *Additive Manufacturing*, **20**, 164-172 (2018).

137. DuPont™ Kapton® HN datasheet, <https://www.dupont.com/content/dam/dupont/amer/us/en/ei-transformation/public/documents/en/EI-10206-Kapton-HN-Data-Sheet.pdf>, accessed 09/01/2024.

138. <https://www.materialdatacenter.com/ms/en/tradenames/Arboform/TECNARO+GmbH/ARBOFORM+F45+natur/0039a91b/4252>, accessed 12/08/2024.

139. Ratautas, K.; Gedvilas, M.; Stankevičiene, I.; Jagminienė, A.; Norkus, E.; Pira, N. L.; Sinopoli, S.; Račiukaitis, G. Laser-induced selective metallization of polypropylene doped with multiwall carbon nanotubes. *Applied Surface Science* **412**, 319-326 (2017).

140. Trusovas, R.; Ratautas, K.; Račiukaitis, G.; Barkauskas, J.; Stankevičienė, I.; Niaura, G.; Mažeikienė, R. Reduction of graphite oxide to graphene with laser irradiation. *Carbon*, **52**, 574-582 (2013).

141. Huh, S. H. Thermal reduction of graphene oxide. Physics and applications of graphene-experiments (pp. 73-90). Rijeka, Croatia: InTech, (2011).

142. Hristovski, I. R.; Herman, L. A.; Mitchell, M. E.; Lesack, N. I.; Reich, J.; Holzman, J. F. Manifestations of Laser-Induced Graphene under Ultraviolet Irradiation of Polyimide with Varied Optical Fluence. *Nanomaterials*, **12**(8), 1241 (2022).

143. Chyan, Y.; Ye, R.; Li, Y.; Singh, S. P.; Arnusch, C. J.; Tour, J. M. Laser-induced graphene by multiple lasing: toward electronics on cloth, paper, and food. *ACS nano*, **12**(3), 2176-2183 (2018).

144. Lee, J. U.; Ma, Y. W.; Jeong, S. Y.; Shin, B. S. Fabrication of UV laser-induced porous graphene patterns with nanospheres and their optical and electrical characteristics. *Materials*, **13**(18), 3930 (2020).

145. Santos, N. F.; Pereira, S. O.; Moreira, A.; Girão, A. V.; Carvalho, A. F.; Fernandes, A. J.; Costa, F. M. IR and UV Laser-Induced Graphene: Application as Dopamine Electrochemical Sensors. *Advanced Materials Technologies* **6**(6), 2100007 (2021).

146. Trusovas, R.; Raciukaitis, G.; Barkauskas, J.; Mazeikiene, R. Laser-induced graphite oxide/graphene transformation. *J. Laser MicroNanoeng.* **7**, 49 (2012).

147. Ye, R.; Chyan, Y.; Zhang, J.; Li, Y.; Han, X.; Kittrell, C.; Tour, J.M. Laser-induced graphene formation on wood. *Adv. Mater.* **29**, 1702211 (2017).

148. Nosrati, H.; Sarraf-Mamoory, R.; Karimi Behnagh, A.; Zolfaghari Emameh, R.; Aidun, A.; Le, D.Q.S.; Perez, M.C.; Bünger, C.E. Comparison of the effect of argon, hydrogen, and nitrogen gases on the reduced graphene oxide-hydroxyapatite nanocomposites characteristics. *BMC Chem.* **14**, 59 (2020).

149. Graf, D.; Molitor, F.; Ensslin, K.; Stampfer, C.; Jungen, A.; Hierold, C.; Wirtz, L. Raman mapping of a single-layer to double-layer graphene transition. *Eur. Phys. J. Spec. Top.* **148**, 171–176 (2007).

150. Jorio, A.; Ferreira, E.H.M.; Moutinho, M.V.O.; Stavale, F.; Achete, C.A.; Capaz, R.B. Measuring Disorder in Graphene with the G and D Bands. *Phys. Status Solidi Basic Res.* **247**, 2980–2982 (2010).

151. Sokolov, D. A.; Rouleau, C. M.; Geohegan, D. B.; Orlando, T. M. Excimer laser reduction and patterning of graphite oxide. *Carbon*, **53**, 81-89 (2013).

152. Kang, S.; Evans, C. C.; Shukla, S.; Reshef, O.; Mazur, E. Patterning and reduction of graphene oxide using femtosecond-laser irradiation. *Optics & Laser Technology*, **103**, 340-345 (2018).

153. Ye, R.; James, D. K.; Tour, J. M. Laser-induced graphene: from discovery to translation. *Advanced Materials*, **31**(1), 1803621 (2019).

154. Pérez-Mas, A. M.; Álvarez, P.; Campos, N.; Gómez, D.; Menéndez, R. Graphene patterning by nanosecond laser ablation: The effect of the substrate interaction with graphene. *Journal of Physics D: Applied Physics*, **49**(30), 305301 (2016).

155. Yoon, D.; Moon, H.; Cheong, H.; Choi, J.S.; Choi, J.A.; Park, B.H. Variations in the Raman Spectrum as a Function of the Number of Graphene Layers. *J. Korean Phys. Soc.* **55**, 1299–1303 (2009).

156. Crank, J.; Nicholson, P. A Practical Method for Numerical Evaluation of Solutions of Partial Differential Equations of the Heat-Conduction Type. *Proc. Cambr. Phil. Soc.* **43**, 50–67 (1947).

157. <https://refractiveindex.info/?shelf=other&book=Kapton&page=French>, accessed 17/09/2024.

158. https://refractiveindex.info/?shelf=other&book=Kapton&page=Brannon#google_vignette, accessed 19/01/2025.

159. <https://refractiveindex.info/?shelf=other&book=Kapton&page=French>, accessed 19/01/2025.

160. Fleming, J. W.; Weber, M. J.; Day, G. W.; Feldman, A.; Chai, B. H.; Kuzyk, M. G.; ... & Munin, E. *Handbook of optical materials*. CRC press. (2018).

161. Kumar, V.; Kumar, A.; Lee, D. J.; Park, S. S. Estimation of a number of graphene layers using different methods: a focused review. *Materials*, **14**(16), 4590 (2021).

162. Ferrari, A.C.; Meyer, J.C.; Scardaci, V.; Casiraghi, C.; Lazzeri, M.; Mauri, F.; Piscanec, S.; Jiang, D.; Novoselov, K.S.; Roth, S.; et al. Raman Spectrum of Graphene and Graphene Layers. *Phys. Rev. Lett.* **97**, 1–4 (2006).

163. Cançado, L.G.; Da Silva, M.G.; Martins Ferreira, E.H.; Hof, F.; Kampioti, K.; Huang, K.; Pénicaud, A.; Achete, C.A.; Capaz, R.B.; Jorio, A. Disentangling Contributions of Point and Line Defects in the Raman Spectra of Graphene-Related Materials. *2D Mater.* **4**, 025039 (2017).
164. Ribeiro-Soares, J.; Oliveros, M.E.; Garin, C.; David, M.V.; Martins, L.G.P.; Almeida, C.A.; Martins-Ferreira, E.H.; Takai, K.; Enoki, T.; Magalhães-Paniago, R.; et al. Structural Analysis of Polycrystalline Graphene Systems by Raman Spectroscopy. *Carbon*. **95**, 646–652 (2015).
165. Markovska, I.; Georgiev, D.; Rusev, D.; Yovkova, F. Obtaining of electrically conductive graphite paste from cheap and harmless materials for capacitor's electrode coating. *Journal of the Balkan Tribological Association*, **28**(3), (2022).
166. Ohring, M. *Engineering Materials Science*; Elsevier (1995).
167. Tous, L.; Russell, R.; Das, J.; Labie, R.; Ngamo, M.; Horzel, J.; Philipsen, H.; Sniekers, J.; Vandermassen, K.; van den Brekel, L.; et al. Large area copper plated silicon solar cell exceeding 19.5% efficiency. *Energy Procedia* **21**, 58–65 (2012).
168. Noh, B.I.; Yoon, J.W.; Lee, B.Y.; Jung, S.B. Adhesion characteristics of Cu/Ni–Cr/polyimide flexible copper clad laminates according to Ni: Cr ratio and Cu electroplating layer thickness. *J. Mater. Sci. Mater. Electron.* **20**, 885–890 (2009).
169. Xu, X.; Xie, D.; Huang, J.; Liu, K.; He, G.; Zhang, Y.; Jiang, P.; Tang, L.; Wu, W. Influence of Pretreatment Processes on Adhesion of Ni/Cu/Ni Multilayer on Polyetherimide Resin Reinforced with Glass Fibers. *Metals* **12**, 1359 (2022).

Curriculum Vitae

Personal info

Name, Surname: Vitalij Fiodorov

Birthplace: Vilnius, Lithuania

Phone number: +37062862878

Education

2019.10 - 2025.03 Center for Physical Sciences and Technology, the Department of Laser Technologies. PHD student.

PHD thesis: Laser-assisted selective fabrication of copper traces on polymers by electroplating.

2013 - 2015 Vilnius University, Faculty of Physics, Master studies.

Study program: Laser Technology.

Master thesis: Thin metal film ablation with femtosecond pulses.

2012.09 - 2013.02 Vrije Universiteit, Amsterdam, Netherlands. Study semester as an exchange student.

2009 - 2013 Vilnius University, Faculty of Physics, Bachelor studies.

Study program: Physics of Nuclear Energetics.

Bachelor thesis: Thin gold and aluminum film ablation with femtosecond pulses.

1997 - 2009 Vilnius Gabijos gymnasium

Employment experience

2024.09 – now Light Conversion, UAB Service engineer

Description: supporting and installing laser systems.

2021.06 – 2024.09 Altechna R&D, UAB Laser system engineer

Description: designing, assembling, and installing laser micromachining systems.

2013.10 – 2021.06 Ekspla, UAB Laser engineer

Description: assembly of various types of lasers and parametric systems.

Participating in R&D projects.

Languages: Lithuanian – fluent written and spoken,

English – fluent written and spoken,

Russian – fluent written and spoken,

German – basics.

PADĖKA

Norėčiau padėkoti visiems prisidėjusiems prie disertacijos parengimo, nuo fizikos mokytojų ir šeimos, baigiant kolegomis Lietuvoje bei užsienyje.

Vilniaus universiteto leidykla
Saulėtekio al. 9, III rūmai, LT-10222, Vilnius
El. p. info@leidykla.vu.lt, www.leidykla.vu.lt
Tiražas 20 egz.